MONASH University

Ode to Dissipationless Electronics:

Computational Design of Topological Materials

Chutian Wang

BEnvEng (Hons), 2014

A thesis submitted for the degree of *Doctor of Philosophy* at

Monash University in *2021*

Department of Materials Science and Engineering

Faculty of Engineering

Copyright notice

Abstract

Two-dimensional topological insulators (2D TIs) are insulating in the bulk, while having conducting edge states. As a result of the bulk-edge correspondence, the ballistic electron transport for the edge states is dissipationless and can be used to fabricate future low-energy electronics. Large bandgap materials such as bismuth are promising candidates to host edge states at room temperature. Using first-principles calculations and Wannier tight-binding models, the thesis is mainly focused on studying the electronic structure and topological features of different bismuth-related materials.

The challenge in the field of topological material is how to achieve the topological behaviour in a practical device setup. The nontrivial topological states need to be stable against local perturbations while allowed to be tuned via external environmental factors such as an applied field. In this work, we study the robustness of edge states in a two-dimensional topological crystalline insulator (2D TCI) and approaches of modifying them based on a planar bismuthene model. We have found that the mirror symmetry-protected non-trivial topological phase can be maintained when the thin film has a weak interaction with the substrate, or when a sandwich stacking is applied. We observe that spin-filtered edge currents of 2D TCIs can survive strong mirror symmetry breaking fields when they have zigzag edge terminations. Finally, we have demonstrated by modulating the interfacial distance or applying rotation on sandwich structures, bismuthene armchair edge bandgap can be opened, which effectively switches off the nontrivial topological states. This research can provide guidelines for the methodology to tune or maintain those edge states in the design of TCI-based electronic devices.

We have also studied the electronic properties of β’ phase In2Se3, a material that has been newly proved to be stable under room temperature. Consistent with recent experimental observations our results have shown that the material possesses a large bandgap, which makes it a good candidate as a substrate for 2D materials. The large piezo-resistivity of the material is also confirmed through both experimental and our computational results. The large-scale

band structure tuning of the material demonstrates a good example of how pressure controls electronic structures.

Overall, the choosing of substrates, pressure, strain, and electric fields are effective tools to tune the electronic and topological properties of materials. This research can be used to facilitate the design of new generation electronics.

Declaration

This thesis is an original work of my research and contains no material which has been accepted for the award of any other degree or diploma at any university or equivalent institution and that, to the best of my knowledge and belief, this thesis contains no material previously published or written by another person, except where due reference is made in the text of the thesis.

Signature: ……

Print Name: CHUTIAN WANG

Date: 13/Dec/2021

Publications during enrolment

COLLINS, J. L., WANG, C., TADICH, A., YIN, Y., ZHENG, C., HELLERSTEDT, J., GRUBIŠIĆ-ČABO, A., TANG, S., MO, S.-K., RILEY, J., HUWALD, E., MEDHEKAR, N. V., FUHRER, M. S. & EDMONDS, M. T. 2020. Electronic Band Structure of In-Plane Ferroelectric van der Waals β′-In2Se3. *ACS Applied Electronic Materials,* 2**,** 213-219.

LI, Q., SMITH, J. S., YIN, Y., WANG, C., KLYMENKO, M. V., COLE, J. H. & MEDHEKAR, N. V. 2021. Localized Wannier function based tight-binding models for two-dimensional allotropes of bismuth. *New Journal of Physics,* 23**,** 063042.

Acknowledgements

This research was supported by an Australian Government Research Training Program (RTP) Scholarship.

I started computational modeling in 2014, when I took the unit MTE4590 from Monash University, especially the assignments that were painful but rewarding. The supervisor for my assignment, Dr Nikhil Medhekar later became my PhD supervisor in 2017.

I would like to express my gratitude to my supervisors Assoc. Prof Nikhil Medhekar and Prof. Michael Fuhrer for providing guidance for my research. I would also like to thank Dr Yuefeng Yin, who spent a lot of time helping me debugging everything, especially when I was so frustrated amid darkness and cannot figure out where to go next. Without his help, this research is not possible. I would like to thank my milestone examiners Dr Julie Karel, Dr Cornelius Krull, and Assoc. Prof Agustin Schiffrin for their useful discussion and feedback. I would also like to thank Prof Chris McNeill, who introduced me to research in 2014 as my final year project supervisor and later provided me a lot of support as the Graduate Research Coordinator. I would also like to thank our experimental collaborators from the group of Dr Mark Edmonds, Dr Changxi Zheng, and Prof Simon Brown.

I would like to thank the Monash Graduate Scholarship, and RTP Stipend for providing support for my research. I would also like to thank the Faculty of Engineering, Monash University for hiring me as a teaching associate, especially between 2017-2018. Working with first-year university students has been a great experience for me. I wish them all a great future. And I would also like to thank FLEET for organising high-quality workshops, summer schools, and multiple events that helped me learn a lot from top researchers in this field. I admire FLEET's advocate for equality and the bridging between academic, industry and community.

I would also like to thank the developer of the software VASP, Wannier90, Wanniertool, and colleagues at National Computational Infrastructure (NCI) and Pawsey Supercomputing

Centre for making these computations happen. I hope my research will one day benefit the supercomputing industry.

Pursuing a PhD is a lonely journey, especially during 2020-2021, not only because of lockdowns and travel restrictions but also because of fear and depression that spreads among people. I was lucky because when I have nowhere to go, I can listen to classical music and play the piano. I wish to thank all my piano teachers since 2010, who are like my mentors of life and gave me a lot of strength. Especially Ms Cai Meide, Mr Glenn Riddle, and Prof Anatoly Dokumentov. Sadly, Ms Cai passed away in 2020. She had been a good friend to me. No matter where I go in the future, her music and her character have already become part of me.

I wish to thank my parents and other family members for their support. It was my parents who helped me determine that I should do a PhD.

I also wish to thank some of my true friends throughout all those years from when I started university. Thank you for your sincerity and kindness. Although we may seldom contact each other in recent years, I could not survive all those years without thinking of you. I am not good at expressing myself, but I love you all. I hope you can have a smile on your face if someday you happen to see my thesis and find your name here. The names are ranked based on the timeline we started to truly get to know each other. To protect privacy, I use abbreviations here.

I wish to thank my friends Dr JXW, Ms JSH, Ms LHX, Dr PFZ, Mr HHY, Mr QQ, Dr XFZ, Mr. QZ, Mr ZDY, Mr WF, Mr LJ, Ms CYL(CN), Mr ZBG, Mr LT, Ms MHY, Ms SHR, Ms TY, Dr ZY, Ms HCH, Ms CYL(AU), Ms WGY, Ms XDX, Mr FTL, Dr XX, Dr YHZ, Ms LSM, Dr HR, Ms LLM, Dr XG, Mr TM, Ms VZS, Dr ZYL, Dr YP, Mr MDG, Dr HL, Dr YQZ, and Ms HYT for their kindness and support throughout all those years.

List of Acronyms

AC	Armchair
AC-k	Armchair edge with Klein defect
AHE	Anomalous Hall effect
BL	Bilayer
BP	Black Phosphorus
CPU	Central Processing Unit
CVD	Chemical Vapour Deposition
DBP	Distorted Black Phosphorus
DFT	Density Functional Theory
DOS	Density of States
GGA	Generalised Gradient Approximation
h-BN	Hexagonal Boron Nitride
HOPG	Highly Oriented Pyrolytic Graphite
HOTI	Higher-order Topological Insulators
SiCH-(0001)	Hydrogen Passivated Silicon Carbide
ICT	Information and Communication Technology
IQHE	Integer Quantum Hall effect
LDA	Local Density Approximation
MBE	Molecular Beam Epitaxy

ML	Monolayer
MLWF	Maximally Localised Wannier Functions
1BL	Mono bilayer
PAW	Projector Augmented Wave
PBE	Perdew-Burke-Ernzerhof
PVD	Physical Vapour Deposition
QAHE	Quantum Anomalous Hall Effect
QHE	Quantum Hall Effect
QSH	Quantum Spin Hall
QSH	Quantum Spin Hall Insulator
SOC	Spin-orbit coupling
TCI	Topological Crystalline Insulator
3D	Three-dimensional
TB	Tight binding
TI	Topological Insulator
TRIM	Time Reversal Invariant Momentum
TRS	Time Reversal Symmetry
STM	Scanning Tunnelling Microscope
2D	Two-dimensional
2D TCI	Two-dimensional Topological Crystalline Insulators
2D TI	Two-dimensional Topological Insulators

vdW	van der Waals
VASP	Vienna Ab-Initio Simulation Package
WCC	Wannnier Charge Centre
ZZ	Zigzag
ZZ-k	Zigzag edge with Klein defect

Contents

Chapter 1 Overview of the thesis

This chapter provides an overview of the thesis. The related details will be covered in the following chapters.

Dissipationless electron transport can be realised through the edge current of two-dimensional topological insulators. Such electron transport mechanisms can be used to build new generation transistors to extend Moore's law and reduce the energy consumption of future electronics. The edge conduction of two-dimensional topological insulators (2D TIs) is protected by the time-reversal symmetry, as well as the topological order of the material's bulk band structure. The concept has been further extended to 2D topological crystalline insulators (TCIs) [1] as their edge states are protected by mirror symmetry.

Despite the significant theoretical progress that had been made through the years [2], the experimental progress of 2D TI research still underperforms. One challenge is that there is a lack of study that bridges that gap between the theory and experiments [3]. For example, many materials theoretically predicted have the band gap at meV or μeV level [4]. If the band gap is not large enough, the topological features cannot be maintained at room temperature due to band closure. Also, though the 2D TIs may have theoretically predicted edge states in its pure form, they are sensitive to the environment that affects their bulk band structure or symmetry. The substrate will play a significant role as they can tune both the bulk band structure and symmetry. There had been lack of experimental progress in 2D TCIs due to its vulnerability against mirror-symmetry breaking field.

To address those challenges, this thesis focuses on the first-principles calculation of electronic properties of topological materials. The experimental factors such as substrates and pressure are used to tune the electronic and topological properties. The main material in our study is bismuth, as its large band gap makes it a favourable material in experimental fabrication. The methods have been investigated to maintain and tune the edge states, especially with substrates.

This research aims to provide guidelines for two-dimensional topological materials design and bridge the gap between the theoretical calculation and experimental realisation of 2D TIs. The research includes discovering new large-band gap two-dimensional quantum spin Hall (QSH) systems that are stable under room temperature. When constructing such systems, we also need to consider how to implement such systems with experiments. Experimental factors such as substrate, edge termination, and strain etc. should be taken into consideration. More extensive research can be carried out focusing on the electronic properties of TCI. This may include edge-state robustness analysis, and substrate studies that facilitates the realisation of the states in experiments. After the optimum experimental conditions are confirmed to maintain the topological edge states, the next step is to find a way to effectively tune the electronic structures. This can facilitate the design of new generation of electronics with switchable topological current.

Through this thesis, we demonstrated a practical approach to maintain and tune the edge states of topological materials, using experimental factors of strain, electrical field, edge terminations, and substrates. The designing ideas and the map of parameters will be beneficial for future experimental research.

Chapter 3 includes a literature review starting with the basic theory of topological insulators and designing strategies, the current research status for TCIs, and current research status for the studies of bismuth as topological insulators. **Chapter 4** reviews the methodology used in topological materials. **Chapter 5** includes our results in the calculation on different bismuth allotropes, where the Bi (110) results are compared with experimental results. Those studies provide us with understanding of bismuth allotropes' electronic properties, how they can be tuned, and foundations for the specific studies on bismuthene in **Chapter 6** and **Chapter 7**.

Chapter 6 and **Chapter 7** are the main body parts of this thesis. Using bismuthene as the material, we have demonstrated the tuning of TCI edge states via restoring and breaking mirror symmetry. In **Chapter 6**, we mainly focus on how to maintain those 2D TCIs edge states. In **Chapter 7**, we focus on the ways to tune the band gap of 2D TCIs. In **Chapter 8**, we studied the electronic properties of In2Se3, which has unique properties such as large band gap and large piezo-resistance. **Chapter 9** gives the conclusions and outlook of this research.

Chapter 2 Introduction

2.1 Development of Future Electronic Technologies: A Low-Energy Approach

The rapid development in the transistor industry in recent decades has been predicted by Moore's law[5, 6], which stated that the number of transistors in an integrated circuit doubles every two years. However, recently there have been more statements that Moore's Law is coming to an end [7-9]. The trend is shown in **Figure 2.1** as transistors per chip. There are some limitations that may prevent the trend from increasing, including the slowdown of progress in silicon manufacturing technology [10], the quantum uncertainties limit [11], and the CPU clock speed [12]. The clock speed is saturated between 2010 and 2015 as shown in **Figure 2.1** because of its heat dissipation. This brings the fundamental limits is the thermal limits [13]. Having a denser transistor design, or increasing the clock speed, increases the difficulty in cooling, and therefore limits the density of transistors in a circuit. The current transistors industry is strongly dependent on silicon, which is incorporated with the problems of Joule heating [14], which contributes to the heat generation during computation. In addition to that, models have predicted that the total global electricity demand for Information and Communication Technology (ICT) is about to increase to 8~21% of the total global electricity usage [15]. Therefore, finding a low-energy computational approach not only will enhance the computational efficiency but will also contribute to solving the energy crisis. The key issue is to find a dissipationless material that can replace silicon in the design of transistors.

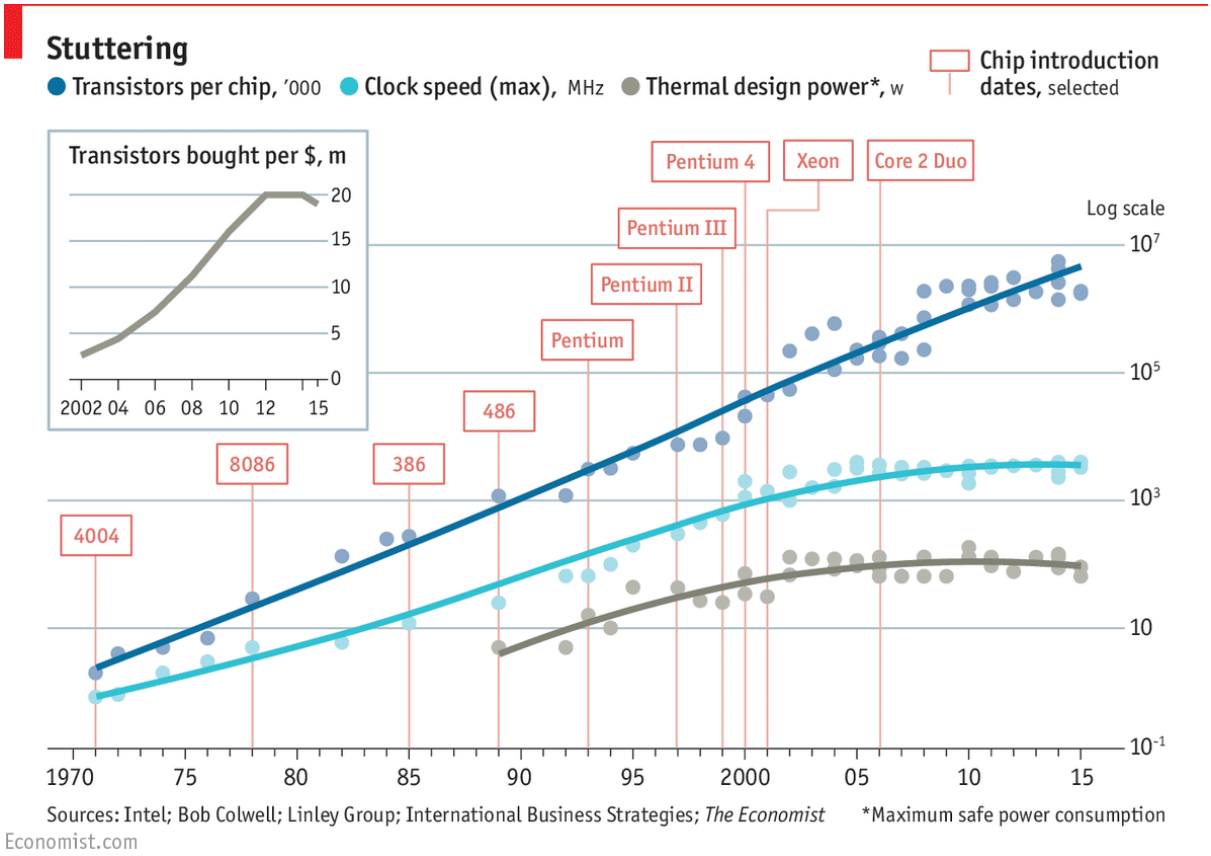

Figure 2.1 A Graph showing Moore's law. While the number of transistors per chip keeps increasing, the clock speed and the thermal design power becomes stable between 2010 and 2015. Graph taken from Ref [16]. Reused under license from © The Economist Group Limited, London (Mar 10 2016).

The recent development of topological insulators material provides a potential solution as the conducting process in this material is dissipationless. Like original (i.e. trivial) insulators, topological insulators have a band gap near the Fermi level. However, due to the non-trivial topological features in its bulk band structure, gapless interface states exist at the interface between the topological insulators and the ordinary insulators. The vacuum can be considered a trivial insulator. Therefore, the conductive interface can be the surface of 3D materials [17], and the edge of 2D materials [18]. The concept has also been extended to the concept of higher-

order topological insulators (HOTI) [19], which has the hinge state on 3D material [20], or corner states of and 3D [21] and 2D [22] materials. The two-dimensional insulators (2D TIs) can be characterised by their bulk-edge correspondence. The edge states in 2D TIs, also known as the QSH state, are robust against disorders and backscattering due to the topological property of the material's bulk band structure. Besides the application in transistors, TIs are also considered as promising materials to be applied in spintronics [23] and future quantum computers design [24].

2.2 Topological Materials: Basic Concepts

Topology is concerned with the properties of spaces that are invariant when space is continuously deformed. Shapes that can be continuously deformed into each other are topologically equivalent and share the same integer topological invariant. For example, in **Figure 2.2** the ball and the polygon can be distinguished by topological invariant g = 0, while

the donut and the tube share the topological invariant g=1, where g is the topological invariant named “genus” that corresponds to the number of holes. [25]

Figure 2.2 The orange shapes are classified with the topological invariant g=0, while the red shapes are classified by the topological invariant g=1.

The concept of topological equivalence in insulators can be defined by the adiabatic continuity of Hamiltonians [26, 27]. Two insulating states are considered topological equivalent if tuning from one Hamiltonian to another can be realised without closing the bandgap. In contrast, tuning the Hamiltonian between two topological non-equivalent insulators cannot be realised without closing the bandgap. Therefore, when connecting two topological non-equivalent insulators together, there will be gapless edge states at the interface protected by bulk topological properties.

The gapless edge states are free from backscattering. This can be understood by a classical illustration of quantum Hall states as shown in **Figure 2.3 (a)**. The electrons, defined by cyclotron orbits, propagate in a chiral manner along a single direction at the interface between two topological non-equivalent materials. **Figure 2.3 (b)** shows QSH interface state in momentum space. The valence band and the conduction band are contributed by the bulk band structure, while the band crossing Fermi level is contributed by the interface state. Vacuum can

be considered as a material with both the topological invariant Chern number n and Z_2 number equal to zero. Therefore, one-dimensional edge states are usually analysed in 2D topological material studies.

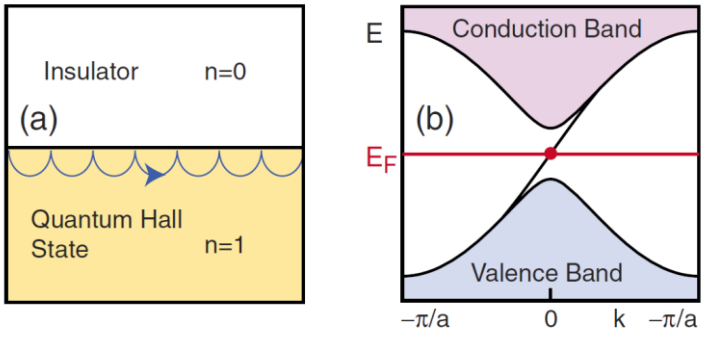

Figure 2.3 (a) Electron motion for Quantum Hall state **(b)** Edge state in bandstructure. Graph taken from Ref [25].

2.3 A Brief History of Discovery of Topological materials

The classical Hall effect was observed experimentally in 1879 [28]. The physicist Edwin Hall discovered that when applying a current and a perpendicular magnetic field to a conductor, a voltage (Hall voltage) forms in the conductor deflecting the current due to the Lorentz Force. In 1880, Hall found that Hall effect can also be realised at systems without magnetic field, when the magnetization in a ferromagnetic or paramagnetic metal contributes to the Hall resistance [29]. Such an effect was named as Anomalous Hall effect (AHE). Later theoretical studies suggested that instead of being equivalent to an external magnetic field, the main contribution of AHE comes from anomalous velocity [30], which is an intrinsic contribution [31] dependent on perfect crystal Hamiltonian. Integer Quantum hall effect (IQHE) observed

in 1980's showed that in a two-dimensional electron system under a strong magnetic field and low temperature, the longitudinal conductance turns to zero at a certain range of magnetic field, while the Hall conductance shows a step like $\sigma = \mathrm{n}\frac{e^2}{h}$, where n = 1,2,… [32] is an integer. Later theoretical studies [33] suggest that the filling factor n is actually a topological invariant in momentum space and is related to the topological properties of bulk material. n is named as TKNN invariant [33] (named after Thouless, Kohomoto, Nightingale and den Nijs), which is equivalent to the mathematical concept Chern number [34]. This invariant can be expressed by the integral over the Berry curvature [34]. This number can be presented by

$$n = \frac{1}{2\pi}\int d^2kF$$

where F is the berry Curvature $F = \nabla \times A$,

A is the berry connection $A = i\sum_{m=1}^{M} < u_m\,(k)|\nabla_k|u_m\,(k) >$,

M is the number of occupied states. When a material that has non-zero Chern-number is put together with a zero Chern number material (such as a vacuum), there will be metallic states on the boundary. Such states are topologically protected.

In 1988, F.D.M. Haldane presented a model for spinless fermions suggesting that Quantum Hall Effect (QHE) may also be realised in a 2D honeycomb graphite (later known as graphene) system by introducing a periodic magnetic field without zero total magnetic flux [35]. The discovery of graphene [36] in 2004 initiated a lot of research in 2D materials. In 2005, Kane & Mele extended the concept of Haldane model to electrons with spin $\frac{1}{2}$. Spin-orbit coupling

(SOC) was applied to replace the effect of magnetic flux [37] in the Haldane model. They predicted the QSH effect QSH in the graphene system, which can be considered as combining two quantum Hall systems with spin up and spin down electrons. Whenever time-reversal symmetry is preserved, the helical interface states at the boundary are protected. Therefore, they are robust against impurities and disorders. QSH states are illustrated in **Figure 2.4 (a)** for real space and **Figure 2.4 (b)** for momentum space.

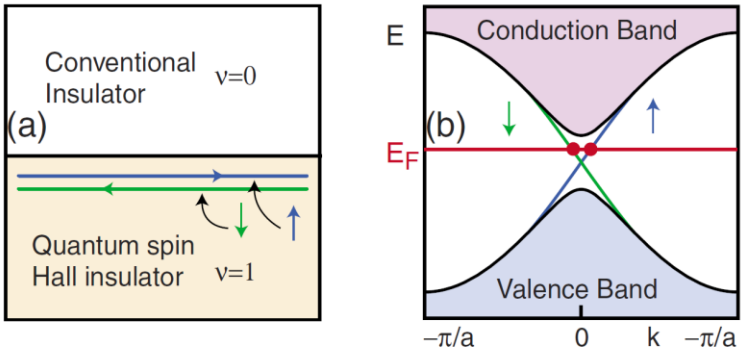

Figure 2.4 (a) Quantum Hall states along the interface between 2D TI and normal insulator (usually vacuum). **(b)** Quantum spin Hall state in momentum space. Graph taken from Ref. [25].

Soon after the theoretical prediction [38], 2D TI was experimentally observed in HgTe quantum-well systems [18]. Later 3D TI was also predicted [39] and experimentally realised [40]. The research of topological insulators has also led to the discovery of various types of novel materials including Dirac semimetal [41], Weyl Semimetal [42], and novel quantum phenomena such as quantum anonymous Hall effect [43]. In 2019, a high throughput calculation was done and found 3307 TIs, and shows that more than 27% of material in nature are topological [44].

Chapter 3 Literature review

3.1 Theories of topological Insulators

3.1.1 Symmetry and Topology

In momentum space, time reversal symmetry (TRS) can be expressed in the following formula:

$$\Theta H(\boldsymbol{k})\Theta^{-1} = H(-\boldsymbol{k})$$

where Θ is the time-reversal operator. This formula tells that the Hamiltonian of a k state degenerates with its time-reversed pair. Therefore, Bloch state pairs degenerate at all time reversal invariant momenta (TRIMs) [45], the high symmetry points in the Brillouin Zone that are invariant under time reversal operation. Those TRIMs fulfil $\boldsymbol{\lambda} + \boldsymbol{G} = -\boldsymbol{\lambda}$, where $\boldsymbol{\lambda}$ are the TRIMs and $\boldsymbol{G}$ is the reciprocal lattice vector. Such degeneracy is shown in **Figure 3.1 (a)**, while an example in sampling of TRIMs in the 2D Brillouin Zone for a square lattice is shown in **Figure 3.1(b).** The Brillouin Zone for a 2D square lattice is also a 2D square lattice. $\boldsymbol{\Gamma}_{11}$, $\boldsymbol{\Gamma}_{12}, \boldsymbol{\Gamma}_{21}$ and $\boldsymbol{\Gamma}_{22}$ are the four TRIMs for a 2D square lattice with periodic boundaries. When a nanoribbon is constructed, one direction of nanoribbon becomes infinite and the other remains periodic, the Brillouin Zone will be contracted into a line. The TRIMs for 2D nanoribbon can be presented as $\boldsymbol{\Lambda}_1$ and $\boldsymbol{\Lambda}_2$, which can be projected $\boldsymbol{\Gamma}_{11}$, $\boldsymbol{\Gamma}_{12}, \boldsymbol{\Gamma}_{21}$, and $\boldsymbol{\Gamma}_{22}$.

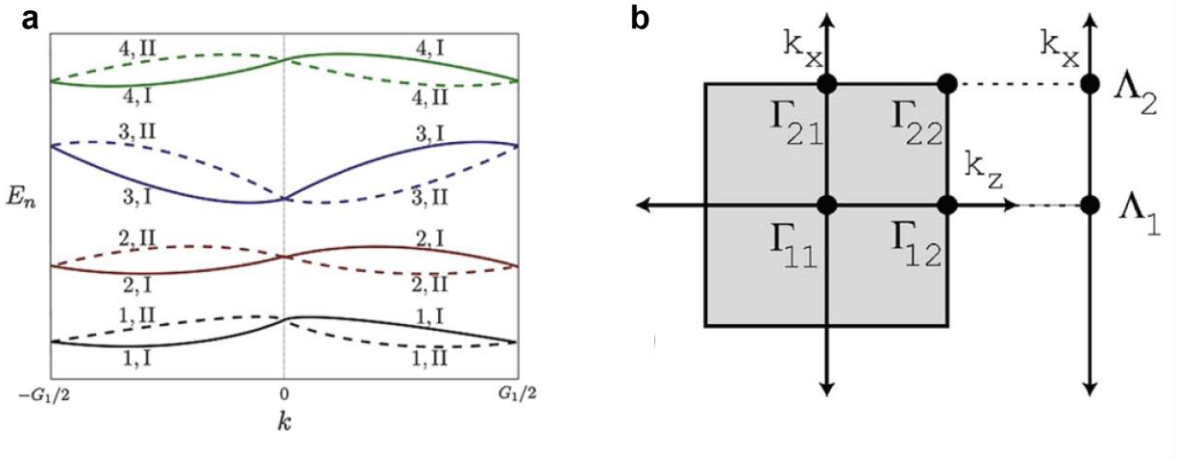

Figure 3.1 (a) Band structure for TRS system along 1D direction in momentum space. Graph taken from Ref. [46] **(b)** TRIMs in two-dimensional square Brillouin zone. Graph taken from Ref. [39].

In time-reversal symmetric systems, the TKNN invariant is zero because the spin up and spin down states directly cancel each other when added up. Therefore, Kane and Mele introduced a Z_2 topological classification to describe the topological property of time-reversal symmetric systems [47].

The Z_2 topological order can be explained in **Figure 3.2**. Both graphs in **Figure 3.2** show the dispersion of surface states in between two TRIMs. However, in **Figure 3.2(b)** there is a single Fermi level crossing, while in **Figure 3.2(a)** there is an odd Fermi level crossing. Therefore, in **Figure 3.2(a)** the surface states can be easily removed by perturbations pushing surface states away from the Fermi level. In this case the material is considered a trivial insulator with Z_2 topological invariant $\nu = 0$. In contrast, in **Figure 3.2(b)** if the perturbation does not close the bulk band gap, the edge states are always protected by time-reversal symmetry. Such system is considered a Z_2 non-trivial with Z_2 topological invariant $\nu = 1$.

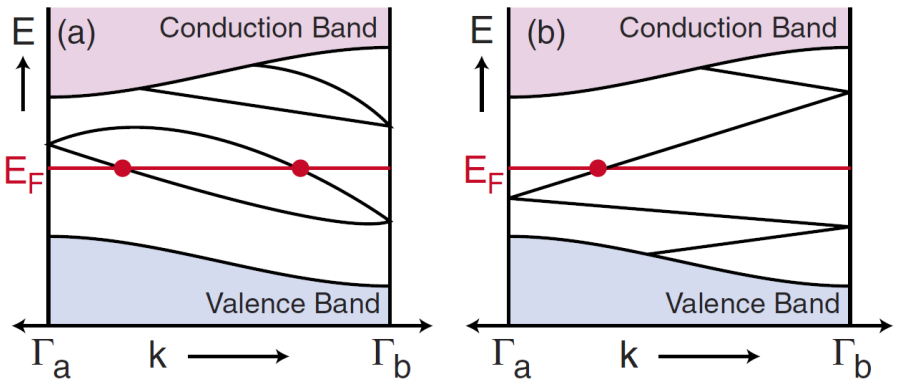

Figure 3.2 Edge states for **(a)** v=0 and **(b)** v=1 topological systems. Graph taken from Ref. [25].

However, the Z_2 number is not the only symmetry that results in the non-trivial edge states. **Figure 3.3** gives a tree graph summary to describe the classification of the two-dimensional insulators. The green column denotes the where the trivial states can occur. In the top layer, a non-zero Chern number denotes the circumstances of the topological features when the time-reversal symmetry is broken. This corresponds to the circumstance that the material is exposed to a magnetic field [48], or magnetic doping [49]. The doping approach uses the intrinsic properties of the material to generate spontaneous breaking of time-reversal symmetry without introducing a magnetic field. Realising Quantum Hall effect with doping approach is also known as quantum anomalous Hall effect (QAHE) [50] . The QAHE has recently achieved tuning the Chern number up to 5 without a magnetic field [51]. With broken time-reversal symmetry, n=0 means the edge states are trivial. When the Chern number n is 0, and the time-reversal symmetry is preserved, the non-trivial edge states exist when the material has a non-zero Z_2 number ν. This corresponds to the Z_2 topological insulators. A zero Z_2 number ν, in this case, indicates that the edge states are Z_2 trivial as they are not protected by TRS. When ν =0, but the mirror-Chern number (Cm) is non-zero, the edge states of the material are protected

by mirror symmetry. This corresponds to the TCI case. With both non-zero Z_2 number and mirror Chern number, a dual topological insulator [52] material can also be realised with both TI and TCI characters.

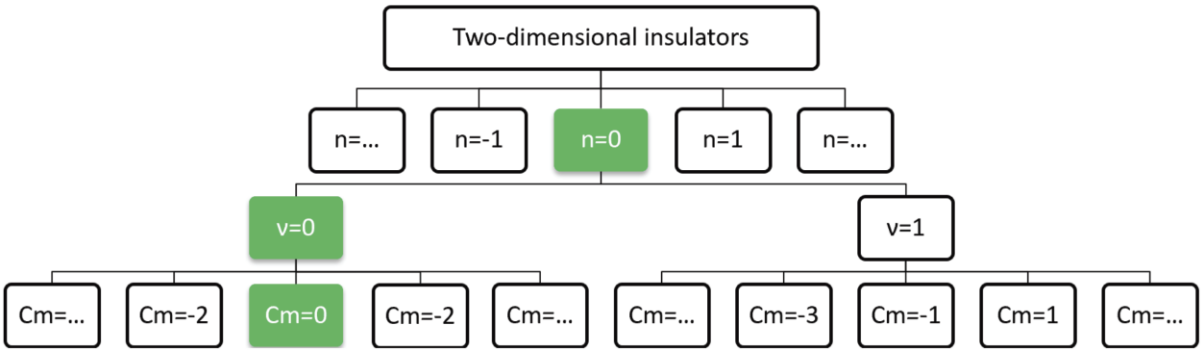

Figure 3.3 Topological family tree of two-dimensional insulators. The green column denotes the topological invariant where trivial states can occur, while the other columns the topological number that associated different types of non-trivial insulators. Graph modified from Ref. [53].

3.1.2 Basic Strategies in Materials Design

There are two basic mechanisms to create a topological insulator. **Figure 3.4(a)** shows the Type I mechanism. The material without SOC has a Dirac point at the Fermi level, connecting the valence band with the conduction band. After the SOC is applied, the bandgap opens at Dirac point. A good example is the band gap opening of graphene predicted by Kane and Mele [37] **Figure 3.4(b)** shows the Type II mechanism introduced by Bernevig, Hughes, and Zhang [38] on the HgTe Quantum Well system. The material without SOC has a trivial band gap. The SOC closes the trivial bandgap and opens a non-trivial band gap, causing the parity to exchange between bands around Fermi level. To realise this band inversion, researchers have developed

various strategies such as doping heavy atoms to induce large SOC [54] , strain tuning the band structures [55], and electrical field tuning of band structures [56].

The phase that appears in the transition between a topological insulator and a trivial insulator is topological semimetal [42, 57], which has a Dirac cone with SOC. The material can be tuned to topological insulator when a band gap is opened via quantum confinement [58] , strain [59] or electric field [60].

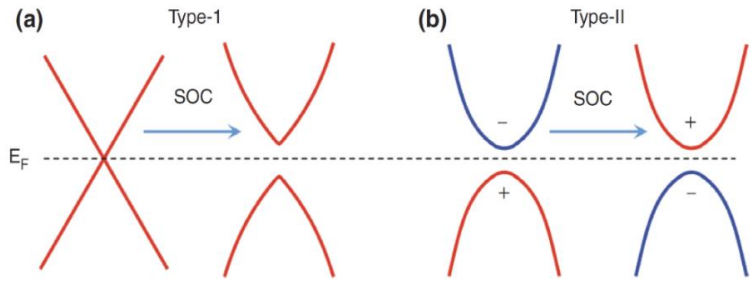

Figure 3.4 Two mechanisms to create an TI. **(a)** Band gap opened by SOC. **(b)** Band inversion around the Fermi level introduced by SOC. Graph taken from Ref. [61].

3.1.3 The Significance of Substrates in 2D Topological Materials

The techniques used in the synthesis of 2D materials include the top-down approaches and bottom-up synthesis [62]. For the top-down approach, the 2D nanosheets can be exfoliated through the micromechanical cleavage process or the solution-based exfoliation process. However, mechanical exfoliation (such as the exfoliation of graphene [36]) are labour intensive, while liquid exfoliation is limited in terms of flake size and film quality [63].

The more superior techniques used are the bottom-up approaches. Among them are the chemical vapour deposition (CVD) and physical vapour deposition (PVD). Both approaches require the thin film to grow on the substrates, where the interactions such as strain [64] and chemical conditions [65] may affect the structures and properties of the grown material. When the interaction between substrate and the thin film is strong, the substrate tends to match with the substrate [66]. In many cases, the lattice mismatch will distort the thin film deposited and defects are created [67]. When the interaction is weak, the van-der Waals epitaxy exists and the defect-free interface can be achieved [68].

In the synthesis of topological insulator materials, a more precise bottom-up approach Molecular Beam Epitaxy (MBE) [69] is generally used. The substrate condition plays an important role not only in providing structural support to the topological insulator thin film but also in improving the electronic and topological properties of the materials. The contrast between two milestones in synthesizing graphene-like V-group thin film is a good example demonstrating the substrate role. Those two milestones are the synthesis of the planar bismuthene on SiC-(0001) [70] and planar antimonene on Ag (111) [71]. Structurally both substrates can support the flat structure as they have a lattice constant close to the relaxed flat thin film rather than relaxed buckled thin film. However, the key difference between the two substrates is their influence on electronic properties. The strong interaction between bismuthene and the substrate SiC-(0001) has caused changes in electronic band structures in bismuthene through the orbital filtering effect [72]. In contrast, the weak interaction between Sb and Ag (111) is expected to maintain the electronic features of the freestanding flat-antimonene.

3.2 Current Research on Topological Crystalline Insulators

In 2011, Liang Fu extended the concept of TRS protected topological insulator to topological crystalline insulators, a class of material with non-trivial band topology protected by crystalline symmetry. [73] The first model is based on a 3D tetragonal lattice with the non-trivial surface states protected by tetragonal C_4 symmetry. Unlike TRS-protected surface states in 3D TIs, the non-trivial edge states in 3D TCIs are surface dependent and can only be preserved when the surface has certain crystalline symmetries.

A similar topological invariant, mirror Chern number [74], can be defined to classify the TCI, similar to the Z_2 invariant used in TRS-protected topological insulators. In 2012, TCI phases were predicted on SnTe rocksalt structure [1] protected by crystalline mirror symmetry. Later the TCI concept has been extended to two-dimensional systems such as $Pb_{1-x}Sn_xSe$ (Te) thin films [75] and PbSe monolayer [76]. The 'weak' protection of crystalline symmetries means that TCI topological states are sensitive to various perturbations such as electrical field [75], substrate [77] and strain [78], as those distortions break crystalline symmetry. This can be turned into an advantage because it is possible to design devices that are easy to turn on and off [75]. Time reversal symmetry can be a feature protecting the edge states. However, it is not an essential feature that those non-trivial edge states exist. Several designs have been proposed in previous studies [75, 78]to realise TCI/TI/trivial insulator transition through strain engineering.

Using four-band k.p theory, Liu et al. have identified two types of surface state [79] that may exist in 3D TCI systems in SnTe material. Type I surface states can be found in (111) surface

in the SnTe material, the distinctive feature is that the degeneracy points are located at the TRIMs, and therefore they are simultaneously protected by time reversal symmetry and (110) mirror symmetry. In contrast, Type II surface states, which can be found at (001) and (110) surfaces, have degeneracy points at those non-TRIMs protected only by mirror symmetry. This surface dependent behaviour of 3D TCI inspires us to look for the 2D TCIs that will behave differently on different edges.

The evidence of TCI has been observed on 3D systems including SnTe [80] and $Pb_{1-x}Sn_xSe$ [81] through angle-resolved photoelectron spectroscopy (ARPES) measurement of the surface band structure. Ref. [81] also presented a temperature-driven phase transition between TCI and trivial insulator phase. However, there is still a lack of experimental evidence of the presence of two-dimensional TCIs.

3.3 Theoretical Model Development for Topological Materials

3.3.1 Haldane Model

The Haldane model [35] was the first to predict that the quantum hall effect can be realised without an external magnetic field.

The Hamiltonian for Haldane model can be presented as

$$H(\boldsymbol{k}) = 2t_2 cos\varphi[\sum_i \cos(\boldsymbol{k}\cdot\boldsymbol{b_i})]\boldsymbol{I} + t_1\{\sum_i [\cos(\boldsymbol{k}\cdot\boldsymbol{a_i})\,\boldsymbol{\sigma}^1 + \sin(\boldsymbol{k}\cdot\boldsymbol{a_i})\,\boldsymbol{\sigma}^2]\} + \{M - 2t_2 sin\varphi[\sum_i \sin(\boldsymbol{k}\cdot\boldsymbol{b_i})]\}\boldsymbol{\sigma}^3$$

The t_1 term denotes the nearest neighbour simple tight-binding model for graphene ("2D graphite" in 1988), where $\boldsymbol{a_i}$ is the nearest neighbour vector. $\boldsymbol{\sigma^1}$ and $\boldsymbol{\sigma^2}$ are effectively $\boldsymbol{\sigma_x}$ and $\boldsymbol{\sigma_y}$ for the Pauli Matrix. The Dirac cone at the K and K' point of graphene is protected by both sublattice symmetry and timer reversal symmetry. This nearest neighbour term is similar to the model built by Semenoff in 1984[82], where the onsite energy M was also introduced to break the sublattice symmetry and create a bandgap. However, such a gap can only lead to a normal insulator. The creative part is Haldane's t2 term, which is contributed by second nearest neighbour terms within both the A and B sublattice. The imaginary hopping between sublattice and sublattice b follows the same chirality and induces an opposite magnetic flux in the **a** and **b** region in **Figure 3.5.** The total magnetic field though the whole region is zero. However, the term t2 breaks the time-reversal symmetry and can tune the material from a trivial insulator to a non-trivial Chern insulator.

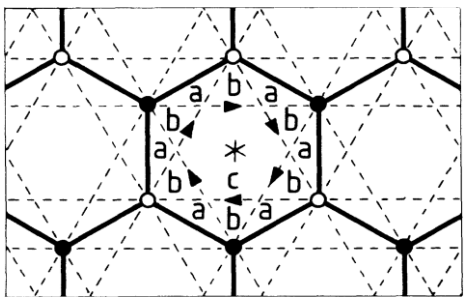

Figure 3.5 Haldane model. Graph taken from Ref. [35].

3.3.2 Kane & Mele Model

The magnetic flux in Haldane's model has not been realised in the experiment. However, in 2005 the Kane & Mele model generalises the Haldane model by using the SOC as a

replacement of the magnetic flux in Haldane's model. The difference is that the SOC does not break time-reversal symmetry. It can be considered as two Haldane models (with spin-up electrons and spin-down electrons) that are time-reversal symmetric added up. The spin-up states and spin-down states have opposite Chern numbers. The net Chern number is 0 and cannot be used to describe the topological features. Therefore, it becomes a Z_2 topological insulator.

The tight binding Hamiltonian for graphene in Kane and Mele model can be presented as

$$H = t\sum_{\ll ij \gg} c_i^\dagger c_j + i\lambda_{SO}\sum_{\ll ij \gg} v_{ij} c_i^\dagger s^z c_j + i\lambda_R \sum_{<ij>} c_i^\dagger \left(\boldsymbol{s} \times \hat{\boldsymbol{d}}_{ij}\right)_z c_j + \lambda_v \sum_i \xi_i c_i^\dagger c_i$$

The four terms of the model are the nearest neighbour hopping term, a SOC term and the nearest neighbour Rashba term, and a staggering sublattice potential term. t is the hopping parameter. $c_i^\dagger$ and c_j are the annihilation operator at i site and creation operator at j site. λ_{SO} is the intrinsic SOC strength. $v_{ij} = \pm 1$ and the sign notes the direction of the election transport. s^z is the σ^z is the Pauli Matrix. $\hat{\boldsymbol{d}}_{ij}$ is the nearest-neighbor vectors from site i to site j. $\boldsymbol{s}$ is the vector of Pauli matrices for the spin degree of freedom. λ_v is the staggered sublattice potential. $\xi_i = \pm 1$ represents the two sublattices of the graphene system.

3.4 Bismuth as a Topological Insulator Material

Since the bandgap of TI is opened by strong SOC, TI usually involves heavy elements that induce strong SOC. Bismuth is a material with strong SOC and it has been one of the most frequent elements contained in predicted 2D and 3D topological materials [26]. In its natural

form, the three-demensional bulk bismuth has rhombohedral crystal structure [83]. As shown in **Figure 3.6**, in its three-dimensional bulk form, bismuth (111) has the structure formed with bilayers (BLs). Within one bilayer the Bi atoms are bonded through a covalent bond, while between bilayers the material is combined through van der Waals interaction. Therefore, bilayers are usually considered units in thin-film bismuth studies. Bi (111) mono bilayers (1BLs) are also referred to by some literature as “buckled single layer bismuthene” [84]. However, in this thesis “bismuthene” only refers to the planar honeycomb graphene-like structure replacing the carbon atoms with bismuth atoms. **Figure 3.7** shows the transition between two structures under strain.

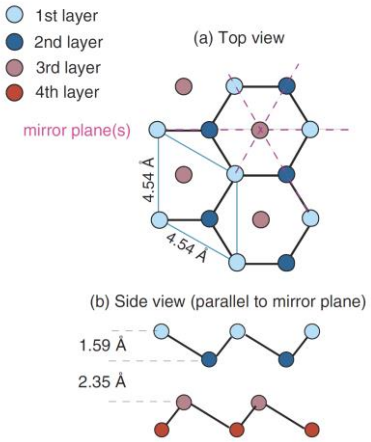

Figure 3.6 Truncated bulk structure of Bi (111). Graph taken from Ref. [85].

Figure 3.7 Bi (111) 1BL stretched to freestanding planar bismuthene. Graph taken from Ref. [77].

3.4.1 Bismuth (111) Bilayer

Bi (111) 1BL is one of the earliest predicted 2D TIs. In 2006, Murakami et al. demonstrated that the spin Hall conductivity is directly associated with strong diamagnetism, which is a measure for SOC strength [86]. Therefore, bismuth was chosen as the candidate material. The study demonstrated that Bi (111) 1BL is a TI through calculation of Pfaffian. The non-trivial properties were further confirmed in later studies through parity analysis and first-principle calculation of nanoribbon edge states [87]. As shown in **Figure 3.8**, the non-trivial topology can be maintained between 1-bilayer and 4-bilayer in its pure form, and up until 8-bilayer with surface adsorption of hydrogen [88]. Such robustness makes the realisation in experiments more promising, as it is difficult to synthesize single layer bismuth. Research has also shown that Bi (111) 1BL TI states are robust against up to 6% strain or 0.8eV/Å of external electric

field [89]. Through first-principles calculation, Huang et al. demonstrated that the non-trivial topology can be maintained when Bi (111) 1BL is placed on various substrates, identifying hexagonal boron nitride (h-BN) to be the best substrate to support the non-trivial property [90]. Wang et al. calculated that the edge adsorption of hydrogen atoms can tune the topological edge state and increase the Fermi velocity to 0.9×10^6m/s [91], which is comparable to the record-breaking fermi velocity in suspended graphene $(3 \times 10^6$m/s) [92].

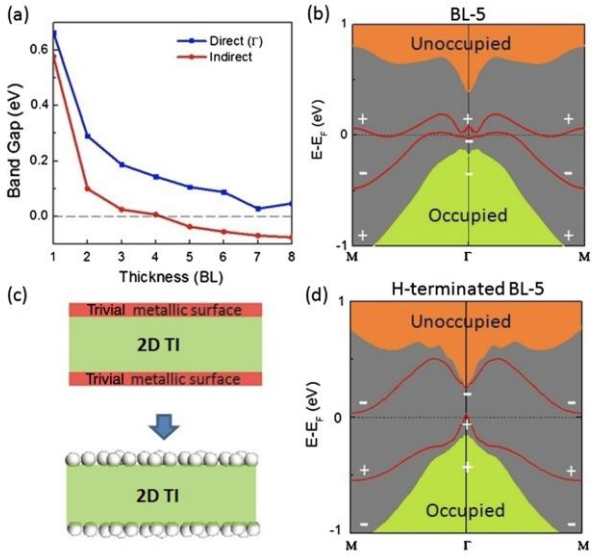

Figure 3.8 The calculation found that non-trivial topology is robust within the range between 1BL-4BL of Bi (111). As shown in (a) and (b), at 5 or more BLs, the indirect bandgap closes, turning the material into metals. However, as shown in (c) and (d), the indirect bandgap opens after hydrogen termination. Graph taken from Ref. [88].

Experimentally, the edge states of Bi (111) BLs were first observed and resolved on both clean and Bi covered Bi_2Te_3 substrates [93]. Later $G_0 = 2e^2/h$ step-wise conductance was

measured on Bi (111) substrate via mechanical exfoliation of a Bi (111) 1BL at room temperature using a scanning tunnelling microscope (STM) [94].

3.4.2 Bulk Bismuth Crystals

In 2014, Drozdov et al. claimed topological 1D edge states of Bi (111) 1BL was observed through STM measurement on bulk Bi crystals [95], as a result of the decoupling of a Bi BL from Bi substrate. However, the surface state found in bulk bismuth was claimed to be trivial in later research [96, 97], as the band structure calculation suggests that the surface states are trivial since it has even times of Fermi level crossing. However, in 2018, it has been proved that this 1D state in bulk bismuth is actually a non-trivial hinge state of a HOTI [20]. The second-order hinge states here are protected together by time-reversal symmetry, inversion symmetry, as well as three-fold rotational symmetry around the z-axis. Later in 2019, bulk bismuth has also been reported to be a first-order 3D TCI, as the $(1\bar{1}0)$ surface exhibit non-trivial surface states [98]. The same study also found 1D hinge states protected by twofold rotational symmetry.

3.4.3 Bismuthene

Huang et al. (2013) performed a theoretical structural analysis on ultra-thin film. The analysis shows that although Bi (111) 1BL is a stable structure at the optimised lattice constant 4.33 Å, the metastable planar honeycomb structure (planar bismuthene) is more energy favourable

when the lattice constant is larger than 5.2 Å [90]. The planar bismuthene is proved to be Z_2 trivial, but it can be tuned to Z_2 non-trivial phase by putting onto substrate such as Si (111)-$\sqrt{3} \times \sqrt{3}$-X (Cl, Br, I) surface [99] or SiC (0001) surface [70, 100]. The dangling bonds from Si substrate forms bonds with planar bismuthene to provide structural stability. In the meantime, the pz orbitals are pushed apart from the Fermi level so the topology is changed [99]. Similar effects can also be seen in BiX/SbX (X=H, F, Cl, Br) [101], where a 2D TI with a record-breaking band gap 1.08eV 2D TI is predicted for monolayer BiF structure. However, experimental studies have shown that the high reaction rate of plasma fluorination and hydrogenation [102] may bring disorders and defects to the structure. Therefore, researchers tended to look at functionalised groups such as methyl, cyanide,, amidogen and oxide which has predicted to open the bandgap of thin-film bismuth to 0.934 eV [103], 1eV [104], 0.83 eV [105] and 0.28eV [106] while maintaining the TI phase. In 2017, the orbital filtered planar bismuthene as a Z_2 topological insulator was realised on SiC (0001) substrate [70]. The experimental band gap has been detected as 0.8 eV and the 1D conductive edge states are measured via scanning tunnelling spectroscopy (STS).

Besides its Z_2 topological behaviour, bismuthene is also distinguished by its non-trivial property as a 2D TCI in its freestanding form [77]. In contrast to Huang et al.'s conclusion in Ref [90] that the planar bismuthene has trivial edge states, Hsu et al. [77] suggested that the edge states are protected by mirror symmetry and its topological properties can be defined with the topological invariant mirror-Chern number C_m =2. Antimonene is another 2D TCI predicted in Hsu et al.'s work [77], which has similar structures and topological properties as bismuthene. While planar bismuthene has not been synthesized on the substrate with weak interaction, the

synthesized planar antimonene on Ag (111) substrate [71] is a promising result, suggesting the flat graphene-like Group V elemental structure can be fabricated on weak substrates.

3.4.4 Bi (110) Thin Films

Bi (110) thin films refer to the pure bismuth thin film in black phosphorus (BP) structure. The material was first discovered in 2004 [107] and named as Bi {012} phase when Nagao et al. found that on Si(111)-7×7 puckered layers form below a certain thickness (<4ML) at room temperature. After the film has been grown to a larger thickness, the material regains Bi (111) buckled phase. Later studies found that edge reconstructions open a band gap of 0.4eV for the 4 monolayer (ML) Bi (110) layer [108]. In 2014, the 2ML and 4ML layers of Bi (110) film were identified as TIs [109]. 6ML Bi (110) also has a non-trivial Z_2 number but turns metallic due to the bulk band closure. Also, the band topology has been proved sensitive to the atomic atomic corrugation. As shown in **Figure 3.9**, simulation results have shown that the topological feature of 2ML thin film with perfect BP structure transitions from non-trivial to trivial when it is distorted. The critical height for the transition is 0.1 Å. The atomic corrugation can be strongly determined by the substrate. For example, BP is more stable with Si (111)-7×7 substrate [107], while distorted black phosphorus (DBP) structure is more stable with highly oriented pyrolytic graphite (HOPG) substrate [109].

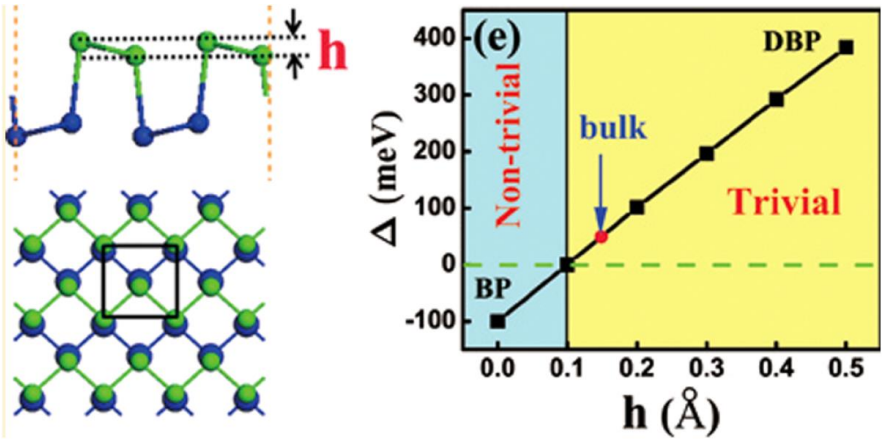

Figure 3.9 The atomic corrugation in 2ML Bi (110) DBP structure and its effect on the triviality. The height h measures the level of atomic corrugation. Graphs taken from Ref [109].

3.5 Comments

The experimental progress in the fields of 2D topological insulators is much slower than the advance in theoretical prediction [2]. One of the main reasons is that most materials do not have a large band gap opened by SOC. Therefore, the band gap may close when the temperature is a lot higher than 0K. For example, as the first predicted topological insulator, graphene has a band gap in the order of 10^{-3} eV [110], which makes it hard to observe topological protected edge states through experiments. Another reason is the difficulty to synthesize 2D materials with perfect crystal structure [111]. In addition, the substrate effect sometimes can be detrimental to experimental realisation. Substrates act as periodic potential exerted on the thin film material and effectively alters the band structure. The freestanding thin film TI may change its property when placed on a substrate. Planar bismuthene on SiC (0001) surface is a good example for this because the TI feature is induced by the substrates. However, that is only limited to Z_2 Topological Insulator phases. The recent studies of topological non-trivial phases

have been extended from time-reversal symmetry protected systems to crystal symmetry protected systems. Compared to 2D TIs, 2D TCIs still have a lot of potential to uncover. For example, although the bismuth-related material has been extensively studied for its TI phase, fewer works have focused on its TCI feature formed by freestanding planar bismuthene.

Chapter 4 Methodology

4.1 Density Functional Theory Calculation

Density functional theory (DFT) is an effective method to study the electronic property of the many-body system. A detailed description of DFT can be found in some textbooks [112, 113]. A recent review listed some most recent applications of the method [114]. This section briefly introduces the fundamentals of DFT.

The many-body system can be described by many-body Schrödinger equation,

$$\hat{H} = -\sum_i \frac{\hbar^2}{2m_e}\nabla_i^2 + \sum_{i,I}\frac{Z_I e^2}{|\mathbf{r}_i - \mathbf{R}_I|} + \frac{1}{2}\sum_{i\neq j}\frac{e^2}{|\mathbf{r}_i - \mathbf{r}_j|} - \sum_I \frac{\hbar^2}{2M_I}\nabla_I^2 + \frac{1}{2}\sum_{I\neq J}\frac{Z_I Z_J e^2}{|\mathbf{R}_I - \mathbf{R}_J|}$$

The terms in the right-hand side equation represents the kinetic energy of the electrons, interactions between electrons, the kinetic energy of nuclei, the interaction between atoms, and interaction between electron and atoms. In the formula, i and j represents the i^{th} and j^{th} electron, while I and J represents the I^{th} and J^{th} nuclei. r and R stand for the coordinates of electrons and nuclei, respectively. ∇ is the Laplacian operator. m_e and M_I are the electron mass and nuclei mass. Z is the charge of nuclei. After Born-Oppenheimer approximation [115] is applied, the electronic motion and the nuclei motion are assumed separated. Since the motion of electrons is a lot faster than the motion of nuclei, the nuclei are considered frozen. Therefore, the equation is reduced to

$$\hat{H} = -\sum_i \frac{\hbar^2}{2m_e}\nabla_i^2 + \sum_{i,I}\frac{Z_I e^2}{|\mathbf{r}_i - \mathbf{R}_I|} + \frac{1}{2}\sum_{i\neq j}\frac{e^2}{|\mathbf{r}_i - \mathbf{r}_j|}.$$

Since the many-body system is still challenging to solve, researchers developed different strategies for single-electron approximation. The simplest approach is the free electron model with the approximation that drops the electron-electron and electron-ion interaction [116]. Although this approach fails in most cases as it cannot distinguish between metal and insulator, it helps to introduce the concept of Fermi energy. Later Hartree approximation was developed considering the many-body wavefunction as a product of each individual electron wavefunction [117]. This theory was further developed by Fock and Slater to include the exchange term to derive the Hartree-Fock equation [118, 119]. However, the shortage for Hartree-Fork equation correlation energy was not considered.

DFT added the exchange-correlation energy part to the one-electron approximation. DFT is under two fundamental theorems [120]. Firstly, the ground-state electron density determines the Hamiltonian, and therefore the properties of the system. The second theorem suggests that the electron density that minimises the energy functional is the exact ground-state electron density. DFT uses Kohn-Sham equation [121] to approximate Schrodinger's equation. The Kohn-Sham equation can be written as

$$\left[-\frac{\hbar^2}{2m}\nabla^2 + V(\mathbf{r}) + V_H(\mathbf{r}) + V_{\mathrm{XC}}(\mathbf{r})\right]\psi_i(\mathbf{r}) = \varepsilon_i\psi_i(\mathbf{r}).$$

where the first three terms in the bracket can be determined exactly. $V(\boldsymbol{r})$ represents the potential between an electron and overall nuclei. $V_H(\boldsymbol{r})$ is the Hartree potential which defines

the Coulomb interaction between one electron and the total electron density. $\psi_i(\boldsymbol{r})$ is an individual electron wavefunction with eigenvalue ε_i. The $V_{xc}(r)$ part is the exchange-correlation functional, which cannot be calculated directly. However, it can be approximated with different approaches. The general approaches include Local Density Approximation (LDA) [122] and Generalised Gradient Approximation (GGA) [123]. Various softwares have been developed to perform DFT calculation, including Vienna Ab-Initio Simulation Package (VASP) [124, 125]， WIEN2K [126], QUANTUM ESPRESSO [127], and ABINIT [128].

One of the challenges for DFT is the modelling of van der Waals (vdW) interaction, which plays a crucial role in multi-layer two-dimensional material systems. Since vdW is a result of long-range electron correlation [112], where standard DFT may not provide an accurate description. To model the van der Waals interaction, researchers developed different methods as add-ons to DFT. Those methods include DFT-D2 [129] and DFT-D3 [130] developed by S. Grimme, and DFT-TS [131] developed by A. Tkatchenko and M. Scheffler. The general calculation steps for DFT are shown in **Figure 4.1**.

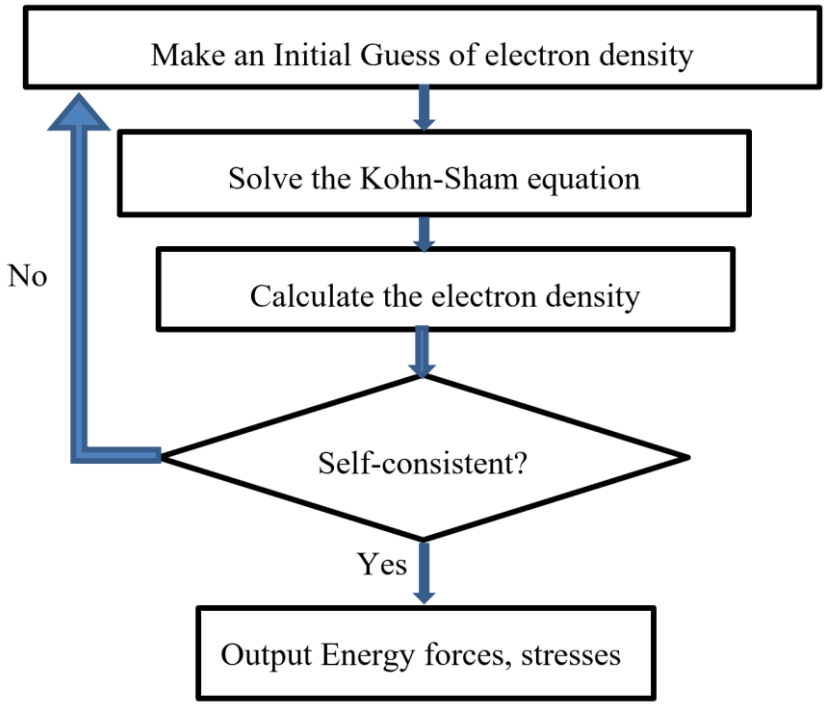

Figure 4.1 General steps for DFT calculation.

4.2 Wannier Functions

4.2.1 Tight Binding Method Based on Wannier Functions

Tight binding (TB) model is an effective method to study electronic structures of solid state systems. The logic behind the TB model is to consider the wavefunction of a single electron as the linear combination of isolated atomic orbitals. Methods to construct TB model includes Slater-Koster Method [132], and maximally localised Wannier functions (MLWF) [133] method. MLWF TB model Hamiltonian can be constructed through DFT calculation associated with the software Wannier90 [134].

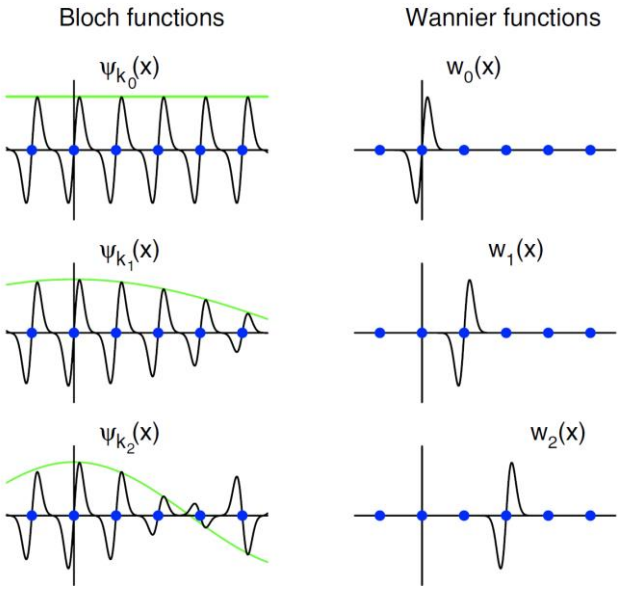

Figure 4.2 Illustration of Bloch wavefunction and Wannier functions. Graph taken from Ref. [135]

The Wannier function is the Fourier transform of the Bloch function in real space. As shown in **Figure 4.2**, in contrast to Bloch functions that spread through the momentum space, the Wannier functions are localised at each individual atom.

The relation between Bloch function and Wannier function [136] can be written as

$$|\boldsymbol{R}n>=\frac{V}{(2\pi)^3}\int_{BZ} d\boldsymbol{k}\, e^{-i\boldsymbol{k}\cdot\boldsymbol{R}}|\psi_{n\boldsymbol{k}}>$$

$$|\psi_{n\boldsymbol{k}}>=\sum_{R} e^{i\boldsymbol{k}\cdot\boldsymbol{R}}|\boldsymbol{R}n>$$

$|\boldsymbol{R}n>$ is the Wannier function in the Rth cell for the nth band. V is the real-space primitive cell volume. $|\psi_{n\boldsymbol{k}}>$ is the eigenstates of the Hamiltonian, where $\boldsymbol{k}$ is the wavevector. However,

Wannier functions are not uniquely determined by the Bloch function because of the choice of phases in the Bloch orbital. Therefore, the shape and spread of Wannier function can have large variations. To solve this issue, MLWF method [133] was developed. A review of the theory and application of MLWF can be found at Ref. [135]. The basic idea behind this is to define a localization criterion that measures and minimizes the spread of Wannier function around their centres. The matrix element from MLWF TB Hamiltonian be expressed as

$$H^{W}_{\boldsymbol{k},nm} = < \psi^{W}_{\boldsymbol{k}n} | H | \psi^{W}_{\boldsymbol{k}m} > = \sum_{\boldsymbol{R}} e^{i\boldsymbol{k}\cdot\boldsymbol{R}} < \boldsymbol{0}n | H | \boldsymbol{R}m >.$$

Where **0** and **R** stands for the home cell and the **R**th cell, with the band index n and m.

4.3 Our Computational Workflow

4.3.1 Methodology

The general step for 2D TI calculation involves band structure calculation, calculating topological invariants and plotting edge states. In the calculation of bandstructures, SOC is applied since it is essential for the existence of topological insulators. The orbital resolved band structure plot is a projection of orbital composition on the band structure. Early signs of band inversion can sometimes be found by analysing the orbitals. Calculation of topological invariants is the determining step that confirms the topology of the material. When the material is confirmed to be TI or TCI, helical edge states that are protected by symmetry will be present on the edge of the material. Those edge states can be further analysed by plotting the edge state either through constructing nanoribbon, or through TB model.

DFT calculations are carried out with VASP software. The pseudopotential used is generated through the projector augmented wave (PAW) method [137]. Perdew-Burke-Ernzerhof (PBE) [138] exchange-correlation functional was applied. A convergence test was performed before carrying out the calculation. Zero damping DFT-D3 Grimme Method [139] was applied to approximate vdW Interaction.

The input and output for each calculation steps are listed in **Table 4-1**.

Table 4-1 General steps for topological materials calculation

Step	Input	Software	Output
Geometry Relaxation	Unrelaxed atomic structure	VASP	Optimised atomic structure
Self-consistent calculation	Atomic structure information	VASP	Charge Density file Density of states Wavefunction information
Band structure calculation	Band structure calculation	VASP	Band structure, atomic orbital information
Write Wannier90 Input	Wavefunction information	VASP/Wannier90 Interface	Wannier90 Input files
Wannier 90 calculation	Wannier90 Input files	Wannier90	Wannier TB Hamiltonian
Wannier TB Hamiltonian Post-processing	Wannier TB Hamiltonian	Wanniertool	TB bandstructure Wannier Charge Centre plot

			Surface states

4.3.2 The “Band Downfolding” Technique

The “band downfolding technique” is useful in providing tight-binding Hamiltonian for the circumstances that a thin film material is placed on a substrate. Here the term “downfold” is to extract the effective Hamiltonian of the thin film out of the bulk band information which consists of the thin film and the substrate. The DFT band structure contains both substrate and thin film information. Extracting the thin film information out of the bulk Hamiltonian not only saves time and computational resources in post-processing the Hamiltonian, but also is more relevant to the practical circumstances. The reason can be demonstrated in **Figure 4.3**, which has shown an example of plots comparing the corresponding edge configurations downfolded and un-downfolded edge states. We can identify the distinctive difference between the plots. In **Figure 4.3 (a)** shows that the edge of the thin film material deposited in the bulk substrate, which is a situation that is common in experimental deposition of 2D thin films [140]. The influence from the bulk substrate will be projected into the orbitals of the thin film. **Figure 4.3 (b)** shows that the edge of the thin film perfectly matched the substrate edge. If we use a undownfolded Wannier tight-binding Hamiltonian and calculate the edge state with the same method, we will have to assume the substrate edge matches the thin film edge, which is a model that exist only in theoretical calculation and unlikely to be created experimentally. Therefore, using a downfolded Hamiltonian is important in our calculation of Wannier edge states.

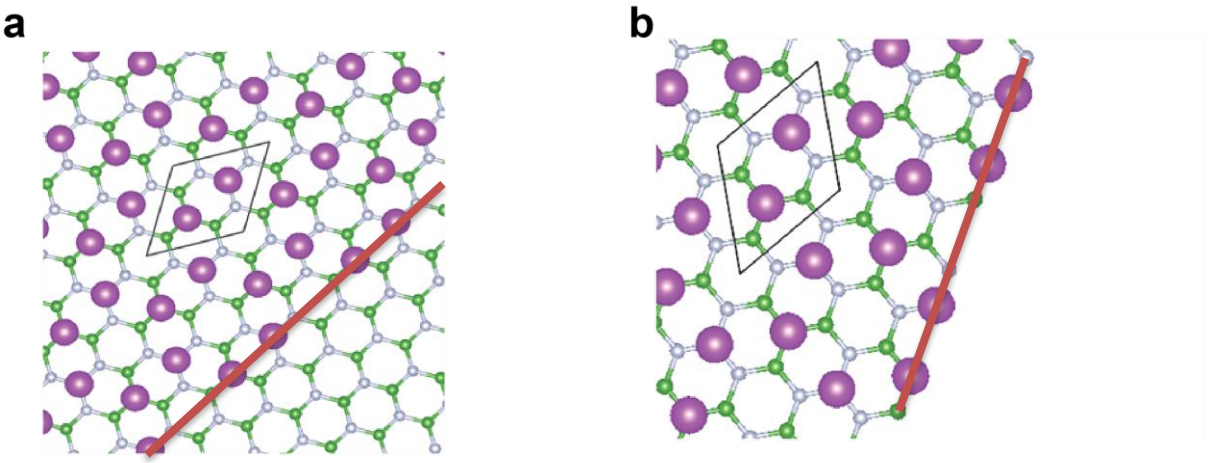

Figure 4.3 (a) Atomic structure with thin film edge bismuthene deposited on the substrate, which is more likely to appear in experimental circumstances **(b)** Atomic structure with thin film edge deposited exactly on substrate edge, which is only hypothetical. When calculating the edge states through Wannier function, **(a)** edge corresponds to the "downfolded" Armchair structure edge that only bismuth orbital is used in the edge calculation, while **(b)** edge correspond to the "undownfolded" edge band structure that both Bi and h-BN orbitals are used to calculate the edge states. The purple atom is the bismuthene thin film. h-BN substrate is under the thin film. The red line indicates the edge of the bismuthene thin film. More details on Bi/h-BN model setup can be found at **Chapter 6.2**.

The general principle of the technique is to write a Hamiltonian that contains selectively projected orbital information relevant to the material's topological properties. We have summaries the following procedures to achieve the best quality downfolded Hamiltonian for topological insulator materials on a substrate. The first procedure is to plot the orbital projected bulk band structure for both thin film and the substrate using DFT. Secondly, we need to identify the orbitals of the thin film that are close to Fermi level and record the range of the energy window that contains all those orbitals. This energy window is used as an "outer window" in writing the Wannier90 input file. The other important input "inner window" is determined by the maximum window near the Fermi level that contains only the selected orbital

information. **Figure 4.4 (b)** demonstrates an example of downfolded structure, which can be compared with the bismuth bands in DFT calculation highlighted the in red circles demonstrated in **Figure 4.4 (a).** The similar shape between the two band structures shows that the downfolding process has been completed in high quality. Only high-quality effective Hamiltonians provide consistent edge band structures.

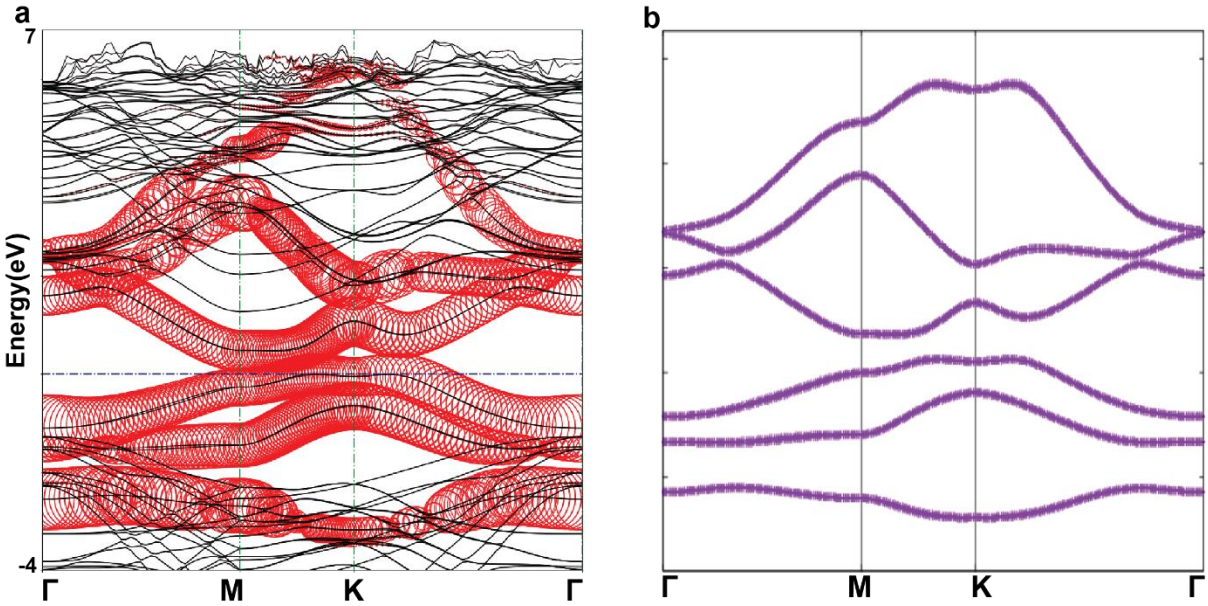

Figure 4.4 (a) The DFT band structure for Bi/SiCH-(0001) with highlighted bands contributed by bismuth atoms. **(b)** The Wannier tight-binding band structure constructed based on a projection on p orbitals extracted from Bi/SiCH-(0001) DFT calculations.

4.4 Calculation of Topological Invariants

The Z_2 topological invariant is defined in Ref. [45] as

$$(-1)^{\nu} = \prod_i \frac{\sqrt{\det\left(w(\gamma_i)\right)}}{Pf\left(w(\gamma_i)\right)}$$

where γ_i is time reversal invariant momenta. v is the Z_2 topological invariant that may have the values of either 0 or 1.

However, solving this equation requires complex mathematics. Researchers developed different methods to calculate topological invariants. In 2007, Fu & Kane [39] derived a new equation to calculate the topological invariant for materials that are inversion symmetric in their atomic structures. The calculation is based on parity analysis.

$$\delta_i = \prod_{m=1}^{N} \xi_{2m}(\Gamma_i)$$

$$(-1)^v = \prod_i \delta_i$$

where $\xi_{2m}(\Gamma_i) = \pm 1$ is the parity eigenvalue of the occupied energy band at TRIMs.

This method is only applicable in inversion symmetry systems. It helped successfully predict some important TIs, such as three dimensional Bi2Se3 [17].

4.4.1 Z_2 Invariant and Wannier Charge Centre Method

Calculation Z_2 number for all systems can be realised with tracking of Wannnier charge centre (WCC). The derivation of this method was discussed in detail in Ref. [141] and Ref. [142].

Wannier centre can be defined as centre of Wannier function $\overline{\boldsymbol{r}_n} = \langle \boldsymbol{0}n|\boldsymbol{r}|\boldsymbol{0}n\rangle$. It also corresponds to the integral Berry connection in the Brillouin Zone $\overline{\boldsymbol{r}_n} = \frac{V_{cell}}{(2\pi)^3}\int_{BZ} <$

$u_{n\boldsymbol{k}}|i\nabla_{\boldsymbol{k}}|u_{n\boldsymbol{k}} > d^3k.$, where V_{cell} is the volume of unit cell. $|u_{n\boldsymbol{k}}>$ is the cell-periodic form of the Bloch function. $\boldsymbol{k}$ is the wavevector.

In a 2D system, when only y direction is taken to the Fourier transform, a hybrid Wannier function can be defined as

$$|nk_x l_y >= \frac{a}{2\pi}\int_0^{2\pi/a} d\, k_y e^{-ik_y l_y}|\tilde{\psi} n\boldsymbol{k}>$$

Then WCC becomes $\overline{y_n}(k_x) = < \mathrm{n}k_x 0|y|nk_x 0 > = \frac{a}{2\pi}\int_0^{2\pi/a} i < u_{n\boldsymbol{k}}|\partial_{k_y}|u_{n\boldsymbol{k}} > dk_y$

$\overline{y_n}(k_x)$ also corresponds to the Berry phase at a given k_x.

Topological invariants can be calculated via tracking $\overline{y_n}$ at different k_x. An example can be found at **Figure 4.5,** where θ is a phase factor directly proportional to $\overline{y_n}$. A reference line can be drawn through k_x. In a time-reversal symmetric system, an even number of crossing points indicates a trivial insulator, while an odd number of crossing points indicates a topological insulator.

The WCC method has been applied in open-source software such as Z2Pack [143] and Wanniertools [144] to calculate the Z_2 invariant.

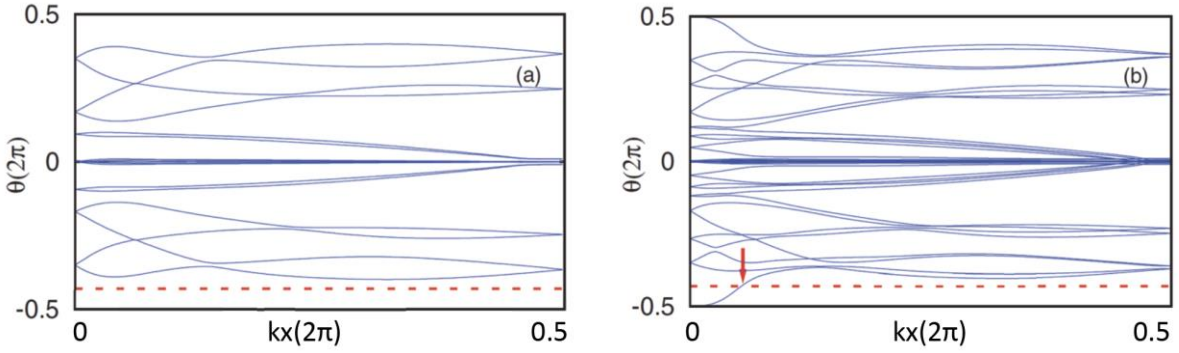

Figure 4.5 Example of Wannier Charge Centre plot taken from Ref. [142]. **(a)** shows the WCC plot for 1QL Bi2Te3 slab which is trivial insulator with Z_2 topological invariant 0. **(b)** shows the WCC plot 2QL Bi2Te3 which is a topological insulator with Z_2 topological invariant 1. The red line is a reference line crossing the WCC plot. An even number indicates Z_2 topological invariant 0, while an odd number indicates Z_2 topological invariant 1.

4.4.2 Edge States Calculation

The most general method in calculating surface states is to construct a one-dimensional nanoribbon and use DFT to plot the whole band structure. This method is very useful to account for the influence of structural deformation [145], and the effect of edge adsorption [91]. However, the large number of atoms in nanoribbon also means time-consuming and memory-intensive calculations. Also, since topologically protected surface states are robust against many perturbations, such high accuracy simulation of the real system may not be required in most circumstances. To simplify the calculation, the software Wanniertools uses iterative Green function methods associated with the input single unit-cell Wannier tight binding Hamiltonian to perform edge states calculation [144].

4.5 Tight Binding Model and Effective Hamiltonian

The tight binding model for the thin film bulk bismuthene can be written as

$$H = t\sum_{\langle ij\rangle} c_i^{\dagger} c_j + \lambda_{SO}\hat{\boldsymbol{L}}\cdot\widehat{\boldsymbol{S}} + i\lambda_R \sum_{\langle ij\rangle} c_i^{\dagger}\left(\boldsymbol{s}\times\widehat{\boldsymbol{d}}_{\boldsymbol{ij}}\right)_z c_j + H.c.$$

The first term and the third term are the same as described in **Chapter 3.3.2**, in the second term, λ_{SO}, $\hat{\boldsymbol{L}}$ and $\widehat{\boldsymbol{S}}$ stands for SOC strength, orbital angular momentum, and spin angular momentum. The detailed construction for the first part of the Hamiltonian $H = t\sum_{\langle ij\rangle} c_i^{\dagger} c_j + \lambda_{SO}\hat{\boldsymbol{L}}\cdot\widehat{\boldsymbol{S}}$ follows the principle from Ref [146]. Using previously obtained Wannier tight-binding Hamiltoninan, the hopping parameters can be obtained. For bismuth p orbital is chosen as the basis for the model. Hopping has been limited to the second nearest neighbour. The spin-orbital term λ_{SO} can be determined by DFT calculation of the structure. The model can be used to study multiple bismuth allotropes. In our case, the Rashba term $i\lambda_R \sum_{\langle ij\rangle} c_i^{\dagger}\left(\boldsymbol{s}\times\boldsymbol{d}_{\boldsymbol{ij}}\right)_z c_j$ from Kane-Mele model [47]. is added to model the mirror symmetry breaking effect. This can either be a perpendicular electric field or the substrate effect.

Chapter 5 Electronic Structure of Bismuth Allotropes

5.1 Introduction

As introduced in **Chapter 3.4**, bismuth allotropes provide us with a platform to study various types of topological features. To provide the benchmark for our calculation, this chapter begins with the part verifying the results from previous studies. This includes calculation of electronic band structures and topological features for Bi (111) thin films, planar bismuthene, and the orbital filtered bismuthene on SiC thin film which leads to the experimental realisation of a room temperature 2D TI [70]. Those results have been consistent with previous findings.

We have also included a TCI/TI edge interface states study that shows how the TI edge states dominate over the TCI edge states in planar bismuthene nanoribbon structure. The new interface states have demonstrated the resemblance to the edge states of both materials.

We focused on the electronic structures of Bi (110) in **Chapter 5.4.** The electronic structures have been compared with the experimental results from our experimental collaborator.

5.2 Electronic Structure of Bismuth Allotropes

5.2.1 Bi (111) Electronic Structures and Topological Properties.

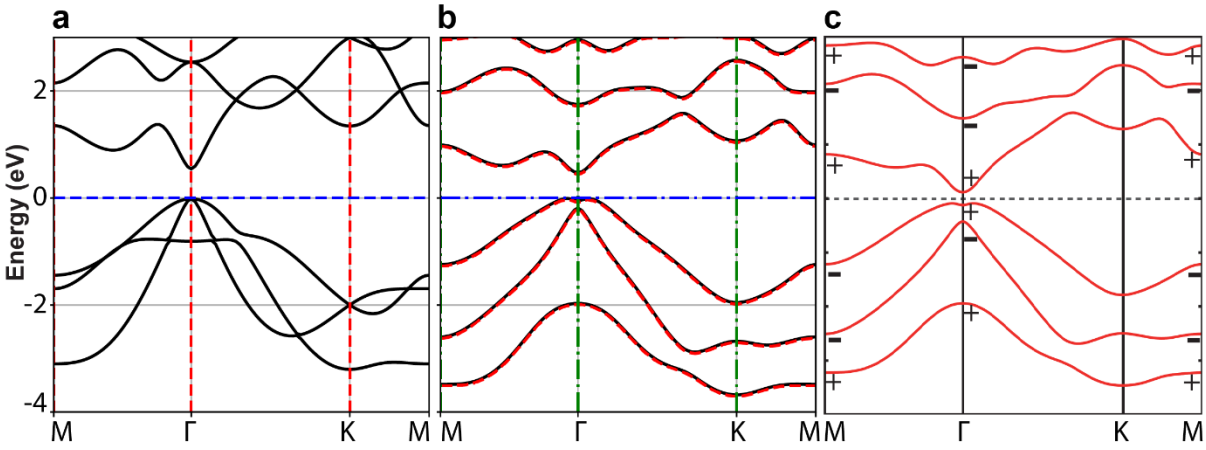

Figure 5.1 Bi (111) BL bandstructure **(a)** DFT bandstructure without SOC **(b)** DFT bandstructure with SOC printed in black lines. Wannier TB band structure with SOC printed in red dots **(c)** Band structure with SOC taken from Ref [87] .

The band structure for Bi (111) 1BL without and with SOC is shown in **Figure 5.1 (a)** and **5.1 (b)** respectively. The black lines are DFT band structure, while the red dashed line in **Figure 5.1(b)** is the Wannier TB band structure. The DFT and Wannier bandstructure in **Figure 5.1(b)** matches well with each other. The Wannier TB band structure is based on the projection on p orbitals of Bi atoms. The overlap of band structure calculated with the two methods around the Fermi level indicates the reliability of the Wannier TB Hamiltonian. The band structure shape **Figure 5.1 (b)** is consistent with **Figure 5.1 (c)** obtained from Ref [87], despite our calculation indicates a larger indirect band gap 0.48eV instead of 0.2eV. As Ref [88] has calculated 0.58eV indirect band gap for the same structure, we believe our band gap is consistent with the range of previous calculated magnitudes. By comparing **Figure 5.1 (a)** and **Figure 5.1 (b)**, we can

see that after SOC is applied, the initially entangled band structure becomes separated. At Γ point near the Fermi level, the shape of the occupied band indicates an early sign for band inversion.

As suggested in literatures [141, 142], the topological invariants can be calculated via drawing a horizontal line through the Wannier charge centre plot. An odd number of crossings indicates a non-trivial topological phase with $\nu = 1$, while an even number of crossings indicates trivial phase with $\nu = 0$. Therefore, the Wannier charge centre shown in **Figure 5.2 (b)** plot confirmed that Bi (111) 1 BL is a Z_2 topological insulator induced by SOC.

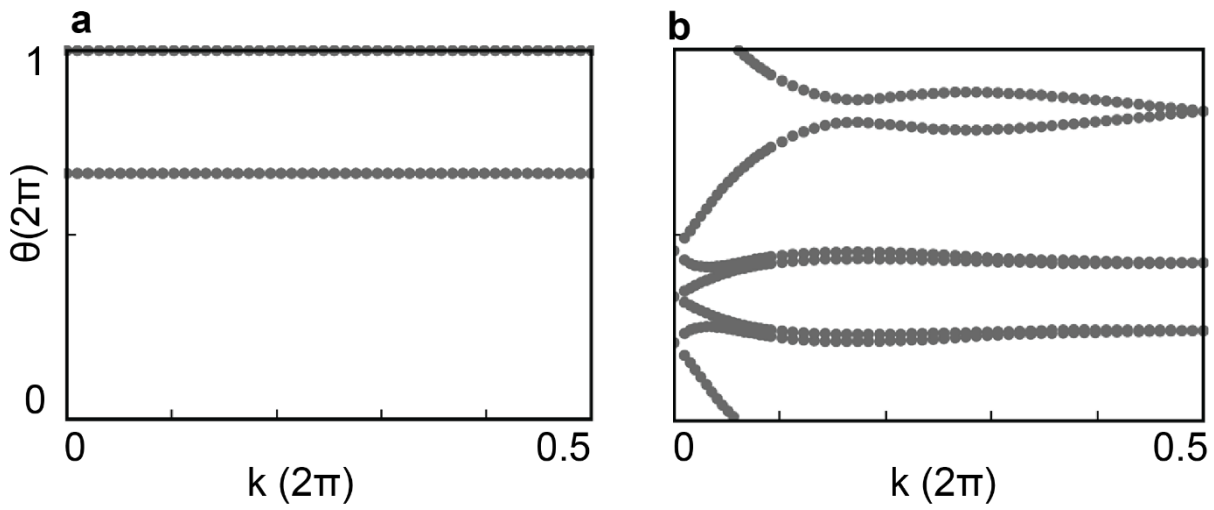

Figure 5.2 The Wannier charge centre plot under **(a)** no SOC and **(b)** with SOC circumstances.

5.2.2 Electronic Structures and Topological Properties for Planar Bismuthene

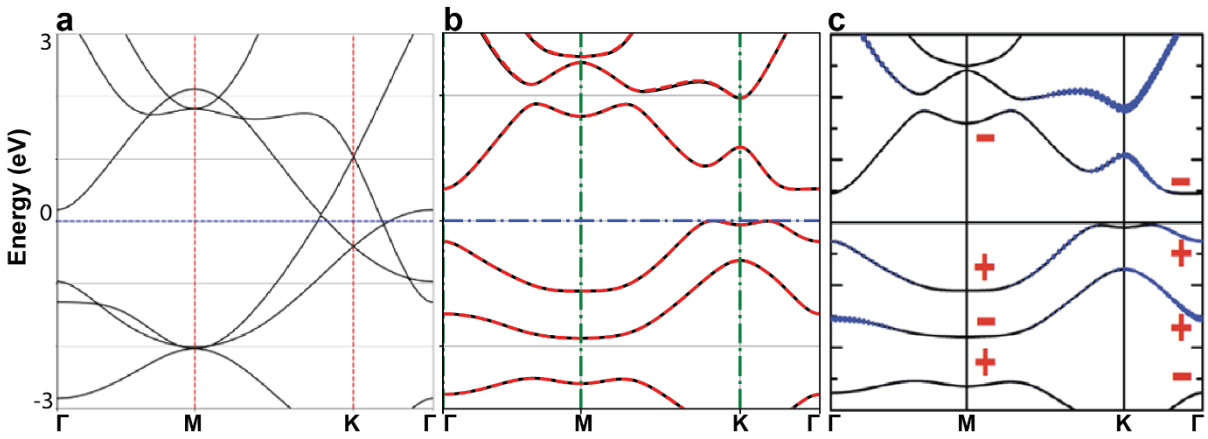

Figure 5.3 Bandstructure for planar Bismuthene **(a)** DFT band structure without SOC **(b)** DFT band structure in blacklines and Wannier TB band structure in red dotted lines **(c)** Bandstructure taken from Ref. [90].

The band structure for freestanding planar bismuthene without and with SOC is shown in **Figure 5.3 (a) and 5.3 (b)** respectively. The Wannier TB band structure (red line) matches well with the DFT band structure (black line), as well as the band structure plotted in literature [90] shown in **Figure 5.3 (c).** The band structure without SOC has Dirac cones at Fermi level. After SOC was applied, the degeneracy was lifted.

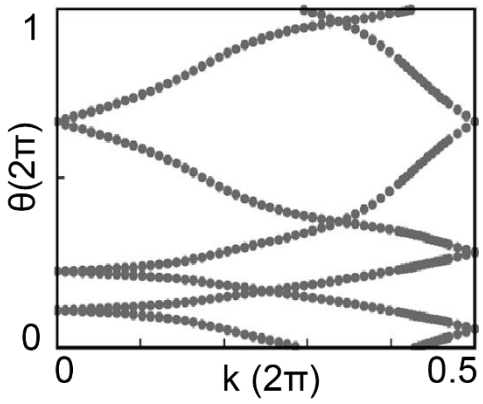

Figure 5.4 Wannier charge centre plot for freestanding bismuthene with SOC.

As shown in **Figure 5.4**, the WCC plot has two crossing points with a horizontal line, which indicates that the material is Z_2 trivial. Therefore, the material is not protected by time-reversal symmetry. However, the pattern of this WCC plot is different from the usual non-trivial WCC plot. It can be explained with the condition of the WCC loop with WCC winding the cylinder twice. As described in Ref [142], the degeneracy is usually lifted by perturbation (indicated with point P in **Figure 5.5**). However, as shown in **Figure 5.4**, the degeneracy is maintained. The WCC plot indicates there might be symmetry other than TRS that protects the degeneracy. This is consistent with previous studies that the material is a TCI [77].

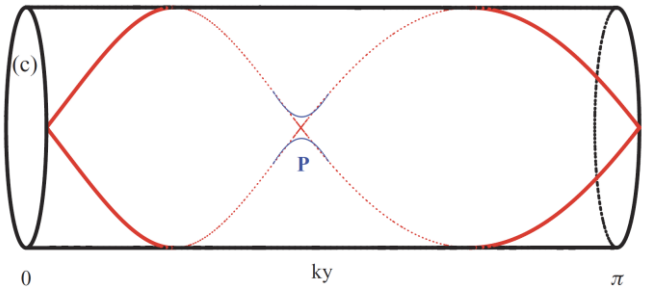

Figure 5.5 Illustration of WCC windling the cylinder twice. Usually, the degeneracy is lifted at point P. Graph taken from Ref. [142].

The edge states of freestanding bismuthene will be discussed in detail in **Chapter 6.3.1.**

5.2.3 TCI/TI Interface States

The TI model constructed here we used here is BiF. It has been reported BiF is a 2D TI with a large bandgap [101]. The TCI applied here is freestanding planar bismuthene. The nanoribbon constructed here for BiF is $8 \times 1 \times 1$ and for freestanding bismuthene monolayer is $10 \times 1 \times 1$. The edges for both nanoribbons separated with 40 Å vacuum to make sure there are no interactions between each edge. The single unit-cells are fully relaxed without SOC while the nanoribbons are frozen to simplify the calculation. BiF and freestanding bismuthene have the relaxed lattice constant of 5.26 Å and 5.27 Å respectively. Then the TCI and TI nanoribbons are connected to construct a TCI/TI interface. Constructed nanoribbons are shown in **Figure 5.6**.

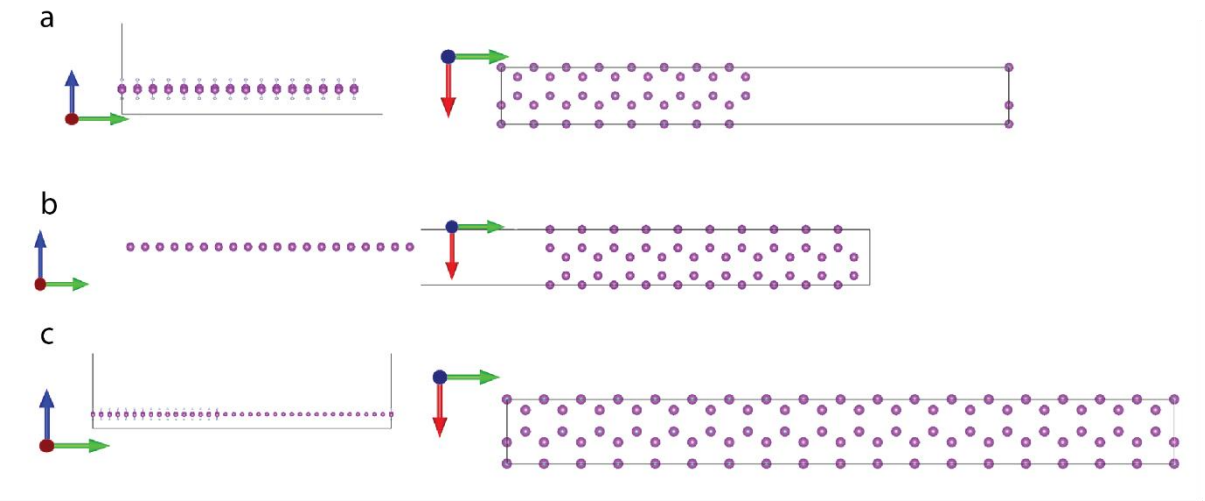

Figure 5.6 Construction of nanoribbons. **(a)** 8 × 1 × 1 BiF nanoribbon **(b)** 10 × 1 × 1 freestanding bismuthene **(c)** BiF/Bismuthene interface.

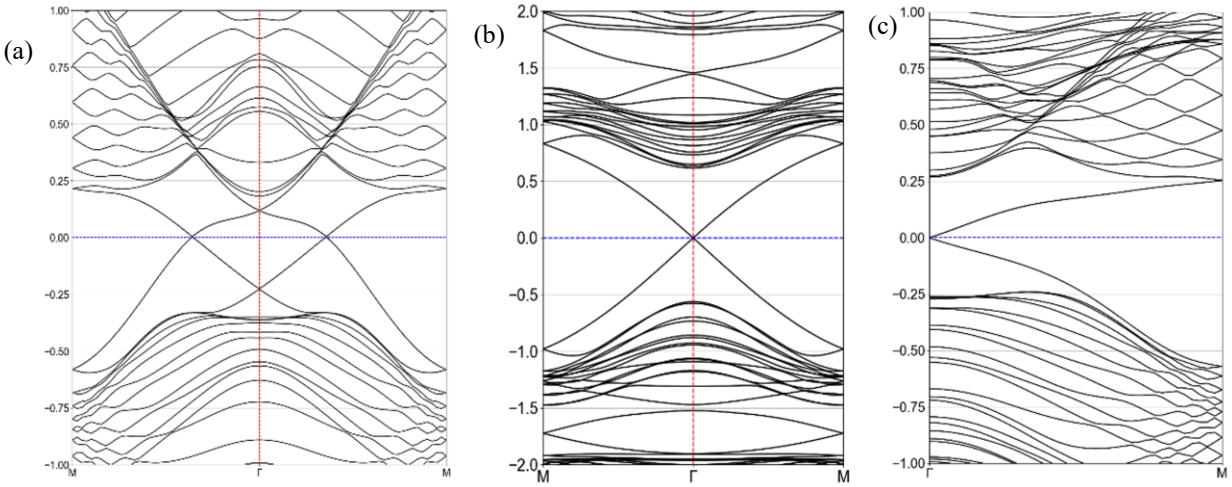

Figure 5.7 (a) Freestanding planar bismuthene armchair band structure **(b)** BiF edge band structure **(c)** BiF/Bi Interface band structure.

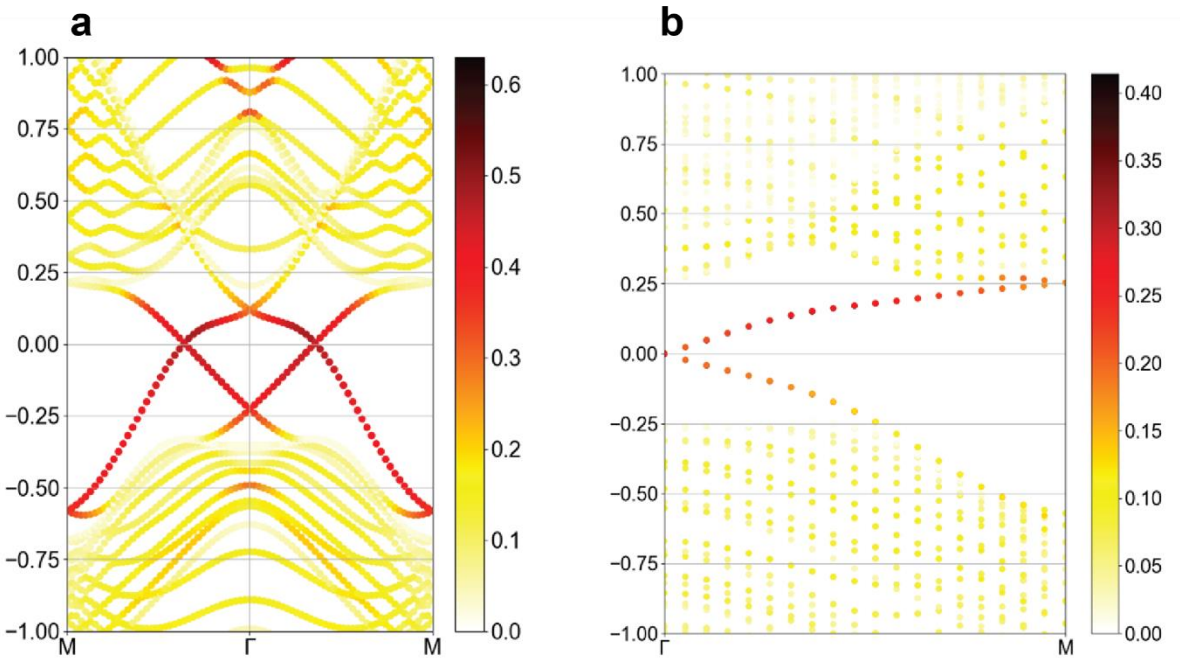

Figure 5.8 (a) Freestanding planar bismuthene bandstructrue showing the weights of the edge bismuth atom. **(b)** BiF/Bismuthene interface bandstructure showing the weights of edge bismuth atom on bismuthene side.

The BiF nanoribbon edge states, freestanding planar Bismuthene edge states, and the BiF/ Bismuthene interface states are plotted in **Figure 5.7**. BiF is a TI with an odd number of Fermi level crossing, while freestanding planar Bismuthene is a TCI with an even number of Fermi level crossing. The TCI/TI interface maintains a single number of Fermi level crossings, which may suggest that the topological insulator edge states protected by TRS are maintained. The reason that the TCI edge state feature is not seen in the interface could be the breaking of crystalline symmetry at the interface. Interestingly, the projected orbital in **Figure 5.8(b)** shows that the edge states near the Fermi level are contributed by the edge atoms of the freestanding bismuthene instead of the edge atoms of BiF. As shown in **Figure 5.8(a)** without the influence from the topological insulator BiF, the edge states of freestanding bismuthene originally

contribute edge states with two Fermi-level crossings between TRIMs. In addition, although the Bi/BiF interface states have a shape similar to the BiF TI edge states, the states sit well within the Bismuthene TCI bulk band gap. The interface states cross the M point at an energy level at about -0.6eV and 0.25eV, which is similar to the bismuthene TCI states. BiF TI edge states cross the M point at about -1.0eV and 0.6eV, which is a lot wider than the interface states. Therefore, we conclude that the TCI/TI edge states in Bi/BiF have obtained the feature of the edge band number and shape from the TI, while incorporating the energy range feature of TCI.

5.3 Bismuthene on SiC (0001)

5.3.1 Material Structure

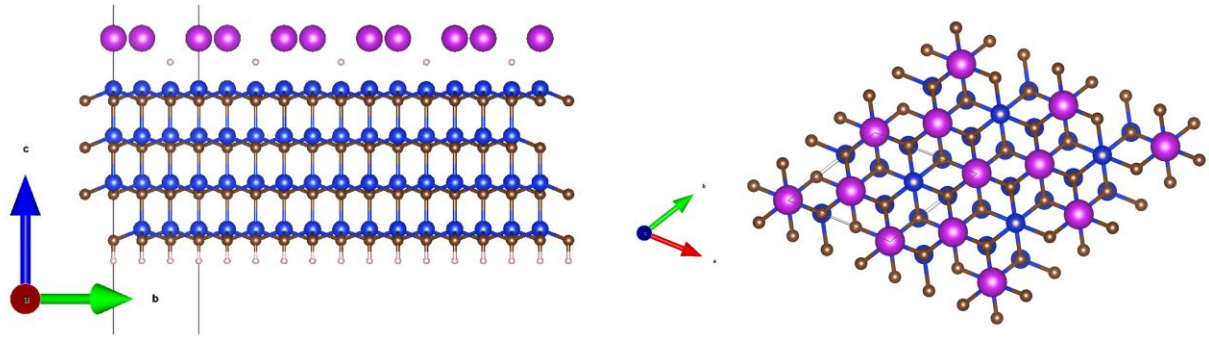

Figure 5.9 Bi on SiC (0001) a structure constructed for DFT calculations.

The structure of planar Bismuthene on SiC (0001) is presented in **Figure 5.9**. The structure was relaxed with the lattice constant of bismuthene fixed at the lattice constant of SiC (0001). Each two of the three silicon atoms are bonded with two bismuth atoms. The other is passivated with a hydrogen atom.

5.3.2 Band Structures

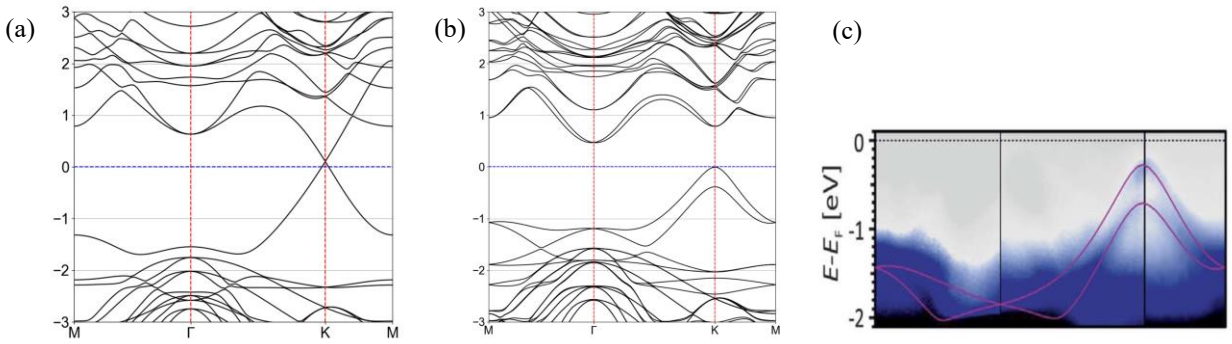

Figure 5.10 Band structure for planar bismuthene on SiC (0001) surface under circumstances **(a)** without SOC and **(b)** with SOC compared with **(c)** calculations and ARPES experiments from Ref. [70].

The band structure of planar bismuthene on SiC (0001) is plotted in **Figure 5.10**. The result is consistent with both the calculation and the ARPES result from the literature [70]. There is a Dirac cone at K point when SOC is not applied. When SOC is applied, a band gap opens at the K point. Strong Rashba splitting of bands is also observed near the Fermi level.

5.3.3 Orbital Filtering Effect

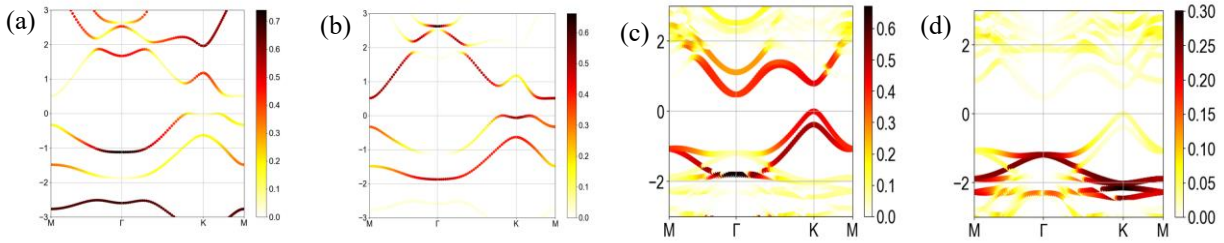

Figure 5.11 Freestanding planar bismuthene showing orbital weight from **(a)** bismuth px+py orbitals **(b)** bismuth pz orbitals. Planar bismuthene on SiC(0001) showing orbital weights from **(c)** px+py orbital and **(d)** pz orbital.

The orbital projected bandstructure for freestanding planar bismuthene and planar bismuthene on SiC (0001) is plotted in **Figure 5.11**. In the freestanding planar bismuthene film with SOC, px, py and pz orbitals are all located around the fermi level. When deposited on substrates, the px and py orbitals are still located near the Fermi level, while the pz orbital is removed from the Fermi level. This is consistent with the prediction of literature [70] that the pz orbtial is filtered by the substrate as the dangling bonds on Si surface interact with bismuth atoms.

5.4 Comparison of Bismuth (110) Electronic Structures with Experiments.

5.4.1 Material and Atomic Structures

Bismuth (110) is the material with a phosphorene structure. Unlike other bismuth-based materials, the material is defined by a rectangular lattice. The BP and DBP structures are varied by a height difference Δh within one monolayer. For 2ML structure Δh is 0.495 Å is our

calculation, which is at a similar level with the 0.45 Å in Ref [109]. Our calculation also shows that in freestanding form, The DBP structure (**see Figure 5.12(b)**) is more stable than the BP (**see Figure 5.12(a)**) structure, with the energy difference of only 0.002eV/ Bi atom.

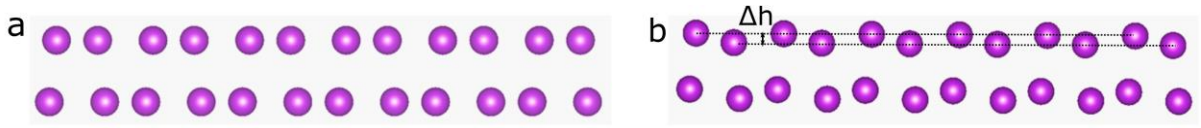

Figure 5.12 Bi (110) thin film **(a)** BP structure **(b)** DBP structure.

Due to different use of functionals and our choice to apply SOC during relaxation, the simulation results are slightly different against previous simulations. The previous simulations and the experimental results lattice parameters are shown in **Table 5-1**.

Table 5-1 Lattice parameters of Bi (110) from various sources comparing with our results. Bold font indicates my results, while simple font indicates the results from current literatures. The "features" column refers to the substrate used in the experiments, or the thin film structure used in the simulations. All the simulations here are without substrate.

Structure	**Features**	**a (Å)**	**b (Å)**	**Source**
2-4ML (experimental)	on Si (111)	4.5±0.2	4.9±0.2	Ref [107]
2ML (experimental)	on HOPG on MoS2	4.40 4.53	4.78 4.87	Ref [109] Ref [147]
2ML (Simulation)	BP DBP	4.43 4.38	4.74 4.54	Ref [109]
4ML (Simulation)	BP	4.43	4.93	Ref [148]
2ML (Simulation)	**BP** **DBP**	**4.60** **4.57**	**4.87** **4.78**	**DFT calculation**
4ML (Simulation)	**BP**	**4.60**	**4.84**	
6ML (Simulation)	**BP**	**4.60**	**4.87**	

As shown in **Figure 5.13**, despite the fact all the relaxed structures adopt a DBP structure with Δh approximately 0. There is a tendency of increase from 0.0002 Å - 0.0008 Å in 2ML structure to 0.005 Å - 0.023 Å in 6ML structure. At 6ML the height differences within the outer 2-layer atoms are higher than the inner 2 layers. However, all the height differences we studied here are significantly below the Δh (~0.5 Å) in a typical BP structure.

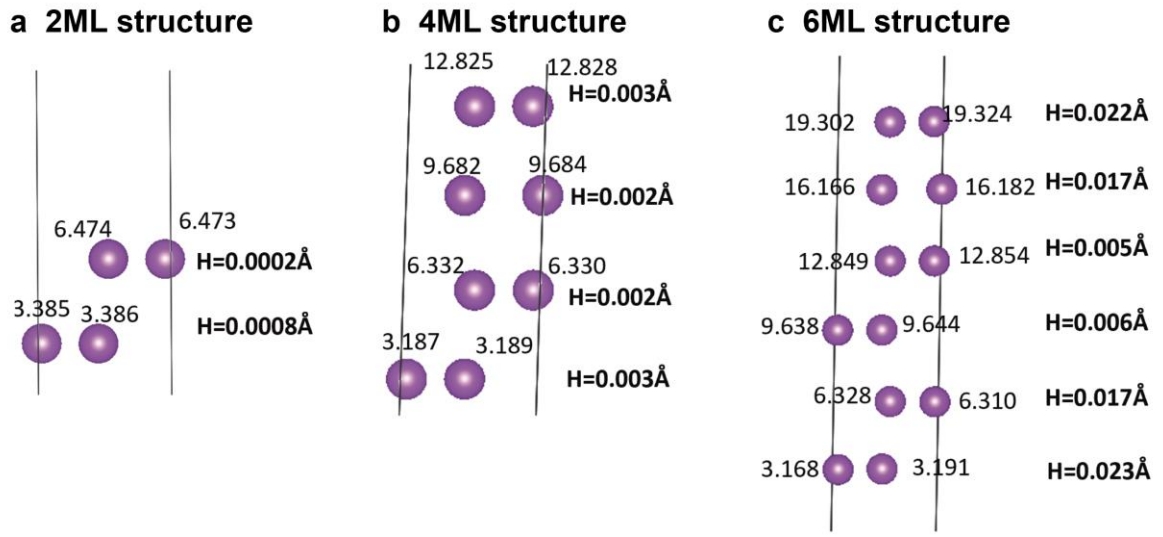

Figure 5.13 The position of atoms for Bi (110) structure for **(a)** 2ML, **(b)** 4ML and **(c)** 6ML thin films. The numbers indicate the absolute height (with arbitrary 0 point). The height difference between each layer of bismuth atoms is recorded in bold letters and numbers. H measures the atomic corrugation for each atomic layer. The oblique lines represent the axis of the unit cell, while the atoms height are measured vertically comparing the position of the atoms within one monolayer.

5.4.2 Electronic Structure

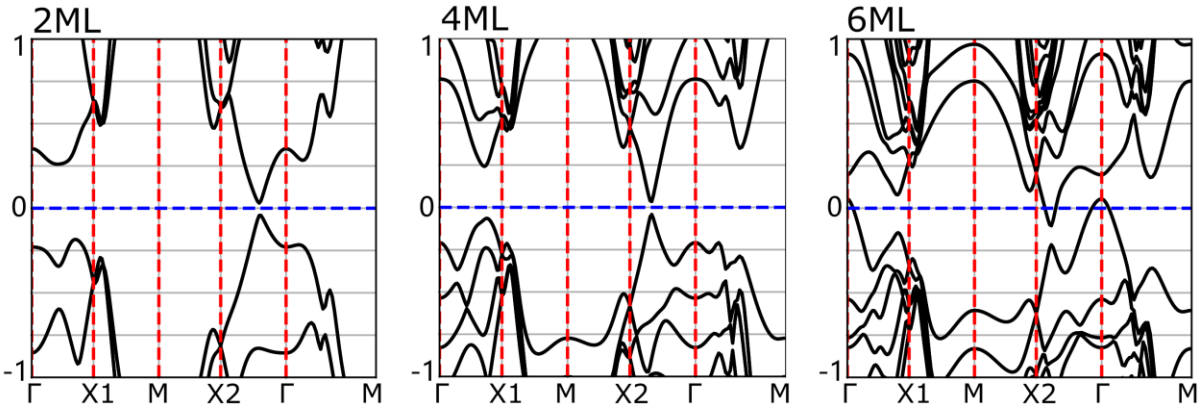

Figure 5.14 The bulk band structure calculated in 2ML, 4ML and 6ML Bi (110) thin films.

The electronic structure for 2ML, 4ML and 6ML Bi (110) is shown in **Figure 5.14.** Both 2ML and 4ML band structure shows a direct band gap between X2 and Γ. The bulk band gap for both 2ML and 4ML in our calculation is 70meV. The band structure calculated has a similar shape with previous studies, despite the slight variation in band gap calculation. (100meV for 2ML and 59meV for 4ML in previous studies [109]). For 6ML Bi (110), the valence band at Γ point are pushed up, resulting in the closure of the indirect band gap, which is consistent with previous results in [109].

5.4.3 The Nontriviality of Bi (110) Edge States

The Wannier projected edge states plot for 2ML 4ML, and 6ML Bi (110) thin film along different edge orientations is presented in **Figure 5.15.** The corresponding orientation is also illustrated. For all configurations, the edge states exist and continuously connect valence band with conduction band, which is consistent with the conclusion the material is topologically protected. The edge states for 2ML and 4ML sit within the 70 meV bulk band gap, while as a semimetal, the 6ML thin film hosts the edge states within its indirect band gap.

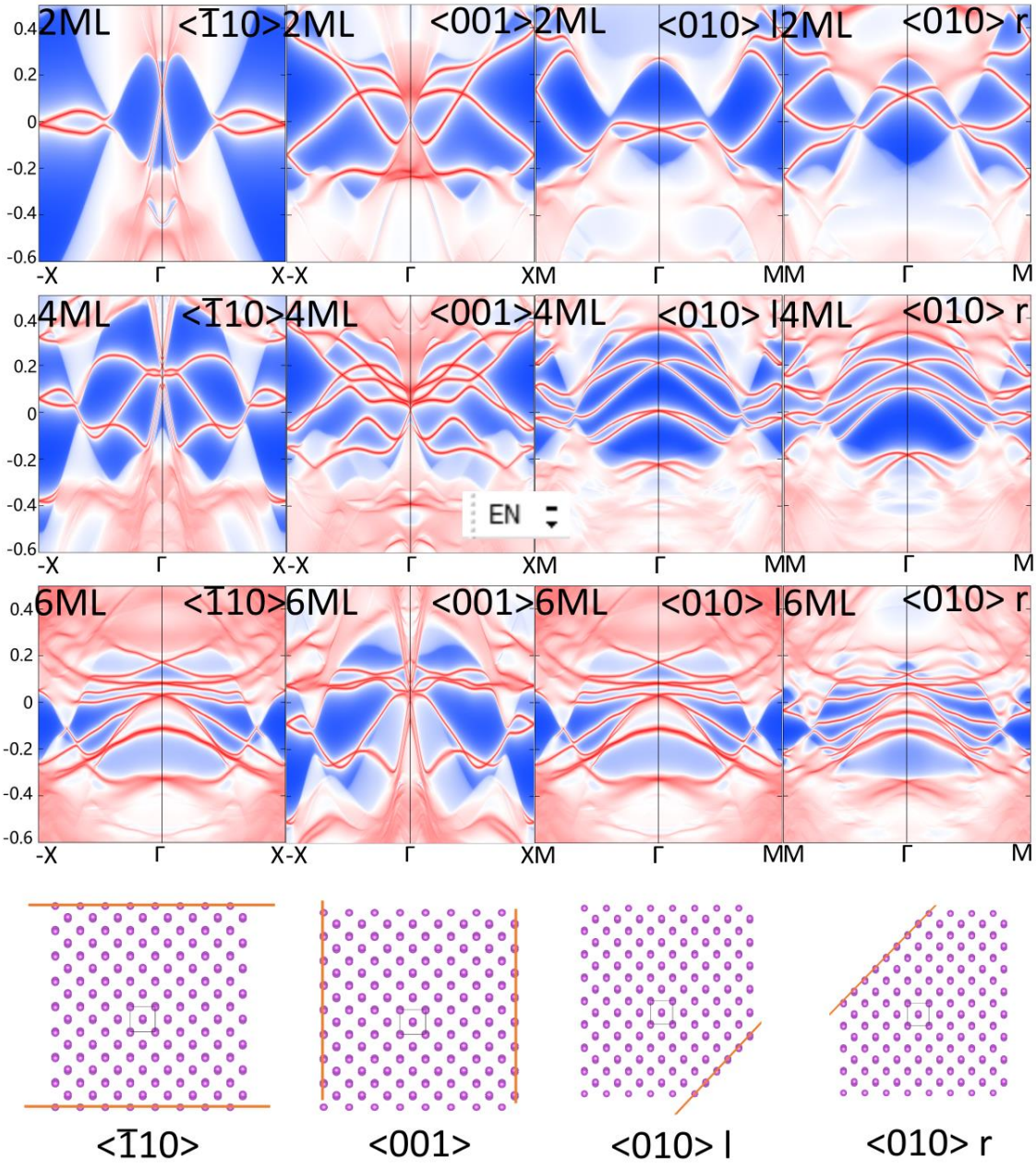

Figure 5.15 Wannier edge states plot along various edges for 2ML, 4ML and 6ML Bi (110) thin films.

The 2ML, 4ML, and 6ML Wannier Charge Centre plots are plotted in **Figure 5.16.** The continuous evolution of WCC proves the nontriviality of the 2ML, 4ML, and 6ML edge states.

The red line has an odd number of crossing points throughout all three samples, indicating the Z_2 number $\nu = 1$ for 2ML, 4ML and 6 ML Bi (110) thin films. This is consistent with previous studies calculated the Z_2 number using parity method [109].

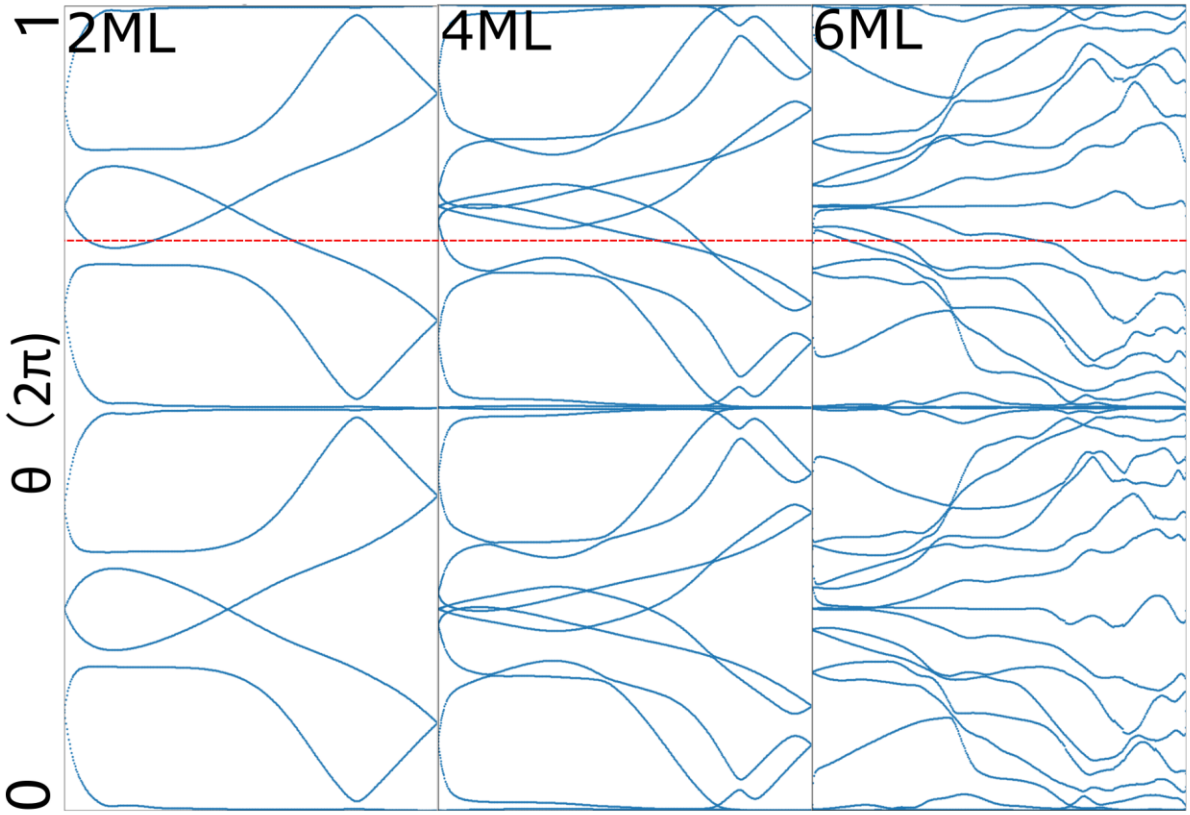

Figure 5.16 Wannier Charge centre plot for 2ML, 4ML and 6ML Bi (110) structures. The red line crosses all three plots an odd number of times. This indicates the Z_2 non-triviality for all three structures.

5.4.4 Features of Bi (110) Edge States Comparing with Experimental Results

In this study, 2ML and 6ML nanoribbon models have been constructed. The edge atoms are numbered according to the distance from the edge**.** In our density of states calculations, the

contribution from both sides of the edge will be added up. For all of the samples, we have relaxed the outmost atom in the edge following the strategy from previous DFT studies on 2ML samples in Ref [109].

Our experimental collaborators have mapped out the density of states of various configurations of Bi (110) edges. To compare with their configurations, we have built five models. The 2ML, 4ML and 6ML nanoribbon, 2ML island + 2ML substrate, and 2ML island + 4ML substrate structure are constructed and used to model the various features that exist in experiments. The 2ML nanoribbon is similar but longer than the 2ML model built-in [109], where only the outmost layer of the edge atom is relaxed. The 4ML and 6ML nanoribbons are relaxed following the same strategy. However, for the 4ML and 6ML nanoribbon, the edge reconstruction took place, making the dangling atom sit between the top 2ML and the bottom substrates. Our models used to conduct the nanoribbon calculation is shown in **Figure 5.17**. Using first-principles calculation, we have plotted the contribution to density of states (DOS) for each atom from the outmost atom to the atoms inside. The atoms are numbered according to the distance from the edge. The innermost atom is atom 16, which is about 2nm inside the edge. The 2ML sample DOS calculation compared with experimental results is shown on **Figure 5.18.** We have identified 5 peaks in the experimental results that correspond to the peaks identified in our first-principles calculation. Three peaks are marked green, which corresponds to the peaks throughout all atoms. Two peaks away from the Fermi level are marked yellow, which corresponds to the peaks away from the edge. The edge-specific features are not observed. Therefore, we conclude that the experimental measurement for 2ML nanoribbon has been reflecting the bulk features instead of edge features.

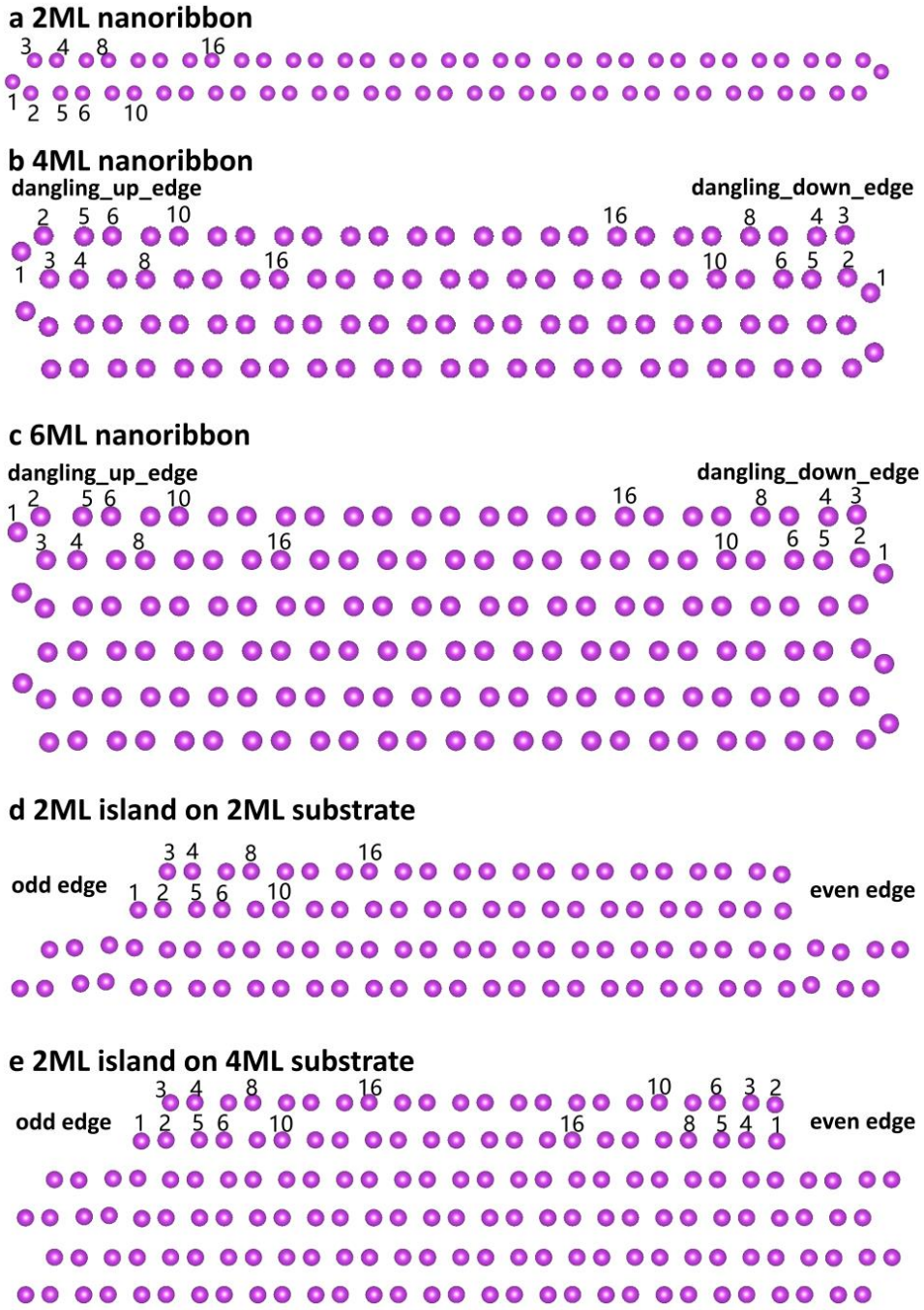

Figure 5.17 Configurations used for Bi (110) nanoribbon calculation. The three configurations are **a** 2ML nanoribbon **b** 4ML nanoribbon and **c** 6ML nanoribbon **d** 2ML island on 2ML substrate **e** 2ML island on 4ML substrate. In **b** and **c** both the dangling up and dangling down edges are studied. In **d** and **e** both odd and even edges were studied.

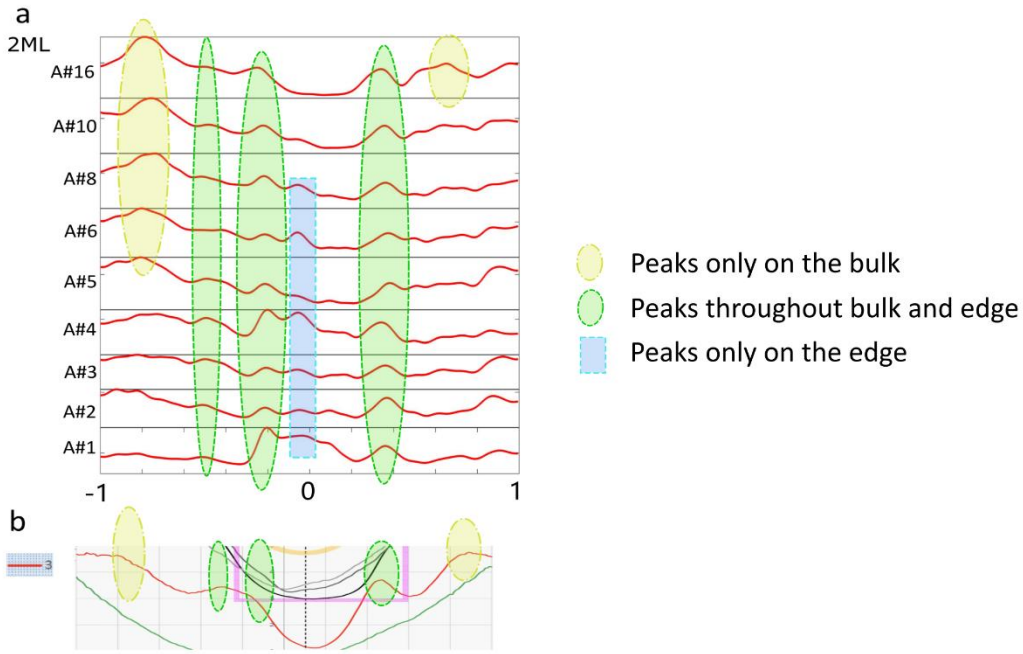

Figure 5.18 a Density of States plot for 2ML nanoribbons for selected atoms (numbered according to **5.17(a)**). **b** Experimental density of states plot for 2ML nanoribbon.

The noise level for both the 4ML nanoribbon and 4ML island configurations have a high edge density of states and is hard to identify. However, the blue region in the experimental figure shows there is a difference between the edge DOS and bulk DOS, which corresponds to the peaks decaying from atom 1 to atom 5. Both the up and down configurations show similar features. With a lack of peaks, it is hard to identify which edge configuration contributed the most to the DOS. For the bulk states (atom 16) in all 4ML nanoribbon configurations as shown in **Figure 5.19a** and **Figure 5.20a**, the position of three peaks (covered in green colour) below Fermi level corresponds well to the three peaks tested in the experimental figures.

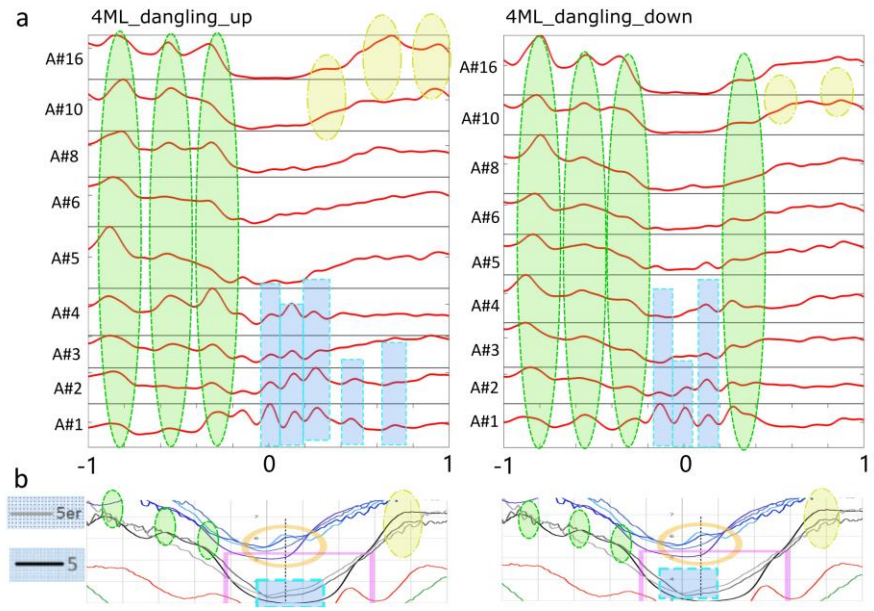

Figure 5.19 a Density of states plot for 4ML nanoribbons for selected atoms (numbered according to **5.17(b)**. **b** Experimental density of states plot for 4ML nanoribbon.

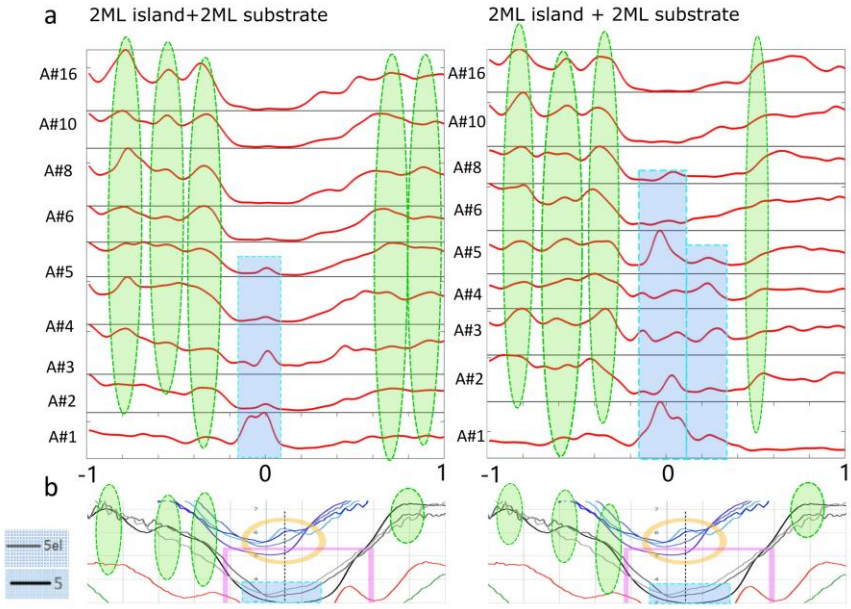

Figure 5.20 a Density of States plot for 2ML nanoribbon + 2ML substrates for selected atoms (numbered according to **5.17(d)**). **b** Experimental density of states plot for 2ML nanoribbon + 2ML substrates.

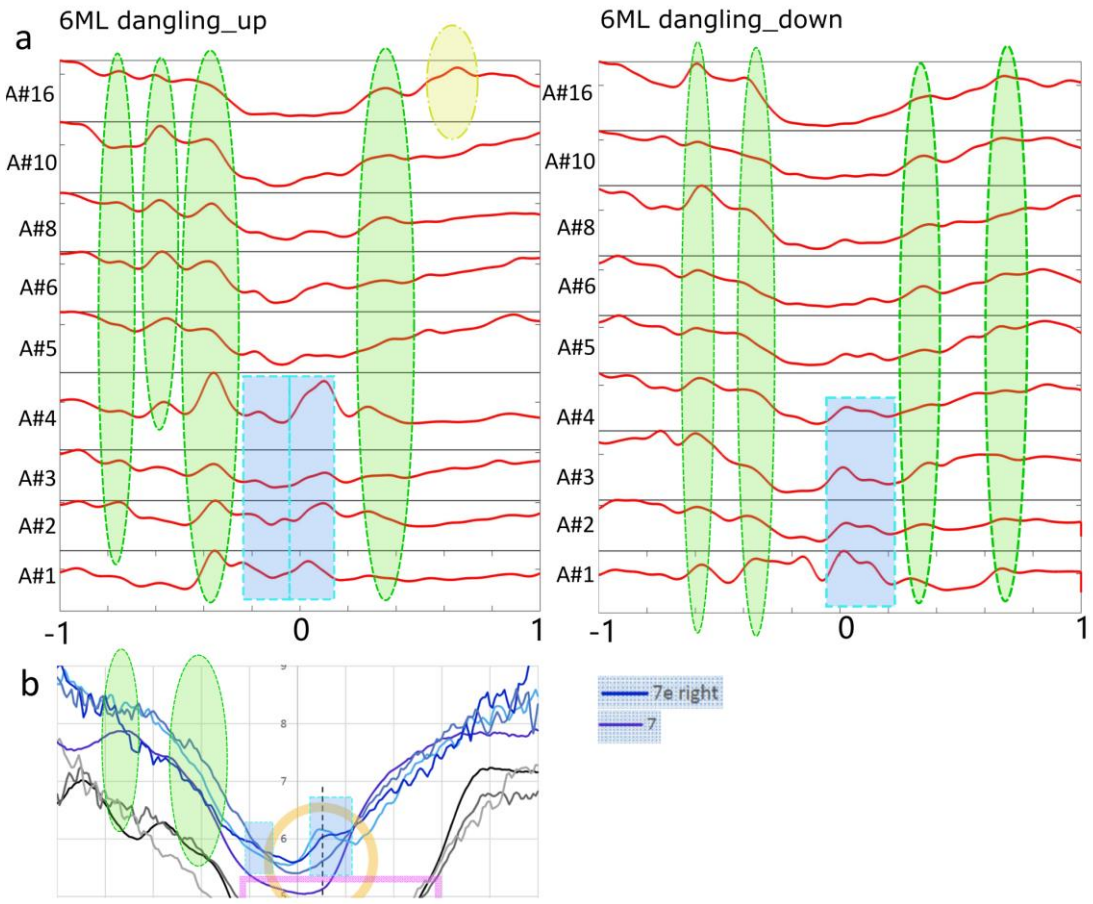

Figure 5.21 a Density of States plot for 6ML nanoribbons for selected atoms (numbered according to **5.17(c)**. **b** Experimental density of states plot for 6ML nanoribbon.

The experimental DOS plot is shown in **Figure 5.21 (b)** demonstrates the difference between the edge and bulk states around Fermi level. Two peaks can be identified near Fermi level. The shape and level resemble the calculated DOS of 6ML dangling up the structure (see **Figure 5.21(a)).** This suggests the structure is contributed by the dangling up structure shown on the left edge of **Figure 5.17(c).** Two peaks below in the experimental bulk states are identified and can be contributed by the three peaks in the calculated DOS.

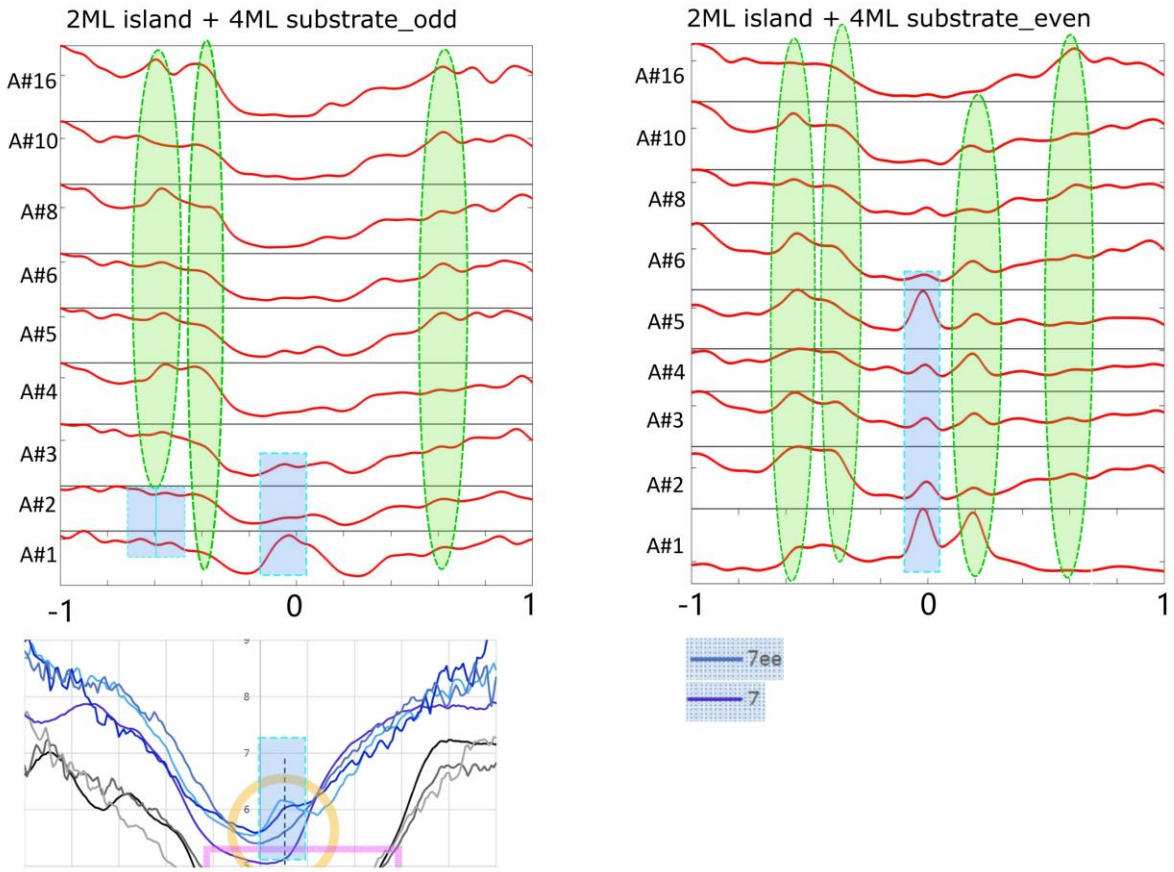

Figure 5.22 a Density of States plot for 2ML island + 4ML substrate nanoribbons for selected atoms (numbered according to **5.17(e)**. **b** Experimental density of states plot for 2ML island + 4ML substrate nanoribbon.

The 2ML island + 4ML substrate experimental structure (see **Figure 5.22 (b)**) has shown a difference of DOS peaks compared with bulk DOS. However, the peaks are not significant enough to be observed. That could be explained by the non-significant peak distribution from Atom #2 to atoms inside the bulk. The experimental DOS failed to capture the peaks in atom

#1 as shown in blue columns below Fermi level in **Figure 5.22 (a)**. The results here give an indication of how deep the measurements are inside the edge.

5.4.5 The Depth of Measurement into the Edge

Multiple peaks have been calculated for all configurations in **Chapter 5.4.4**. However, the experimental setup has only picked up a few of the peaks. One reason is that the measurement was taken at a certain depth into the edge and while the edge states can spread through a range of depth. To determine the range of edge peaks that can be reflected in the measurement, we compared the DOS as a function of depth into the edge at the energy level -0.2eV, 0, 0.1eV, and 0.356eV. At all those four energy levels, the 2ML peaks have the most significant DOS contribution near the end of the edge (see **Figure 5.23(a)**). However, this feature is missed in the experimental DOS data because at the energy 0 to 0.1 the experimental results show low DOS (see **Figure 5.23(b)(c)**). Thus, we can conclude that the experimental setup did not capture the features near the end of the edge. At around 4Å, the 2ML configurations host peaks at energy level -0.2 and 0.356(see **Figure 5.23(a)(d)**), which are captured by the experimental results. The peak of the 2ML+4ML substrate at 0.1eV (see **Figure 5.23(c)**) is also captured by the experimental measurement. Therefore, from the overall results, the region of DOS that is most likely to be captured by the experiment is the depth into the edge around 4Å.

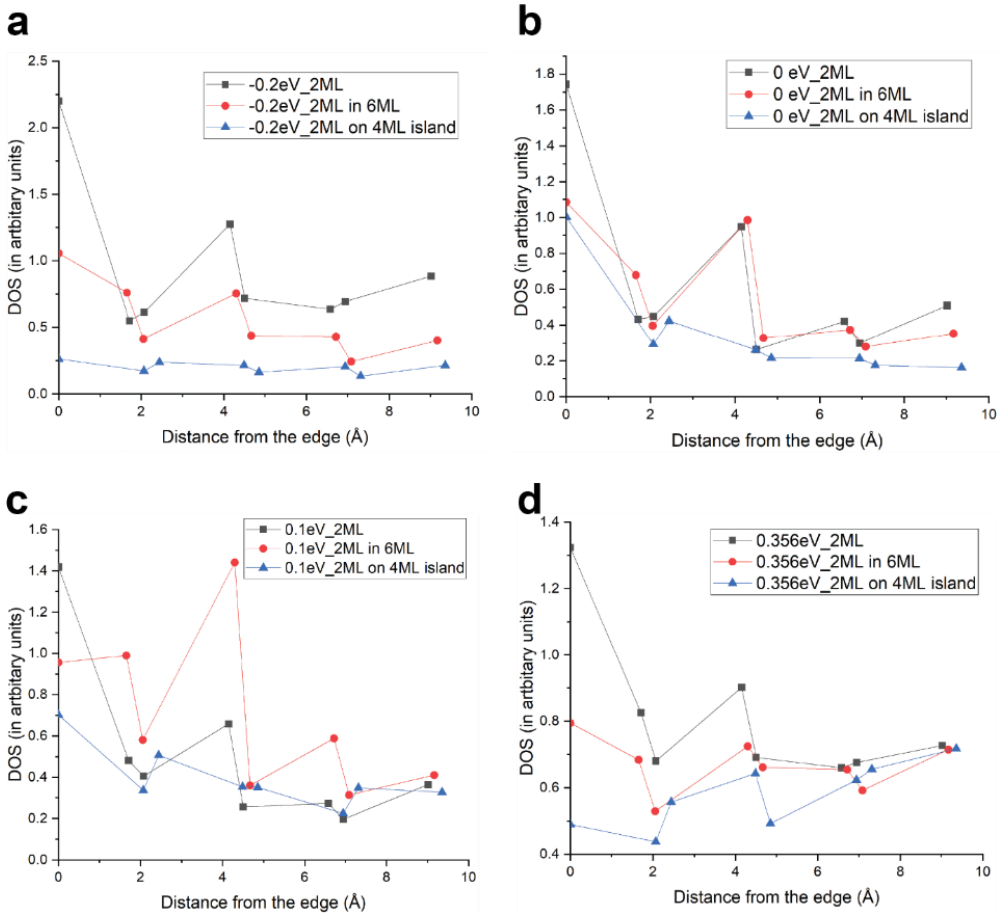

Figure 5.23 DOS vs distance from edge for 2ML, 2ML in 6ML, and 2ML on 4ML island nanoribbon structures at the energy level **(a)** -0.2eV**, (b)**0eV, **(c)**0.1eV and **(d)** 0.356eV

5.5 Conclusions

In this chapter, we have confirmed the electronic structure and topological structure for Bi BL (111) film, Bi/SiC(0001) film, and Bi (110) thin films. Those properties have been proved consistent with previous studies. The Bi/BiF interface study on nanoribbon has demonstrated that the interface state retains features from both TI and TCI edge states. While most current studies focused TI, or TCI edges along, combining the edge features can be a useful strategy in future electronics design to tune the edge transport. The Bi (110) experimental results have

been compared with our calculation. The peaks from experimental and computational results have been matching with each other at 4 Å into the edge. This can be used as a future reference for the experimental detection for the materials' topological edge states.

Chapter 6 Robustness of Bismuthene Edge States on Substrates

6.1 Introduction

The recent progress in the field of two-dimensional Quantum Spin Hall Insulators (2D QSHI) points to a promising direction for developing future electronic and spintronic devices with low energy consumption [23]. 2D QSHI is a material defined by its bulk-edge correspondence, which means that the bulk band topology can lead to the existence of topologically nontrivial edge states. The edge states are protected against non-magnetic perturbations such as disorder and backscattering [149] as long as certain symmetries are preserved. Although theories have indicated that nontrivial band topology can exist in a wide range of materials [44], realizing the fabrication of topological electronic devices still meets many practical challenges. A desirable topological material should have strong spin-orbit interactions with a large band gap near the Fermi level, and should be stable when interacting with substrates. These requirements pose critical challenges for searching for a 'real' topological material used in low-energy electronic devices.

Bismuth and its compounds have demonstrated their potential to have record-high band gaps [70, 150]. Planar bismuthene is a TCI with edge states protected by mirror symmetry [151]. However, the edge states are generally considered not robust and are sensitive to mirror symmetry-breaking substrates [152]. Here we have tested the stability of these edge states

under the influence of different substrate setups using first-principles calculations and Wannier function-based tight-binding models. We have found that choosing a substrate that has a weak interaction with bismuthene or using a sandwich stacking of substrates, could result in stabilized edge states in 2D TCIs. We have also identified that with certain edge terminations, the spin filtered edge states of 2D TCI survive the mirror symmetry breaking field, making it possible to achieve TI-like phases on a strong mirror symmetry breaking substrate. These results have reaffirmed that TCI can be a potential candidate for achieving a convenient switch of electronic states in nanodevices.

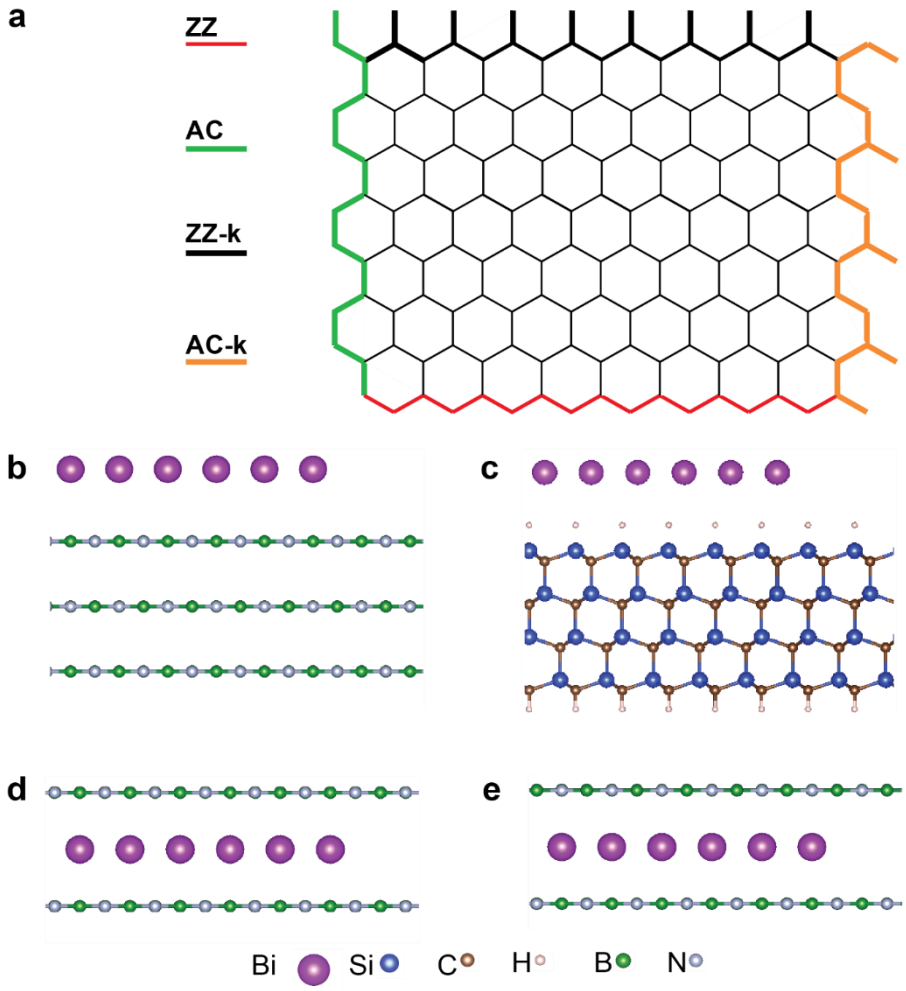

Figure 6.1 (a) Scheme for edges studied for thin film bismuth. And illustration for substrate, thin film, with the edge exposed on the right for **(b)** bismuthene on h-BN structure **(c)** bismuthene/SiCH-(0001) structure **(d)** h-BN/bismuthene/h-BN structure. These models will be used in **Chapter 6** and **Chapter 7**.

6.2 Computational Setup and Model Construction

We used first-principles calculations as implemented in the software VASP [124, 125]. The PBE [138] form of the GGA [123] is used to describe electron exchange and correlation. The energy cut-off was set to at least 500eV. All structures are fully relaxed until the ionic forces

on atoms are less than 0.01 eV/Å. The vacuum is set to be at least 30 Å to avoid the interaction between layers. A dense 21×21×1 kpoint grid was applied to sample the Brillouin Zone for accurate calculations of electronic structures. Wannier 90 [134] was used to generate Wannier tight-binding Hamiltonians, which are extracted for the calculation of topological edge states. The Hamiltonians are constructed with bismuth px, py and pz orbitals, with the effect of substrate incorporated into the model via the downfolding method [153, 154]. The software WANNIERTOOLS [155] was applied to perform edge states calculations based on iterative Green function methods.

In this research, we study the edge states for both freestanding bismuthene and bismuthene supported on different substrates. In terms of edge state calculations, we test on four different edge terminations, namely Zigzag (ZZ), Armchair (AC), Zigzag edge with Klein defect (ZZ-k) [156] and Armchair edge with Klein defect (AC-k) [156, 157]. The four types of edge are shown in **Figure 6.1(a)**. The last two modes are directly modified from conventional ZZ and AC edges by adding another atom per unit cell. Because the Klein edges contain additional dangling bonds compared to ZZ and AC, they are useful to investigate whether edge states can be protected in the presence of defects. The two types of substrates examined are hexagonal boron nitride (h-BN) and hydrogen passivated silicon carbide (SiCH-(0001)), which are shown in **Figure 6.1(b)** and **Figure 6.1(c)** respectively. Those substrates are both considered highly inert [158] to support two-dimensional Group V structures. SiCH - (0001) is modelled by four layers of SiC (0001) with both the top and bottom layer passivated by hydrogen atoms. For h-BN, we have compared the effect of bismuthene on a single layer of h-BN and three layers of h-BN and found they give qualitatively similar results. Hence in the following calculations, we

use a monolayer of h-BN as a simplified model to represent the bulk h-BN substrate. For the stacking between bismuthene and h-BN, we further consider sandwich stackings of h-BN/bismuthene/h-BN sandwich. The stacking order of two h-BN layers can be either AA and AB (**Figure 6.1(d)**and **6.1(e)**). AA stacking is related to AB stacking by a rotation of 60 degrees around the vertical axes.

Lattice mismatch is an important factor when we consider the modelling of heterostructures. The relaxed lattice parameter for the freestanding bismuthene unit cell is 5.27Å. The 2×2 h-BN substrate lattice is 5.02 Å (4.7% lattice mismatch). The SiCH-(0001) substrate lattice is $\sqrt{3} \times \sqrt{3}$ 5.34 Å (1.3% lattice mismatch). For the bismuthene/substrate models, we fixed the bismuthene lattice constant to that of the substrates. Both lattice mismatches are less than 5%. For both substrates, bismuthene maintains planar after the relaxation of the structures, indicating that the planar form of two-dimensional bismuth layers can be stabilized. This agrees with previous theoretical results suggesting planar bismuth should be energetically favourable than a buckled layer if the lattice constant of two-dimensional bismuth is stretched above 5.3 Å.[90] The experimental fabrication of the planar bismuthene on SiC(0001) in [70] also suggested that it is possible for the planar bismuthene to survive the lattice mismatch.

6.3 Freestanding Bismuthene

6.3.1 Orbital Analysis for Freestanding Bismuthene

We firstly revisit the electronic structure of freestanding planar bismuthene. Bismuthene has been confirmed to be a Z_2 topological insulator when placed on silicon carbide substrate both

theoretically [100] and experimentally [70]. In its freestanding form, bismuthene was predicted as a topological crystalline insulator with edge states protected by mirror symmetry [77]. We have calculated the electronic band structure of bismuthene and bismuthene nanoribbons as shown in **Figure 6.2**. The bulk (**Figure 6.2(a)**) , ZZ(**Figure 6.2(b)**)**,** and AC(**Figure 6.2(c)**) edge band structures are consistent with previously published DFT [77] and TB [72] results. In the band structure of nanoribbons, we can clearly see edge states continuously connecting the top of the valence band and the bottom of the conduction band. We have verified that bismuthene has a mirror Chern number of 2 via Wannier tight-binding methods, confirming that freestanding bismuthene is a topological crystalline insulator.

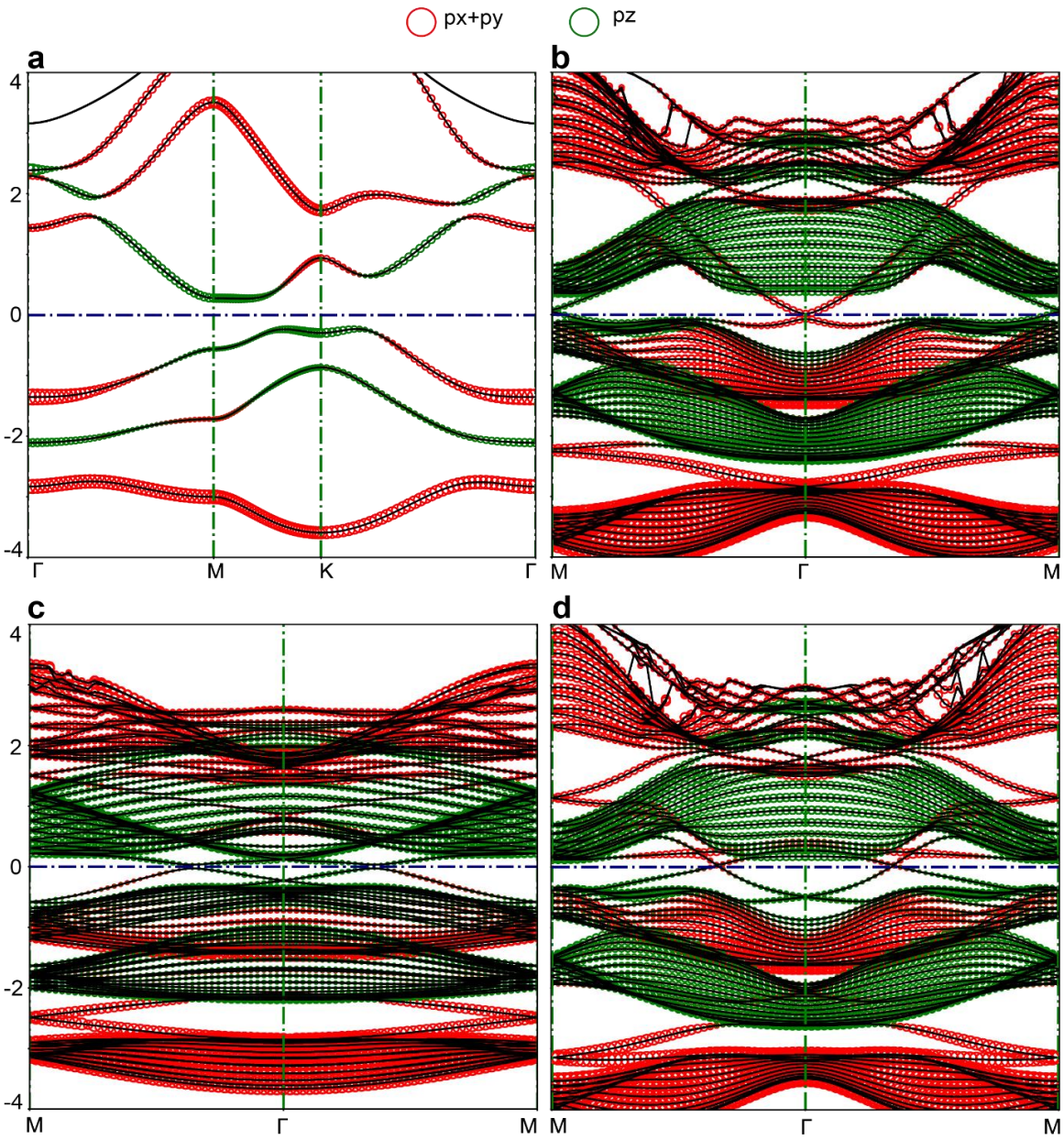

Figure 6.2 | DFT Orbital analysis for freestanding bismuthene at (a) bulk bismuthene, (b) ZZ, (c) AC, and (d) ZZ-k edge configurations.

We also calculate the orbital characters of bands as shown in coloured circles in **Figure 6.2** Orbital characters will be useful later to demonstrate the change in electronic and topological properties due to substrate effects. For freestanding bismuthene, we can observe the features

of band inversion at TRIM point K, between px+py (red) and pz (green) orbitals. As a result of band inversion, edge states in bismuthene nanoribbons form inside the gap region connecting the valence band with the conduction band. We have also found that different edge terminations lead to different edge band degeneracy features and orbital characters. Zigzag nanoribbons **(Figure 6.2(b))** show edge band degeneracy point at Γ contributed by px+py orbitals, while the degeneracy at M is dominated by pz orbital. However, for armchair **(Figure 6.2(c))** and ZZ-k **(Figure 6.2(d))** edge terminations, the edge band crossings are located at generic kpoints, with combined px+py and pz orbital characters.

6.3.2 Wannier Edge States for Freestanding Bismuthene

Using DFT and Wannier functions, we have constructed the edge states plot for freestanding bismuthene on the four different edges. (See **Figure 6.3(a)(b)(c)(d)**). Consistent with our result on nanoribbon calculation and previous literature. All edges hold continuous edge states from the valence band to the conduction band. When compared the DFT edge states (**Figure 6.2 (b)(c)(d))** with the Wannier edge states (**Figure 6.3 (a)(b)(c))**, we can find that the edge states from the two methods are qualitatively very similar near the Fermi level, but has some variation in detail. The detailed variation includes the risen band at Γ point in ZZ structure, and the different numbers of distortions at the higher energy region near the conduction band minimum. Despite the slight distortions, the tight-binding model can demonstrate well the band shape of the edge states. The AC band structure for both models fit well with each other.

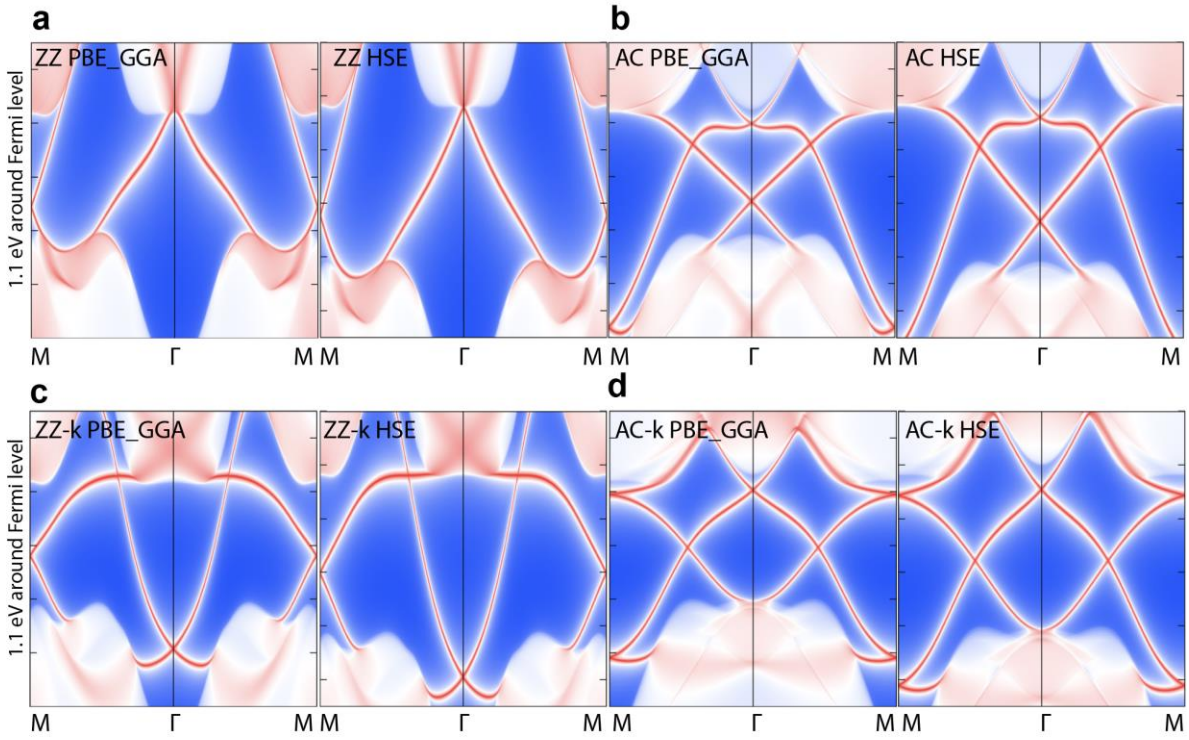

Figure 6.3 Freestanding bismuthene edge states for (**a)** ZZ, (**b)** AC, (**c)** ZZ-k and (**d)** AC-k edge states. Both GGA-PBE and HSE are plotted.

6.4 Bismuthene on substrate

6.4.1 Substrate Type that Maintains the Edge States

We first examine the effect of SiC, a popular choice as the supporting substrate for bismuthene. Previous reports have shown that bismuthene can bind covalently on SOC. However, the formation of covalent bonds between bismuthene and the substrate turns the bismuthene into a Z_2 topological insulator [70]. Therefore, to preserve the topological nature of bismuthene as a TCI when placed on a substrate, we have passivated both surfaces of SiC with hydrogen atoms to form an inert substrate denoted as SiC-H (0001). The interaction between SiC-H (0001) is

now mainly governed by weak van der Waals forces. Hence the electronic structure of bismuthene would be expected to be less affected by substrates compared to the covalent-bonded system.

We can confirm the interaction strength by assessing the energy feasibility of the system via calculating the cohesive energy of the bimsuthene-substrate system. The cohesive energy is defined as: $\mathrm{E_{cohesive}} = E_{sub} + N \times E_{Bi} - E_{tot}$, where E_{tot} is the energy of the bismuthene-substrate system, E_{sub} is the energy of the relaxed isolated substrate, N is the number of bismuth atoms in the bismuthene cell and E_{Bi} is the energy of a single bismuth atom. A positive $E_{cohesive}$value means that formation of the structure is energetically favourable. The cohesive energy of bismuthene-SiCH-(0001) is 2.01 eV/atom, which is much lower compared to 4.00 eV/atom on covalently-bonded planar bismuthene SiC-(0001) substrate, indicating that bismthene does not form strong chemical bonds with the underlying SiCH-(0001) susbstrate.

We calculate the edge band structure of bismuthene nanoribbons on SiC(0001)-H using Wannier-based tight-binding models as shown in **Figure 6.4 (a)(b)(c)(d).** Similar to the freestanding bismuthene, we can observe two branches of edge bands around the Fermi level. Upon support on SiCH-(0001), we see a strong edge-dependent response of edge states affected by the substrate. For AC and AC-k edges, the edge band generalise along $\overline{\Gamma} - \overline{M}$ are broken (highlighted by circles in **Figure 6.4 (b)(d)**). Since the band degeneracy along $\overline{\Gamma} - \overline{X}$ is protected by mirror symmetry, suggesting the substrate effect has switched off the TCI phase in bismuthene. However, the edge band degeneracies for ZZ (**Figure 6.4(a)**) and ZZ-k (**Figure 6.4(c)**) edges are not broken. For the ZZ edge, this is mainly due to the fact that band

degeneracies are located at TRIMs, thus stabilized by the presence of time-reversal symmetry. For ZZ-k edge, the mirror symmetry-protected degeneracies along $\overline{\Gamma} - \overline{M}$ are not broken in contrast to the response in AC edge nanoribbons. This indicates that the band topology of TCI under the influence of the substrate is dependent on the edge configuration.

Next, we investigate the interaction of bismuthene with another planar two-dimensional material, h-BN**.** The cohesive energy of bismuthene on h-BN is 1.86 eV/atom, slightly less than SiCH-(0001). The edge band structure of bismutene nanoribbons on h-BN is shown in **Figure 6.4 (e)(f)(g)(h).** We find that the edge band dispersion is nearly unaffected for all edge configurations compared to freestanding bismuthene. The edge states are still gapless, suggesting that TCI states are still protected. Therefore, we can conclude that if the interaction between the bismuthene and the substrate is weak enough, the TCI states of bismuthene can still be maintained and stabilized.

We have noticed that some reports have shown that h-BN can lead to broken edge band degeneracies in bismuthene [77]. This can be explained by the narrow width (~3 nm) used in their calculations. Band gap opening can happen in a nanoribbon structure contributed by quantum tunnelling coupling between different edges, and this effect becomes more evident as the width of the nanoribbon decreases [159].

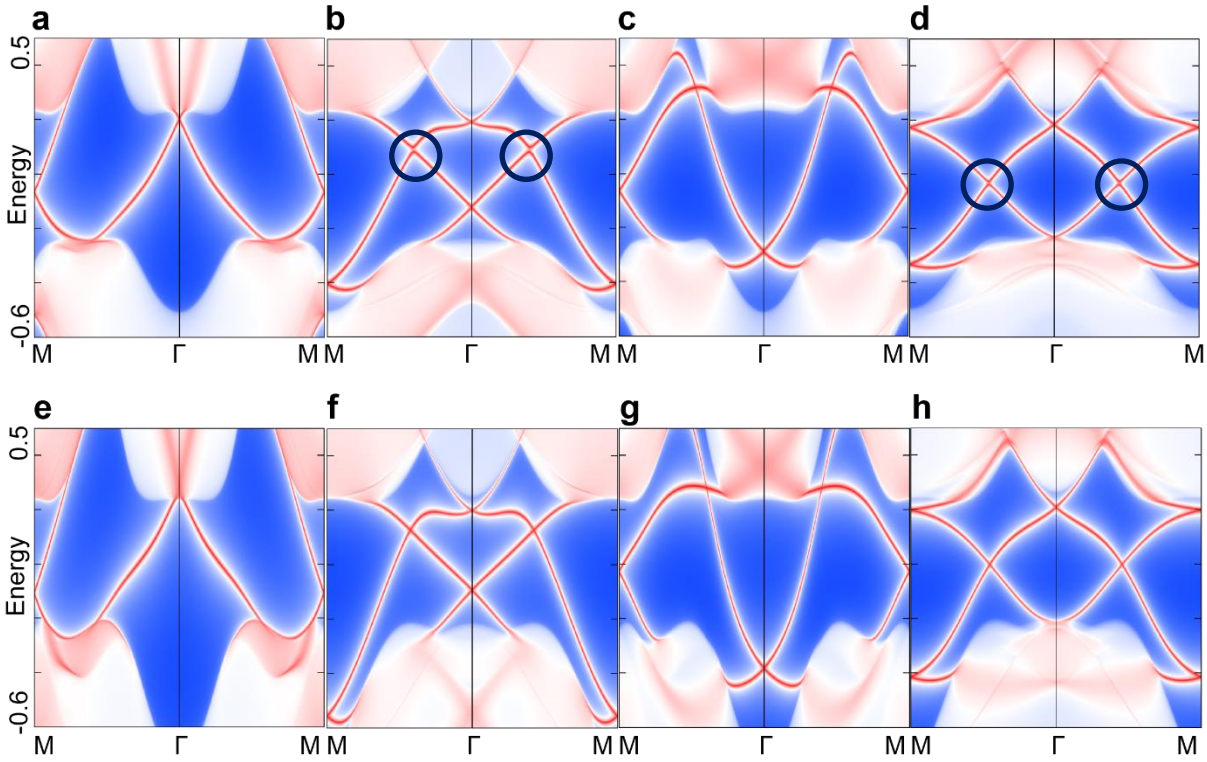

Figure 6.4 Wannier edge band structures for bismuthene/ SiCH-(0001) with **(a)** ZZ **(b)** AC **(c)** ZZ-k edge configuration and **(d)** AC-k edge and bismuthene/ h-BN structures with (**e)** ZZ, **(f)** AC, **(g)** ZZ-k, **(h)** AC-k edge configuration. Black circles denote the breaking points.

We have done a similar DFT analysis using nanoribbon of sub 3nm width. We find edge band degeneracies are broken even for a freestanding bismuthene. These results can in turn indicate that the edge states can be fragile against size effects but should be robust against weak substrate perturbations.

6.4.2 Substrate Configurations that Maintain the Edge States

We have shown that the weak van der Waals interaction imposed by weak substrates such as h-BN can preserve the TCI states of planar bismuthene. However, we can see that the one-side stacking approach is not a convenient way to protect the TCI phase of planar bismuthene as the

in-plane mirror symmetry can be easily broken if the perturbation from the substrate is strong enough. Although we have shown that one-side supporting h-BN can stabilize the TCI edge states, it would still require a delicate control of substrate-bismuthene interaction when using in practice. The detailed study about the substrate-induced band gap opening can be found in **Chapter 7**. Alternatively, we can take the advantage of using this van der Waals system by efficient and flexible controlling of interfacial contact. We can further modify the electronic response of planar bismuthene by varying interfacial conditions such as tuning the stacking order or placing additional supporting layers.

Therefore, we propose a stacking scenario by placing the bismuthene in between two h-BN layers, forming a sandwich stacking structure. This sandwich stacking configuration of h-BN layers is designed not to disrupt the mirror symmetry of bismuthene, thereby the edge states of bismuthene can survive the interactions with substrates. The edge states in sandwich stacking are plotted on **Figure 7.3(i)(j)(k)(l)** to compare with the edge configurations where the band gap is opened. We can see that the degeneracy points in the edge band structure are preserved under the sandwich stacking. These results have shown that it is possible to protect the edge states of TCI on a substrate via appropriate stacking of the substrates.

6.5 TI-like Zigzag Edge Termination

6.5.1 Uniqueness of Zigzag Edge Configuration

Now we have shown the TCI phase of bismuthene can be conveniently switched on/off on substrate by tuning stacking configurations and the interfacial distance. During the

investigation, we have also observed that the electronic structure of bismuthene nanoribbons can be affected by the configuration of edge terminations. The interplay between the substrate potential and the edge structure can lead to different electronic responses in the edge states (see **Figure 6.4(a)-(d)**). For ZZ-k, AC, and AC-k nanoribbons, the edge state degeneracies only break at k-points on the high symmetry line when the mirror symmetry is disrupted by the substrate, while the degeneracies at high symmetry points are retained. However, for ZZ nanoribbon, the edge state degeneracies only occur in the high symmetry point Γ and M, therefore we do not see any edge states broken even when strong pressure/rotation effects are applied. These results can be explained by that degeneracy at TRIMs (Γ and M) are protected by time-reversal symmetry, while the degeneracy at other kpoints is not. Since ZZ nanoribbons only have edge states connecting at TRIMs near the Fermi level, the edge states can then survive strong substrate effects that do not break time- reversal symmetry.

The robustness of the edge states exhibited by the bismuthene zigzag nanoribbon could also be explained by the separation of p orbital characters in the edge bands. Previous studies have suggested that the electronic bands of planar bismuthene near the Fermi level are composed of two branches of topologically nontrivial bands with px+py and pz character, respectively. However, the combination of these bands leads to a Z_2 trivial band topology. If we apply these conclusions and analyze the band character of edge bands, we find that zigzag nanoribbon has completely separated the px+py and pz bands unlike armchair terminations. As shown in **Figure 6.2(b),** the orbital character near Γ is dominated by px+py, while the pz orbital is concentrated near M for ZZ nanoribbons. The px+py and pz edge band branches are completely separated. While for AC and ZZ-k terminations, the px+py and pz orbitals are all mixed on the

edge bands (**Figure 6.2(c) and 6.2(d)**). Therefore, if the mirror symmetry of the nanoribbon is broken by substrates or external factors, the edge degeneracies at non-TRIM positions (Γ or M) with all p orbitals mixed will not be protected for AC and ZZ-k nanoribbons. The edge degeneracies in ZZ nanoribbon only occur at TRIMs and they should be robust against mirror symmetry perturbations which cannot be broken as long as the time-reversal symmetry is conserved.

The two separated branches at Γ and M in the zigzag nanoribbon can be bridged if we can induce structural defects such as forming the Klein defects at edges, i.e. ZZ-k edge terminations. The edge bands in ZZ-k nanoribbons still consist of two separated band approaches centring at Γ and M. However, with the change of edge band energy alignment, the two branches now have an additional degeneracy along $\Gamma - M$, The p orbital characters become mixed near this band degeneracy, as in the case of AC and AC-k nanoribbons. When the mirror symmetry is lifted, the edge degeneracies are broken and a band gap appears. The results above have indicated that the stability of edge states in TCI does not only depend on whether the mirror symmetry of the lattice is broken, but also be affected by the position of the edge band degeneracies and the band orbital characters. We can utilize this effect in practice either to maintain, or selectively tune the edge current with different edge terminations.

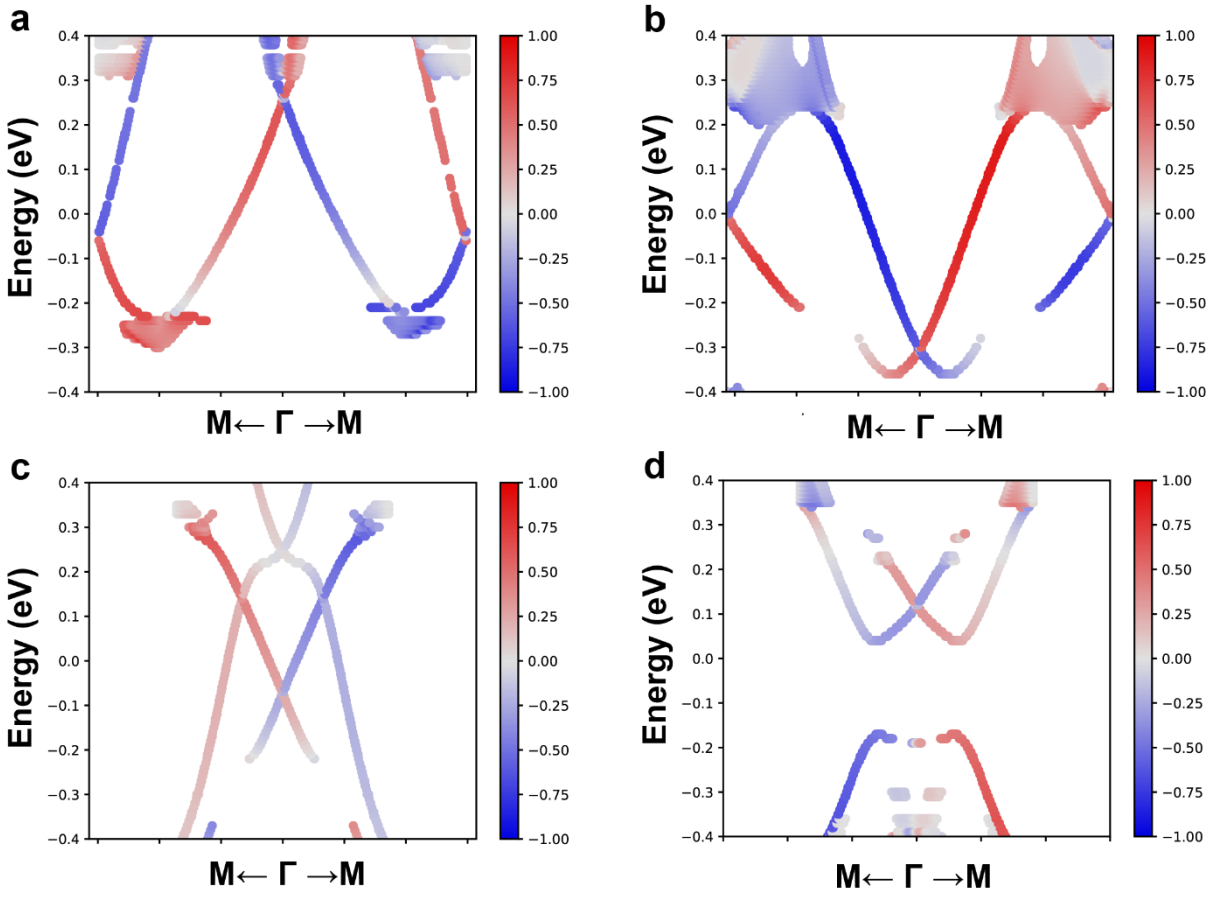

Figure 6.5 Spin texture along Sz direction for edge states in (**a)** freestanding bismuthene ZZ edge band structure**,** and **(b)** Bi/h-BN ROT at 2.76 Å ZZ structure **(c)** freestanding bismuthene AC edge band structure **(d)** Bi/h-BN ROT at 2.76 Å AC band structure. Red colour indicates spin up, while blue colour indicates spin down.

6.5.2 Spin Texture Analysis

TCI has spin filtered edge states protected by the mirror symmetry. We can see this behaviour in the edge spin texture of freestanding bismuthene (see **Figure 6.5 (a)(c)**). The spin polarizations around TRIM degeneracies always have opposite signs like topological insulators, while the spin polarization around non-TRIM degeneracies has the same sign. These non-TRIM edge degeneracies are exclusively protected by mirror symmetry and are known as spin-

filtered states. The TRIM edge degeneracies are also protected by TR symmetry. If we apply an external pressure to break the mirror symmetry, we can find that the spin texture around TRIMs is maintained. The non-TRIM edge degeneracies become gapped, but the spin polarizations around the broken point are retained (see **Figure 6.5 (b)(d)**). We can conclude that the spin filtered feature of the edge degeneracy of bismuthene is not affected by the mirror symmetry-breaking potential.

6.6 Conclusions

While 2D TCI is generally considered vulnerable against the environment, we have found several effective approaches to maintain the edge states. Using a graphene-like bismuthene honeycomb as a 2D TCI model, we have demonstrated that the edge states can be tuned in the following manner. Although it is well understood that mirror symmetry breaking substrate would create band gap, choosing a weaker substrate would be helpful to maintain the edge state. Therefore, weaker substrates are recommended for the synthesize of 2D TCIs. Another approach to maintain the edge states is to maintain a certain edge with an edge band structure that does not have band crossing at generic k-point. We have verified that when the zigzag edge is maintained, both changing interfacial distance and substrate effect leads to the change in a band shape, but does not lead to the opening of a bandgap. This can be an effective approach to tune the edge electron transport while maintaining conduction. We have verified that those edge states are spin filtered edge states similar to topological insulators, which makes the material an excellent candidate as a spin current injector in spintronic devices. We have also demonstrated that when the bismuthene is in a substrate/2D material/substrate structure, all

edge states can survive despite changing interfacial distance. Such stacking is recommended in future electronics design if stable TCI edge states are desired.

Chapter 7 Tuning the Edge State of Bismuthene on Substrates

7.1 Introduction

Specifically for usages in electronic transistors, it is ideal that the conduction current can be conveniently switchable [56]. Recently it has been experimentally realised that the topological states of topological Dirac semimetal Na_3Bi can be turned on and off through an external electrical field. The electric field changes the band ordering in the Na_3Bi thin film, and eliminates the original topological band inversion, thus turning the topological nontrivial phase into a conventional insulator [60]. However, for many topological systems, the level of the bulk band tuning upon application of electric field is relatively small. This has been the case for the topological materials such as bismuth, the electrical field does not have a strong impact on its bulk band structure in terms of band gap tuning [89]. Moreover, the bulk band re-ordering approach becomes much more difficult to implement for materials with a large band gap, which are desired candidates for room-temperature applications.

We then turn to our interests in another approach: directly tuning the edge states of two-dimensional topological materials via symmetry breaking. We choose topological crystalline insulators (TCIs) [160] to investigate since the edge states of TCIs are protected by crystalline symmetries. With certain edges, the TCI states are assumed to be turned off if crystalline symmetries are broken. Therefore, the high on/off operation speed should be expected, which

makes TCI a viable choice for making semiconducting electronic devices [75]. Despite this advantage, making electronic devices based on 2D TCIs is still challenging in experiments since the conducting edge states ("on" state) is hard to be stabilized when interacting with underlying substrates [152].

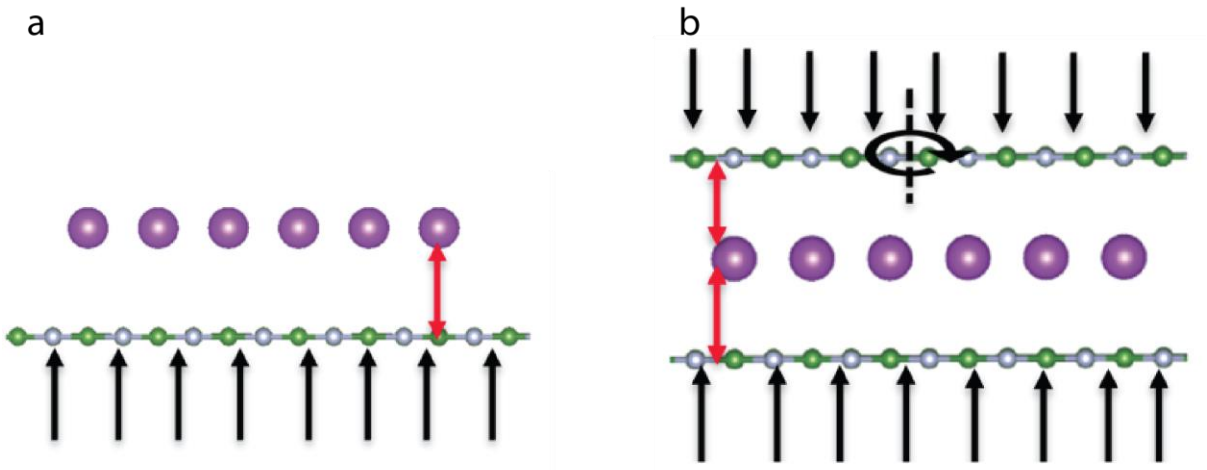

Figure 7.1 Illustrations showing the Bi/h-BN under pressure with **(a)** single-sided stacking and **(b)** rotated sandwich stacking.

We found that these states can be tuned on/off by applying external factors such as pressure, electric fields, and controlling substrate stacking. The illustrations demonstrating how the pressure applied for single-sided stack and rotated sandwich structure stacking is shown in **Figure 7.1(a)** and **Figure 7.1(b)** respectively. The mirror-symmetry breaking effect can be demonstrated with our effective Hamiltonian model. These results provided guidelines for tuning the edge states of topological materials.

7.2 Tuning the Armchair Edge Band Gap

7.2.1 Interfacial Distance Control

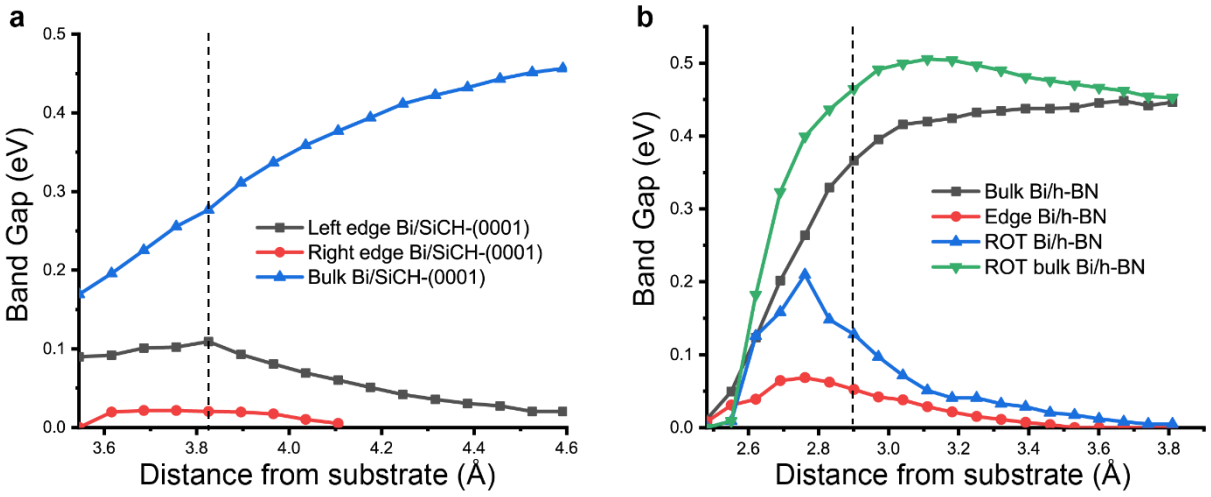

Figure 7.2 Bulk band gap and edge gap in AC structure for **(a)** Bi/SiCH-(0001) and **(b)** Bi on h-BN Substrates. The dashed line corresponds with the distance used in **Figure 7.3**. Bulk bandgaps are calculated through DFT, while the edge band gap is calculated through Wannier functions projected on Bi p-orbitals.

We can also modify the interfacial contract between bismuthene and substrates by reducing the interfacial distance from the substrate. We calculate the evolution of the armchair edge band gap in bismuthene nanoribbons supported on substrates as a function of the interfacial distance in **Figure 7.2**. We have also calculated the band gap between the highest valence band and the lowest conduction band for 2D bismuthene on substrates. In the case of SiCH-(0001) **(Figure 7.2(a)),** when the interfacial distance is reduced from the relaxed distance of 4.8 Å, the band gap in the 2D band structure of bismuthene gradually decreases. In the corresponding edge

band structure for the armchair bismuthenne nanoribbons on SiCH-(0001), we can see that the edge gap is opened and becomes larger as the interfacial distance decreases. We demonstrate the edge band dispersion of pressed bismuthene on SiCH-(0001) (interfacial distance at 3.8 Å) in **Figure 7.3(a)(b)(c)(d)**. The edge band degeneracies are broken at non-TRIM points along $\overline{\Gamma} - \overline{M}$ for AC, AC-k and ZZ-k edge configurations. These observations imply that reduced interfacial distance induces strong mirror symmetry-breaking potential.

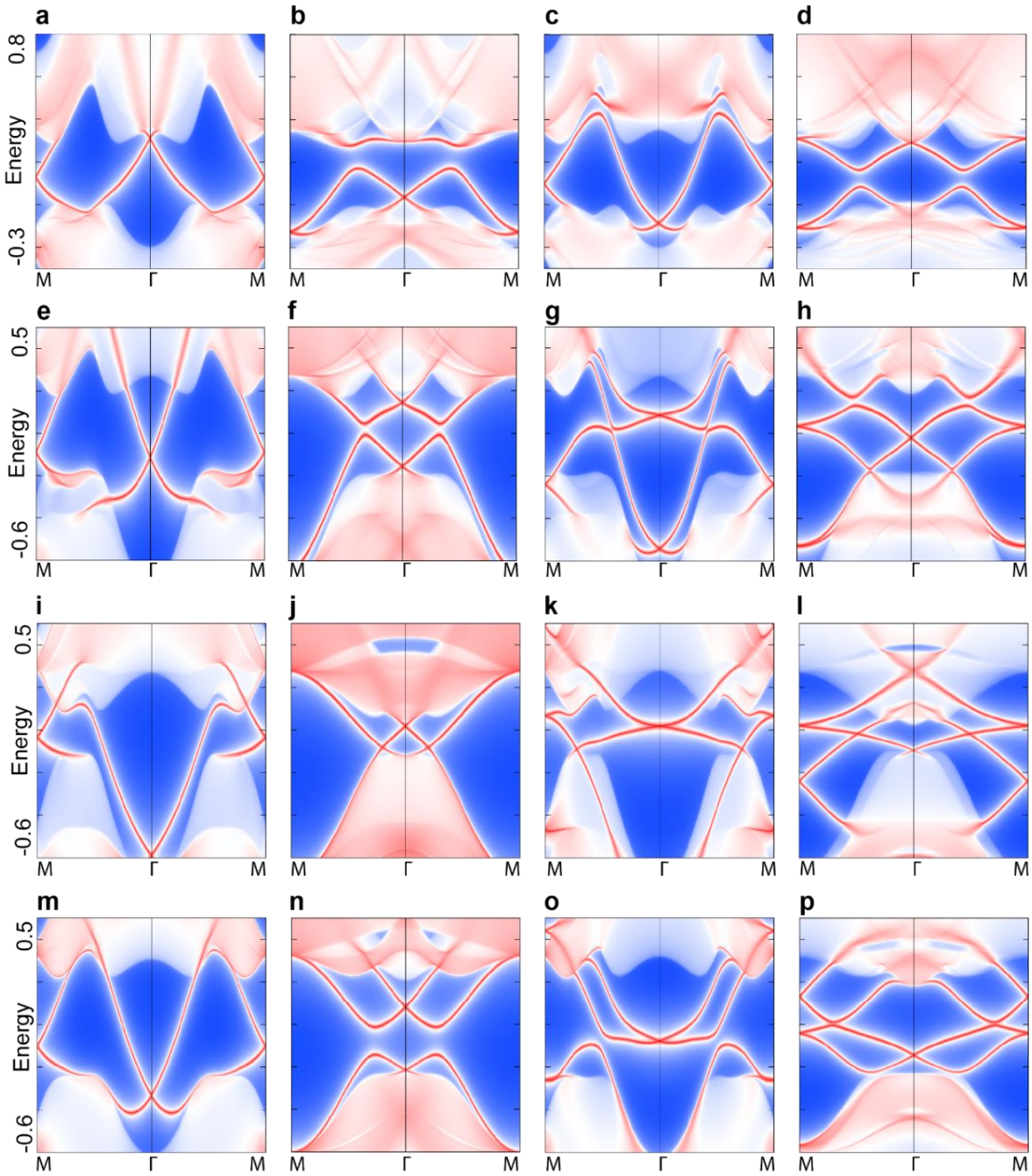

Figure 7.3 (a)(b)(c)(d) Bi/SiCH-(0001) at 3.8 Å ZZ, AC, ZZ-k and AC-k edge band structures. **(e)(f)(g)(h)** Bi/h-BN at 2.9 Å ZZ, AC, ZZ-k and AC-k edge band structures. **(i)(j)(k)(l)** Bi/h-BN SAN at 2.9 Å ZZ, AC, ZZ-k and AC-k edge band structures. **(m)(n)(o)(p)** Bi/h-BN ROT at 2.9 Å ZZ , AC, ZZ-k and AC-k edge band structures.

We can see a similar trend if we change the supporting substrate to h-BN, as shown in **Figure 7.2(b)**. We have shown that the TCI phase of bismuthene is preserved at a relaxed distance. When the interfacial distance (3.8 Å) is reduced, the influence of the substrate on the electronic structure of bismuthene becomes more significant and breaks the edge degeneracies protected by the mirror symmetry for armchair structure. This can be reflected in the armchair edge band structure of bismuthene on h-BN with an interfacial distance of 2.9 Å as shown in **Figure 7.3(e)(f)(g)(h)**. When we further decrease the distance between bismuthene and h-BN to below 2.55 Å, we find that the edge band gap reaches a maximum of 210 meV and then begins to decrease again, approaching nearly zero at 2.34 Å. This fluctuation trend of an edge band gap in bismuthene on h-BN is a result of the competing mechanism between the mirror-breaking potential from the band gap opening the 2D. The band gap closure is a consequence of the reduced interfacial distance (**see Figure 7.4**).

In summary, we can see that tuning the interfacial distance between bismuthene and the substrate is effective in switching the topological structure of bismuthene. In experiments, this can be achieved by applying external pressure on the system to enforce closer interfacial contact. We can estimate the relation between the interfacial distance d and the interfacial pressure P can be estimated as $\mathrm{P} = \frac{\partial \mathrm{E}}{\partial \mathrm{d}}/\mathrm{A}$ for our calculations, where E is the energy of the bismuthene-substrate system for a unit-cell, with surface area A. We have plotted the evolution of band gaps as a function of the estimated interfacial pressure in **Figure 7.5**. For different substrates, the strength of interfacial pressure can be drastically different (around 7 GPa for SiCH-(0001), 30 GPa for h-BN) to achieve a similar maximum edge band gap.

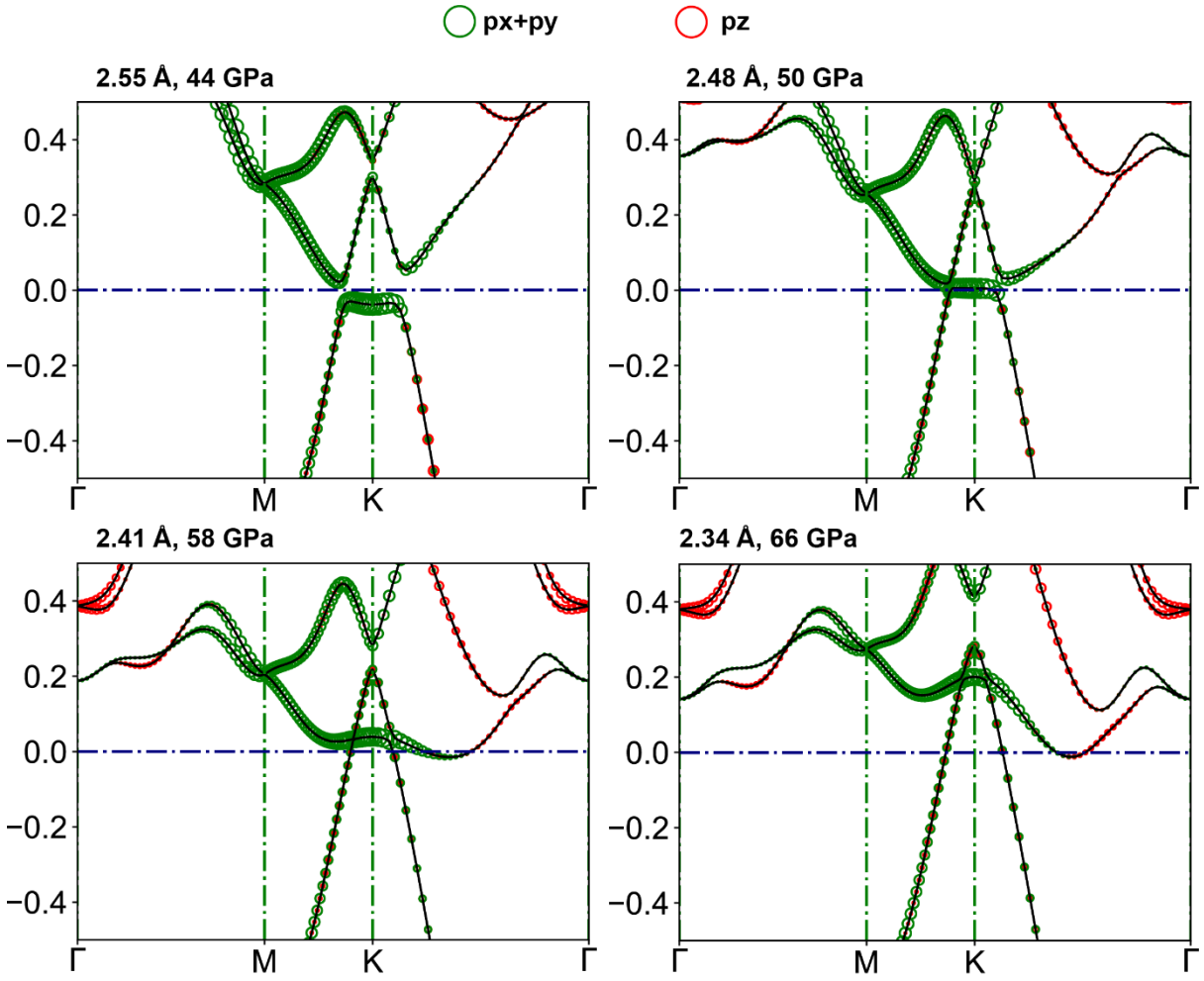

Figure 7.4 Orbital projected band structure near the Fermi level for single sided Bi on h-BN at the interfacial distance 2.55Å to 2.34 Å (pressure increased from 44Gpa to 66GPa).

7.2.2 Substrate Configuration Control

The sandwich configuration could potentially shield the TCI phase of bismuthene from external modification. We have tested the sandwich configuration of h-BN/bismuthene/h-BN, with both

interfacial distances between h-BN compressed to 2.9 Å (1 Å from the relaxed distance). The edge band structure (**Figure 7.3(i)(j)(k)(l)**) shows that the edge band degeneracies are preserved, meaning that although applying external pressure can induce significant influences on bismuthene, the electronic and topological properties of bismuthene can still be preserved if it is placed in a symmetrical environment.

We can tune the electronic structure of sandwich configurations by changing the stacking configuration of the two h-BN substrates. Previously we have made the two h-BN substrates mirror-symmetric. We can change the stacking configuration of the two substrates to antisymmetric by rotating the top h-BN substrate by 60° (denoted as ROT configuration). The antisymmetric stacking configuration will break the edge band degeneracies in bismuthene nanoribbons and result in a large gap opening if applying an interfacial pressure (**Figure 7.2(b) and 7.3(n)**). **Figure 7.4** demonstrates the band closure process of band pressure as the interfacial distance is reduced from 2.55 Å to 2.34 Å. Finally, the valence band at K rises and

merges with the conduction band minima at about 2.41 Å (58 GPa). This demonstrates the band closure and the end of this adiabatic band transformation process.

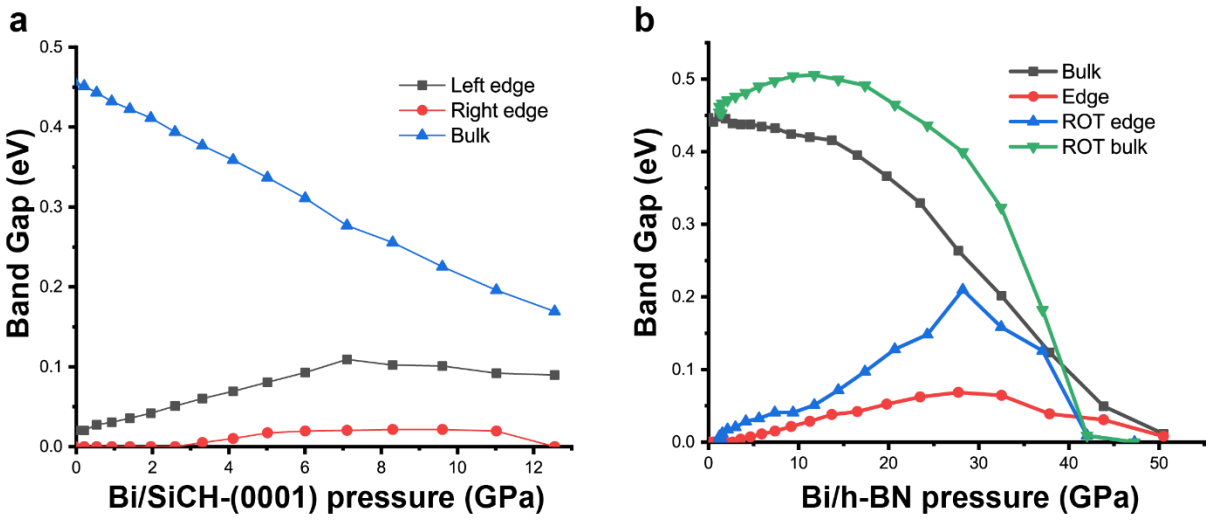

Figure 7.5 Band gap evolution near the Fermi level against pressure (GPa) between thin film and substrates for **a** Bi/SiCH-(0001), **b** Bi/h-BN configurations.

7.3 Effective Tight-Binding Hamiltonian Model of Bismuthene on Substrates

To better understand the physical origin of the effect of weak perturbations on the electronic structure of bismuthene nanoribbons, we have built a second-nearest neighbour tight-binding model for freestanding bismuthene nanoribbon based on Wannier projection from DFT calculations [161]. The tight-binding Hamiltonian can be expressed as $H = t\sum_{\langle ij\rangle} c_i^{\dagger} c_j + \lambda_{SO}\hat{\boldsymbol{L}} \cdot \hat{\mathbf{S}}$ where the first term is the neighboring hopping between bismuth atoms with hooping strength t and the second term is the intrinsic SOC of bismuth with a SOC strength of $\lambda_{SO.}$ We

have shown good agreement between our band structure from the TB model and DFT results (see **Figure 7.6**) for ZZ and AC nanoribbons. Following the examples in Ref. [37] to model the effect of a perpendicular electric field or substrate interaction, we have used the following Rashba [162] term to our Tight Binding Hamiltonian. $H_R = i\lambda_R \sum_{\langle ij \rangle} c_i^{\dagger} \left(\boldsymbol{s} \times \hat{\boldsymbol{d}}_{\boldsymbol{ij}} \right)_z c_j$. The results with increasing mirror symmetry breaking parameters for ZZ and AC edge are presented in **Figure 7.6**. The model is consistent with our results, showing that the substrate effect can be energised to any mirror symmetry-breaking factors.

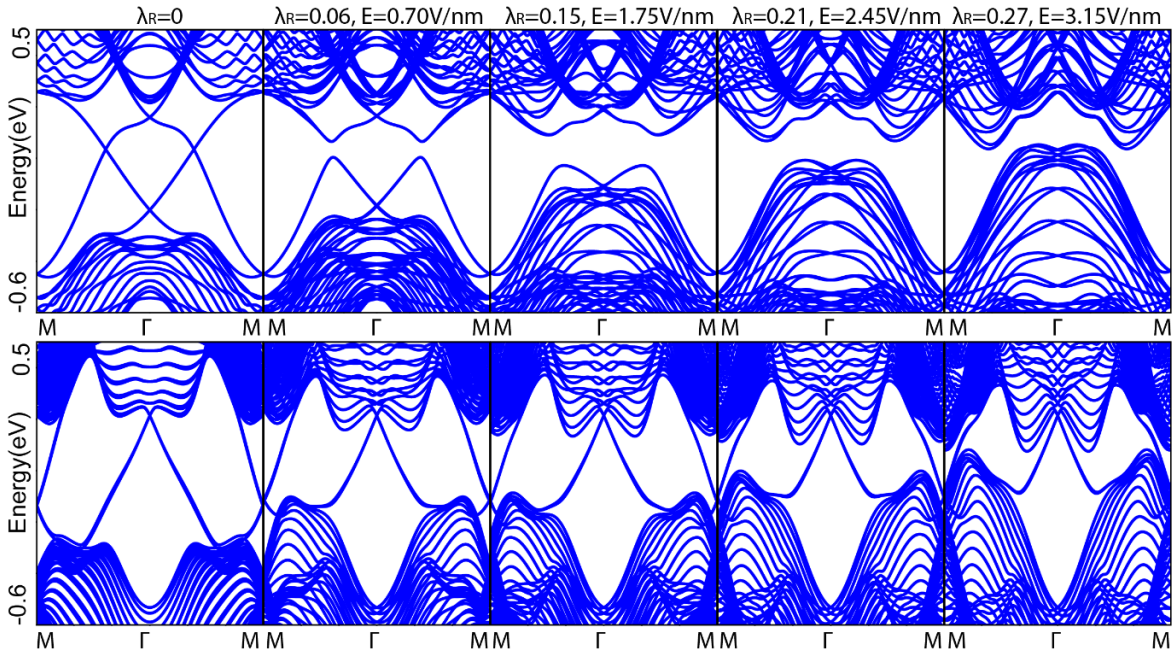

Figure 7.6 Evolution of band structure for AC (top) and ZZ (bottom) freestanding bismuthene nanoribbon when the Rashba parameter is increased from 0 to the level until the indirect band gap is closed. $\boldsymbol{\lambda_R}$ is in an arbitrary energy unit.

Using the model $\lambda_R = \frac{eEz_0}{3(sp\sigma)}\varepsilon$ describing electrical field interaction on Graphene taken from Ref. [163], the Slater-Koster matrix element $sp\sigma = 1.3$ for bismuth [164], and the spin-orbit

strength $\varepsilon = 1.158$ for planar bismuthene from our first-principles calculations, we can estimate the perpendicular electrical fields corresponding to the change of Rashba parameter. **Figure 7.7** shows the Armchair edge band gap evolution with increasing Electric field. The maximum edge bandgap, in this case, is about 118meV and is reached at about 1.75 V/nm. Considering the thermal energy 0.025eV at Room temperature, the "off" state can be reached at 0.35 V/nm, which is significantly lower than the electric field required for reaching "off" state through band ordering inversion approach [60]. A smaller electric field means improved power efficiency at high on/off speed. These results have shown that manipulating substrate effects in combination with other external factors such as pressure and field can be an effective approach to achieve realistic device switching on/off in semiconducting electronic devices.

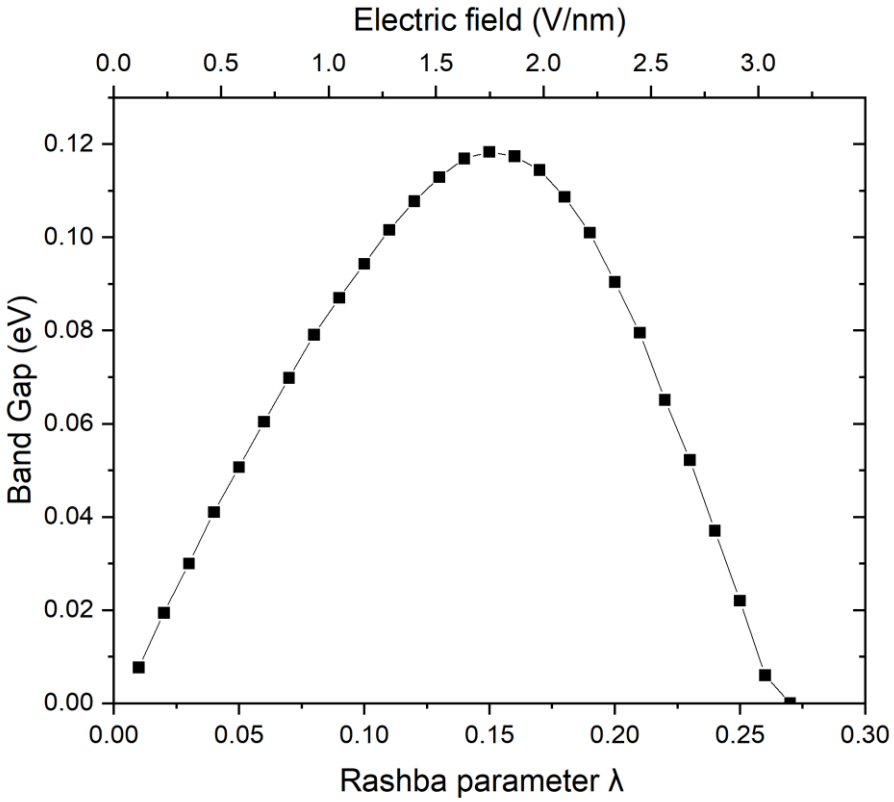

Figure 7.7 Band Gap evolution against Rashba parameter and corresponding electric field.

7.4 Wannier Charge Centre Analysis

We have confirmed the triviality of the bismuth-substrate system by calculating the Wannier charge centre (WCC) evolution. We can infer from the WCC plot in **Figure 7.8** that the Z_2 number of bismuthene on substrates is 0. For bismuthene/h-BN and bismuthene under sandwich substrates configuration, the WCC evolution graph shows two branches of WCC lines connecting along $k = 0$ to $k = \pi$, consistent with the mirror Chern number of 2. The connections along the $[0, \pi]$ corresponds to the location of the mirror-symmetry protected degeneracies. For other scenarios involving mirror symmetry-breaking perturbation such as bismuthene/SiCH-0001, and bismuthene under pressure, we observe a disconnection of WCC lines on $[0, \pi]$, indicating that the TCI phase is broken [142]. These results have proven that both weak substrates and sandwich substrate structures can be used as a good platform to achieve protected edge states in TCIs, and tuning interfacial contact can effectively switch on/off the TCI phase for its applications in transistor devices.

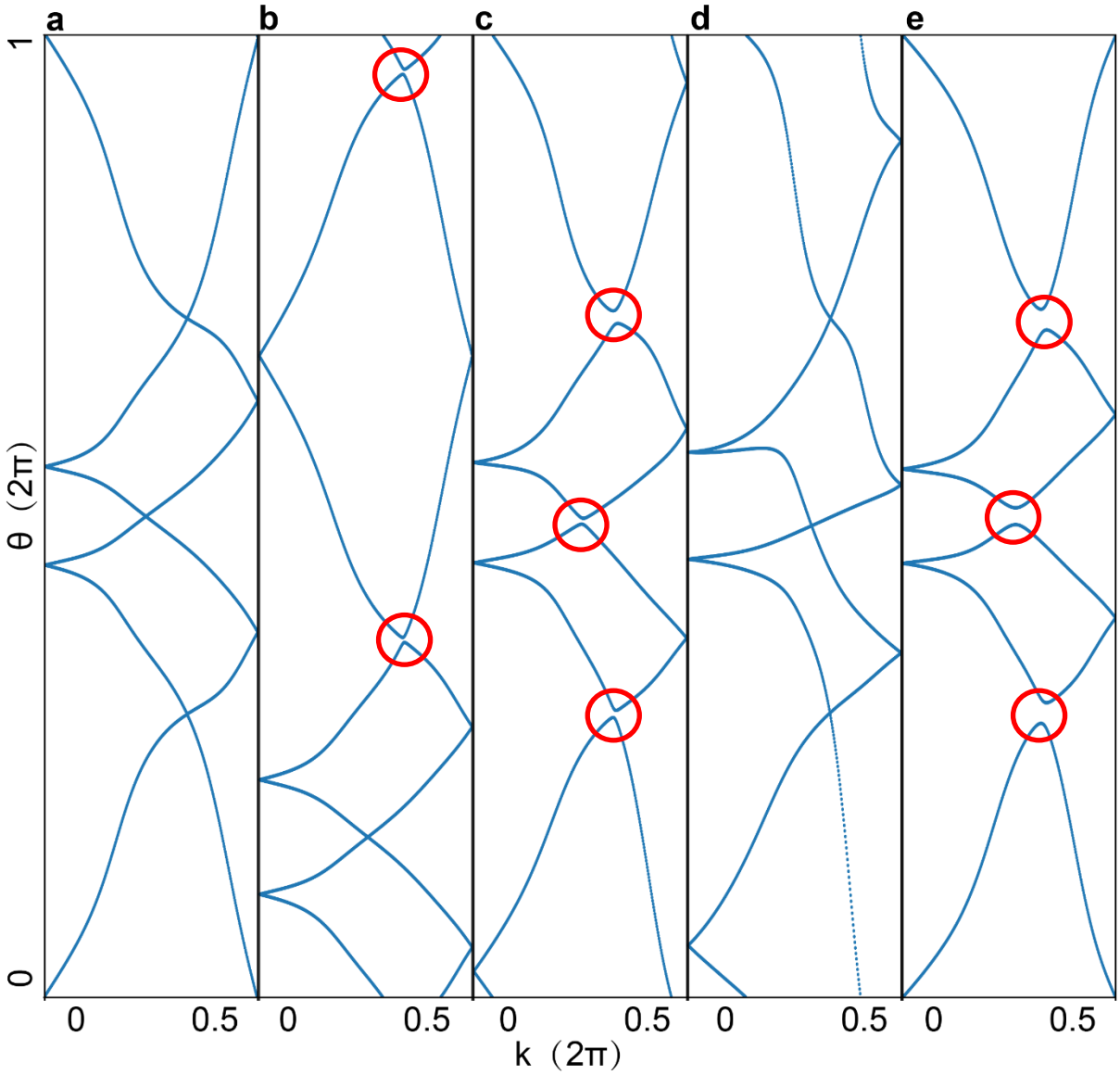

Figure 7.8 Wannier Charge Centre plot for **(a)** Bi/h-BN relaxed, **(b)** Bi/SiCH(0001) relaxed, **(c)** Bi/h-BN on one-side at 2.90 Å. **(d)** Bi/h-BN SAN 2.90 Å. **(e)** Bi/h-BN ROT 2.90 Å. The red circles mark the crossing point opened by mirror symmetry breaking perturbations.

7.5 Nanoribbon Width Studies

The 2D TI states are protected only when the nanoribbon is wide enough to reflect the bulk band structure. Using a slab model based on DFT Wannier tight-binding Hamiltonians, we have plotted the edge band structure against the number of slabs n. **Figure 7.9** demonstrates the nanoribbons in different configurations. The symmetry of the nanoribbon is also dependent on the number of slabs. For AC nanoribbons, an odd slab number n leads to the Pmma space group, while an even n leads to the Pmmm space group. This can be demonstrated via n = 17 (see **Figure 7.9(a)**) and n = 16 (see **Figure 7.9(b)**) examples. On the contrary, for ZZ nanoribbons, an even slab number n leads to the Pmma space group, while an odd n leads to the Pmmm space group. This is demonstrated in n = 8 (see **Figure 7.9(c)**) and n = 7 (see **Figure 7.9(d)**) examples. The difference is that Pmmm is symmorphic, while Pmma is non-symmorphic. The detailed symmetry analysis on graphene nanoribbon can be found in Ref. [165]. As shown in **Figure 7.10,** for AC bismuthene, the edge band gap is not closed until n is larger than 13 (corresponding width 3.2 nm). The band closure takes place at the generic kpoint between high symmetry points Γ and M. We can also observe the degeneracy opening at high symmetry points. which is prohibited when the nanoribbon is wide as we have analysed in **Chapter 6.5.1**. The breaking of degeneracy at M takes place at n= 3, 5, 7, 9 and 11, which clearly indicates that the degeneracy has an even/odd slab number dependency. The degeneracies at Γ point did not show an even/odd slab number dependency, but have shown a decreasing trend of energy gap from n=3 to n=12. As shown in **Figure 7.11** For ZZ bismuthene, the overall bandgap closes at n=11 (corresponding width 4.3 nm) when the edge states are bulk states are merged together. The degeneracy at M point closes at n=5. The degeneracy at Γ point

closes at about n=12, which does not affect the overall band closure since it sits between two other bands.

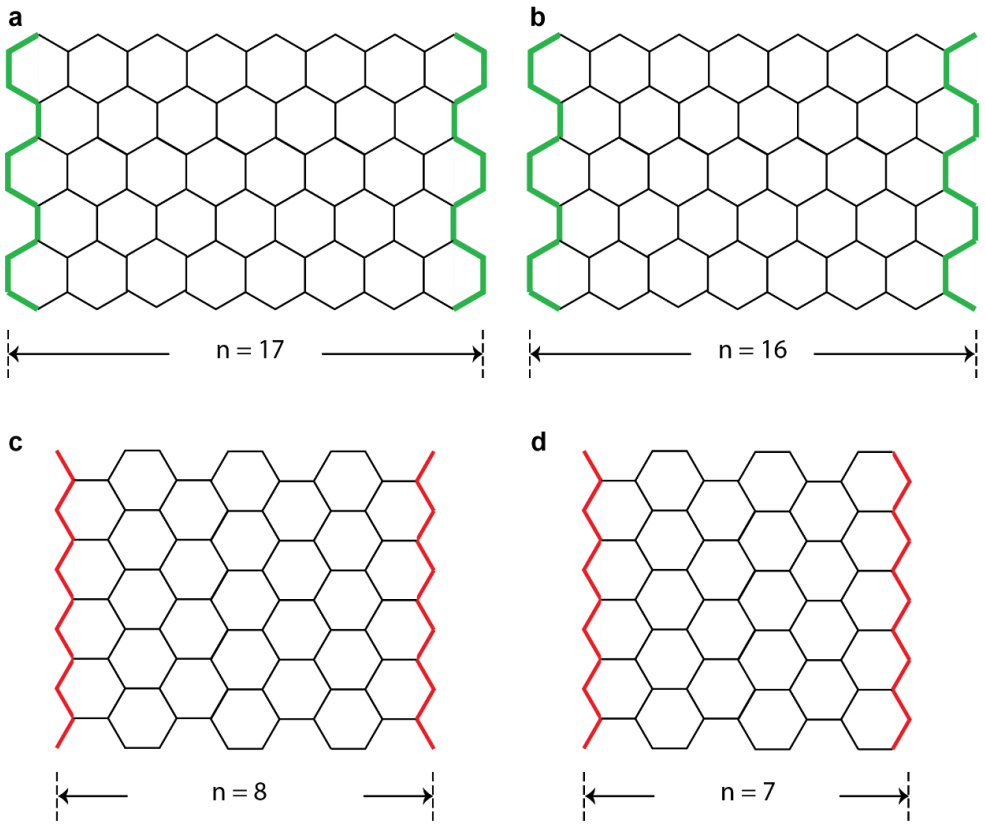

Figure 7.9 AC edge nanoribbon structure with the slab number **(a)** n = 17 **(b)** n =16, and nanoribbon for ZZ edge nanoribbon structure with the slab number **(c)** n = 8 **(d)** n = 7.

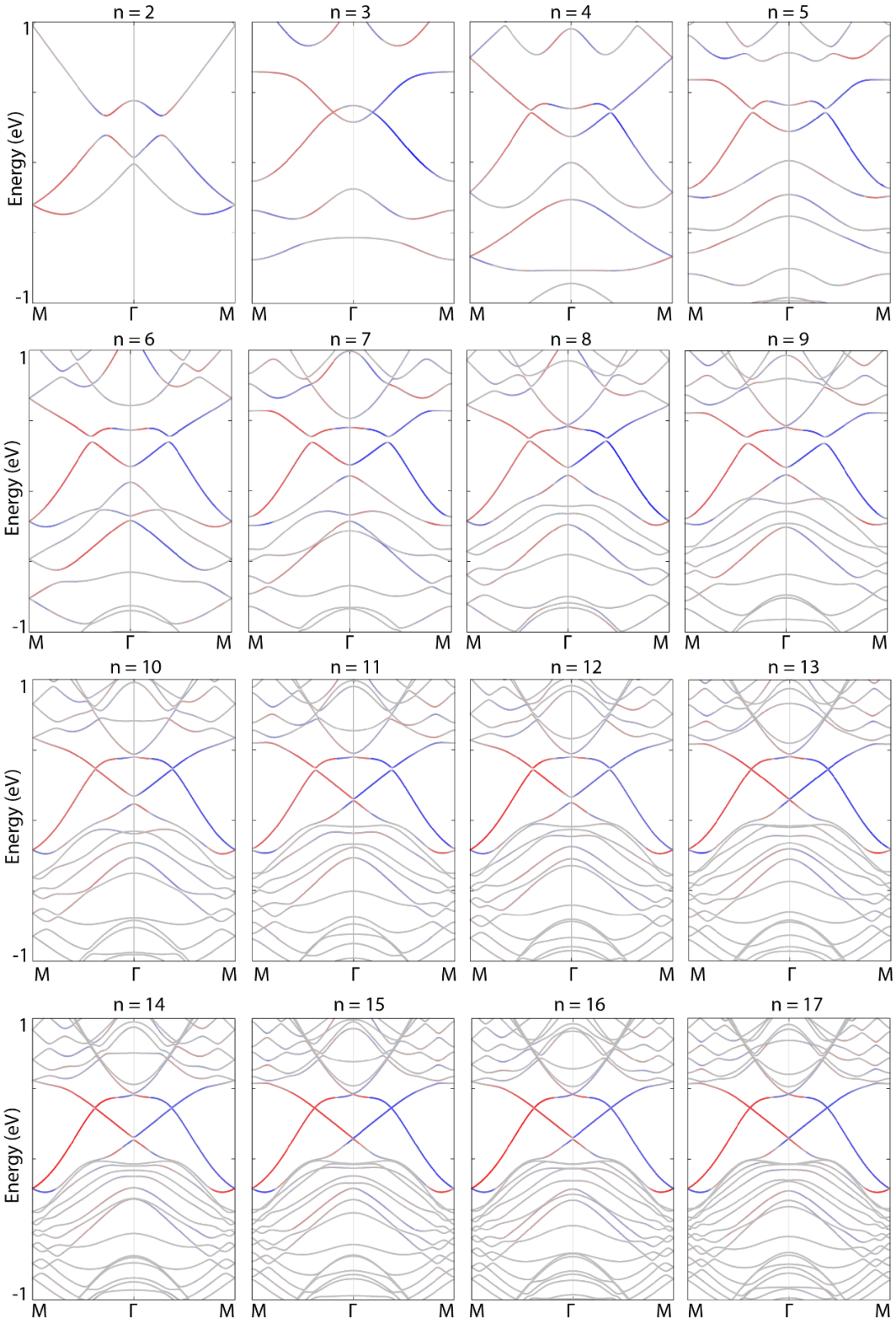

Figure 7.10 AC nanoribbon band structure as the slab number n grows from 2 to 17.

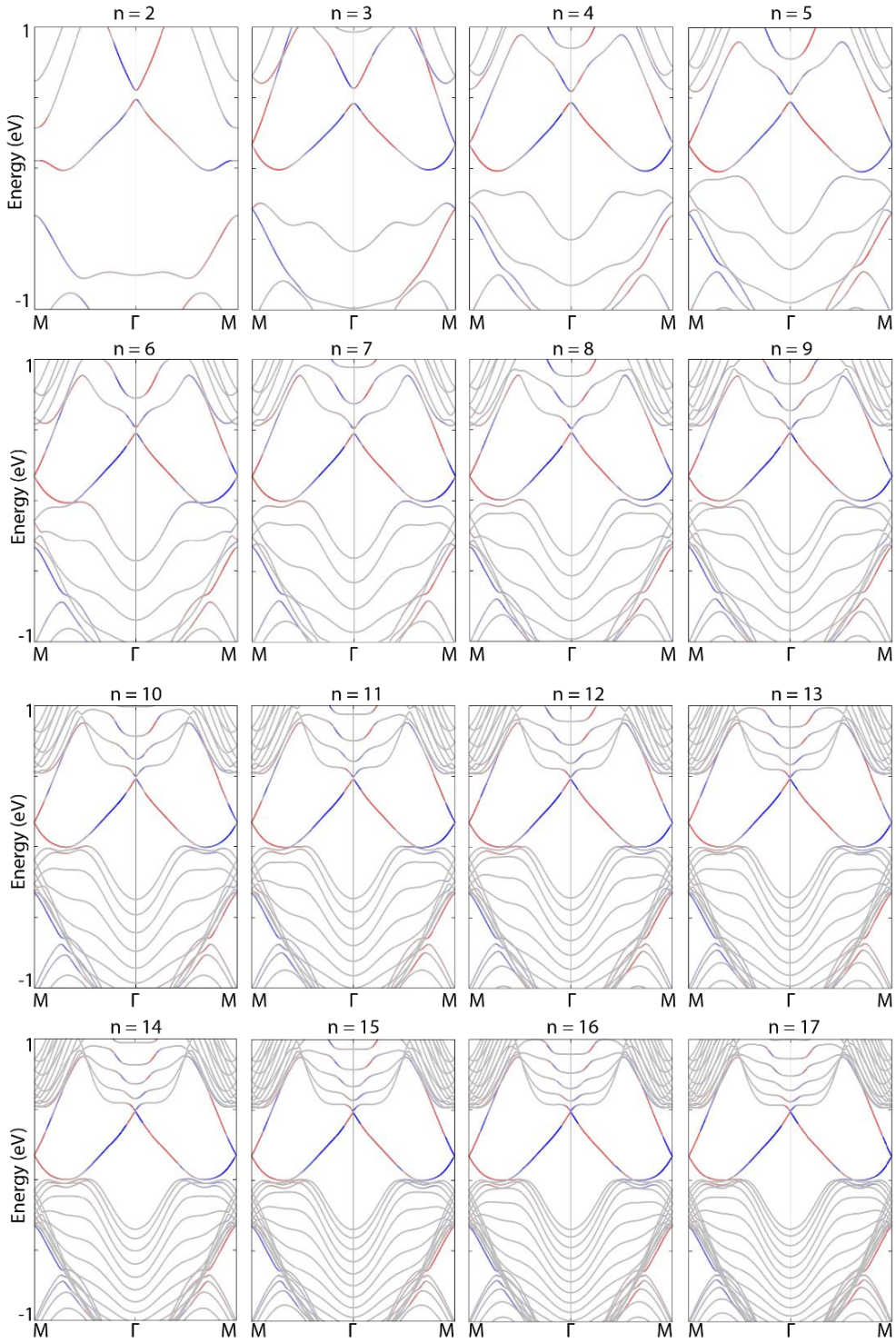

Figure 7.11 ZZ nanoribbon band structure as the slab number n grows from 2 to 17.

7.6 Conclusions

Bandgap can be opened by controlling the interfacial distance between the substrate and the thin film, in that case, the interfacial distance acts as a switch to turn on and off the conduction channels, making it helpful for a switchable topological device. The fact that TCI edge states are so vulnerable to the one-sided substrate also encourages further studies in tuning the edge state structure with the electrical field, and antisymmetric stacking configuration. Those factors have also proved effective to tune the edge states. We have generalised the interaction using the mirror symmetry breaking Rashba term and have replicated the effect resulting in 118meV band gap, indicating the effect can be generalised to mirror symmetry breaking terms for similar systems. The Rashba term also corresponds to the electric field. The overall edge band gap and the degeneracies at TRIMs can also be tuned when the nanoribbon is narrow (less than about 4nm).

Chapter 8 Tuning The Electronic Structure of In2Se3

8.1 Introduction

Layered van der Waals' chalcogenide materials are known for their wide range of promising properties that can be applied for various applications in electronics [166]. Out of all those materials, In2Se3 is characterised by room temperature ferroelectricity that can be used as a field-effect transistor [167]. However, due to the complication in its structure the materials so many possible phases [108] are discovered, which include α-In2Se3 phase(2H), α phase(3R), β phase(3R) γ-In2Se3(3R), etc. The variation in the structures also leads to various band gaps, including the experimental band gap ranging from 1.26eV to 2eV [168, 169], and the calculated band gap ranging from 0.7eV to 2.95eV [170]. The theoretical band gap is strongly dependent on potentials.

As early as 1966, there have been reports on the two main types of In2Se3 structures α phase and β phase [171]. Although they are both 3R structures, there is a difference in the stacking order between those two phases. Multiple phases may exist depending on the temperature and heating/cooling process. One example path is demonstrated in **Figure 8.1** At room temperature, the most stable phase is the α phase. After being heated to 200℃, it can be transformed into the β phase. If the materials are cooled to the temperature between 60℃ and 200℃. The material will transform into an intermediate the β' phase before transforming back to the α phase.

Previously the experimental results have identified that the β' phase cannot be maintained under 60℃ [172]. However, using high-quality crystals, our experimental collaborators have demonstrated that the β'- In2Se3 phase can be stably maintained at room temperature [173]. Because of the polarization, the material has demonstrated in-plane ferroelectricity [174].

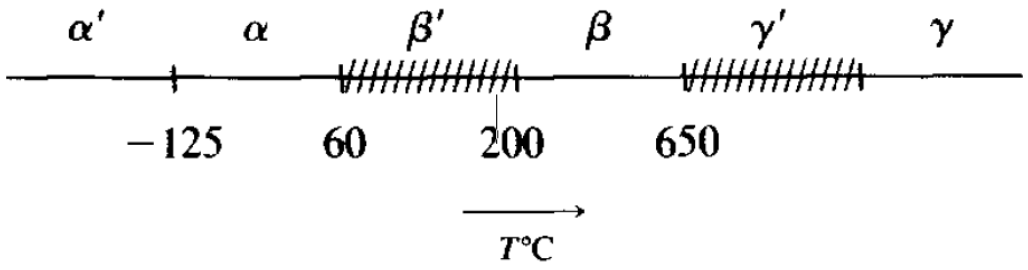

Figure 8.1 The transformation between different In2Se3 phases depending on temperature, and heating/cooling process. The horizontal line indicates the heating process, while the slashed line indicates the cooling process. Graph taken from [175].

Our collaborators have also demonstrated the moderate band gap (0.97eV indirect band gap and 1.46eV direct bandgap) through ARPES measurement [176]. In another study, our collaborators have demonstrated large piezo-resistance.

In this work, the electronic band structures of In2Se3 are studied and compared with the experimental results. The good matching between those two provides us with insights on the electronic property of β'- In2Se3 material. The piezo-resistance of the material's orbital is further studied by using DFT. The orbital projected band structure also helps to explain the mechanism of the large piezo-resistance.

8.2 Electronic Structure of In2Se3 and its Special Properties.

8.2.1 Computational Methods

First-principles calculations are conducted using Vienna Ab-Initio Simulation Package (VASP) [124, 125]. All structures are fully relaxed until the force between ions are less than 0.01 eV/Å. The atomic relaxation and band structure calculation are performed in the PBE level [138] with the exchange-correlation potential approximated by GGA [123]. The Brillouin Zone of bulk In2Se3 is sampled with 21×21×3 kpoints grid. The energy cut-off was set to 400eV. The band structure is further analysed in the HSE scheme [177] to better approximate the experimental bandgap.

8.2.2 From β to β' of In2Se3 and their Band Structures

The bulk β (3R) phase In2Se3 can either be presented with rhombohedral unit cells (see **Figure 8.2(a)),** or hexagonal unit cells (see **Figure 8.2(b)**)**.** It belongs to R$\bar{3}$M space group. Choosing different cells results in different band paths of high symmetry points. (see **Figure 8.2(d)** and **Figure 8.2(e)**). β phase itself has perfect R$\bar{3}$M symmetry, with lattice parameter a=b =4.00 Å and c=27.79 Å. When distorted to the β' phase, the ABCAB stacking order remains the same, the In layer between two Se layers are distorted slightly. After distortion, the lattice parameter became a= 3.99 Å, b=4.11 Å and c=28.27 Å. The β' phase is presented in a hexagonal unit cell to better account for the phase change and compare with the experiments. The β' phase is relaxed from a structure slightly distorted from the β phase. The energy difference E(β)-E(β') is 0.19eV/ unit cell, indicating that the β' phase is more stable than the β phase.

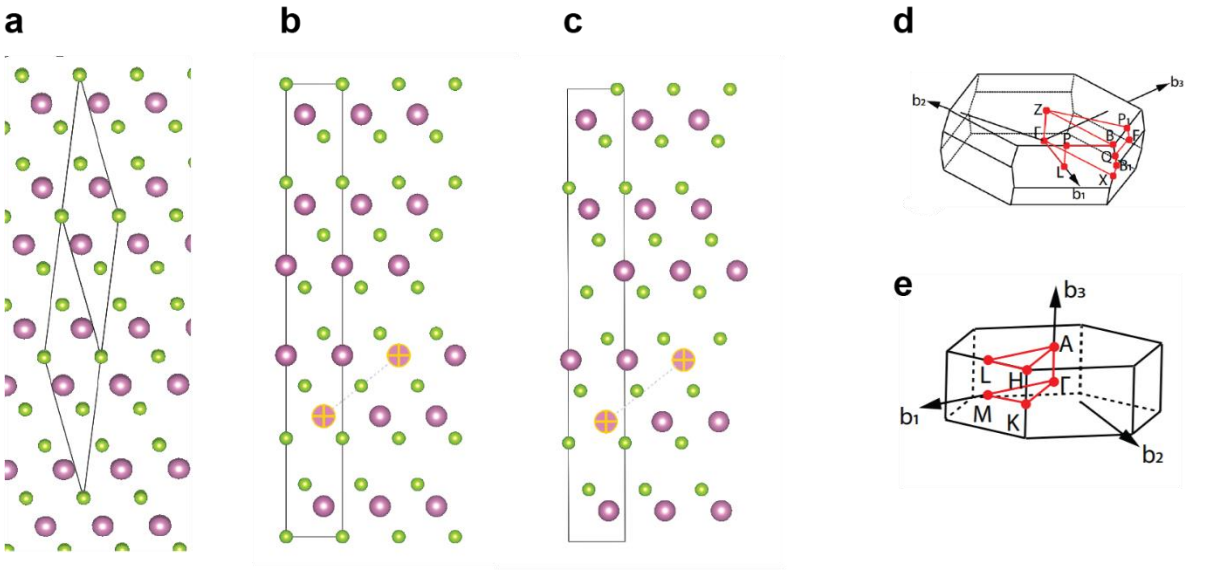

Figure 8.2 In2Se3 β phase is presented with **(a)** rhombohedral unit cell **(b)** hexagonal unit cell, and In2Se3 β' phase presented with **(c)** hexagonal unit cell. **(d)**Brillouin zone for rhombohedral unit cell. **(e)** Brillouin zone for hexagonal unit cell. **(d)** and **(e)** are taken from Ref [178].

The β phase In2Se3 band structure is presented in **Figure 8.3 (a)** using PBE-GGA and **8.3 (b)** using HSE method. For many semiconductors, DFT calculations are expected to underestimate the band gap, while the HSE method generally would give a more accurate result among all functionals [179]. Since HSE is computational resource-consuming, we use a less dense kpoint. Therefore, in our calculation, the HSE results provide more accuracy in the band gap, while PBE-GGA results provide more details in the band shape. The difference that this effect causes is material specific. In terms of β In2Se3, the functional role becomes significant. In the PBE-GGA calculation, the indirect band gap is closed between Γ, and L point, making the band

structure like metal, while in the HSE calculation the indirect band gap is calculated as 0.45eV between the L point, and the point between X and Γ. Both our band shape and bandgap in **Figure 8.3(b)** are consistent with the HSE calculation in previous studies [178]. Our band shape of PBE-GGA and HSE calculation are also consistent with each other. This is considered a benchmark to conduct further calculations. Therefore, the HSE band structures will be mainly used in the following In2Se3 calculation. However, we should realise that because DFT underestimates the band gap, even the HSE band gap may deviate significantly from experimental results (1.55eV in Ref. [180]).

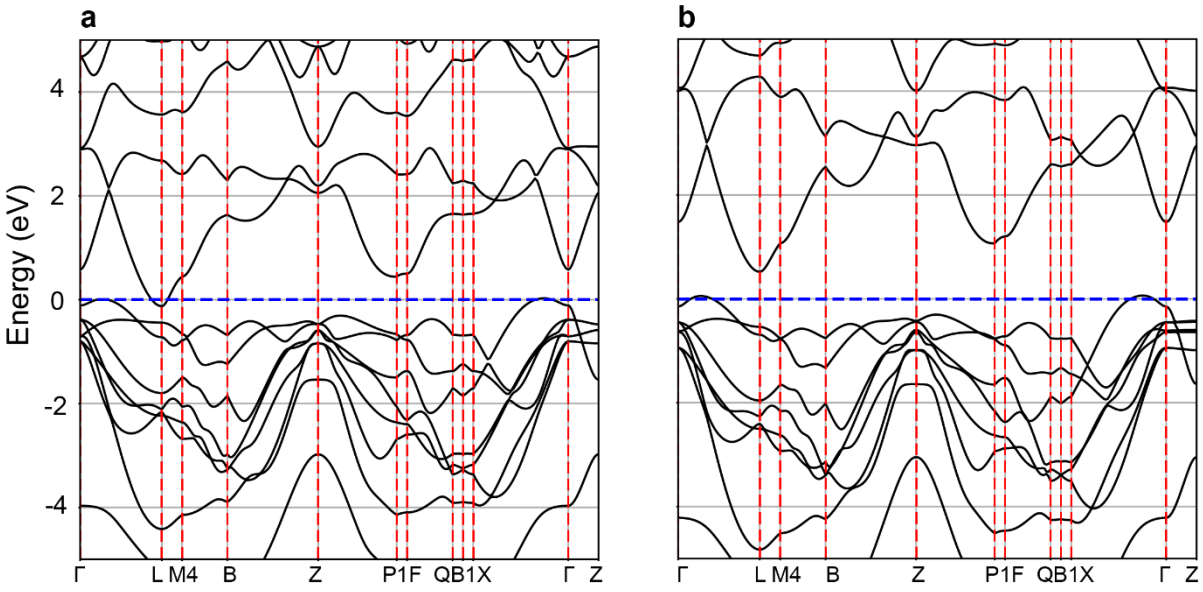

Figure 8.3 Band structure of In2Se3 using the primitive unit cell calculated via **a** PBE-GGA method and **b** HSE method**.**

The electronic band structure for β and β' phases are plotted in **Figure 8.4(a)** and **Figure 8.4(b)** respectively. Compared to the β phase, the HSE band gap for β' phase has been increased to 0.64eV. which is higher than the undistorted phase.

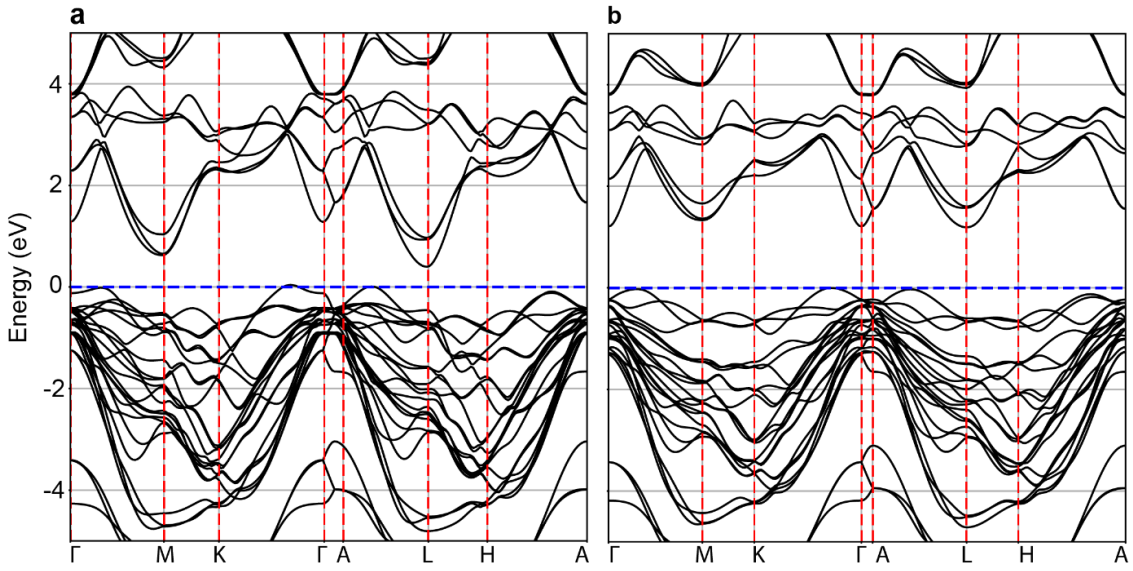

Figure 8.4 Band structure for **(a)** β and **(b)** β' phase In2Se3 using hexagonal unit cell. Both phases are calculated with HSE functionals.

The DFT and structures are compared with ARPES results from our experimental collaborators. The curve is shown in **Figure 8.5** Since the experiments were conducted on the In2Se3 surface, the DFT band structure along the Γ-M-K-Γ and A-L-H-A path in the Brillouin zone are projected together to Γ-M-K-Γ of the ARPES band structure. The HSE band gap (0.46eV) is lower compared to the experimental band gap (0.97eV). The direct band gap at M and Γ point is 1.17eV and 0.93eV respectively, which are lower compared to the experimental direct band gap 1.46eV and 1.77eV. To better compare the band shape with the experimental results, the HSE band gap between the valence band and the conduction band has been manually enlarged 0.33eV, so the two indirect band gaps can match with each other. As shown in **Figure 8.5(a).** We can find that the shape of HSE valence band top matches well with the experimental results through the Γ-M-K-Γ path. The experimental Fermi level crosses through the electron pocket

in the conduction band, suggesting this is an n-doped material. The most intensive band from the experimental results is located at about 0.8eV below the Fermi level at Γ point, and the conduction band bottom at M point. Both can be matched with the dense HSE bands. **Figure 8.5(b)** shows the planar electron pocket near the Fermi level on the kx-ky plane. The circle-shaped ARPES band structure around the M point between K and K' also matches well with the DFT band structure. **Figure 8.5(c)** shows the valence band maxima, which is 1.76eV below the Fermi level. The ARPES band density is peaked slightly away from the Γ point, which suggests that it is consistent with the HSE band structure. **Figure 8.5(d)** the purple diamond curves are extracted from the Gaussian fits of the ARPES band structure. And the shape of the conduction electron pocket DFT structure fits almost exactly with the ARPES band structure. The effective mess calculated is about 0.39 m_0(ΓM) and 0.27 m_0 (KM), which is close to the range (0.328 ± 0.01) m_0 and (0.208 ± 0.01) m_0 (KM).

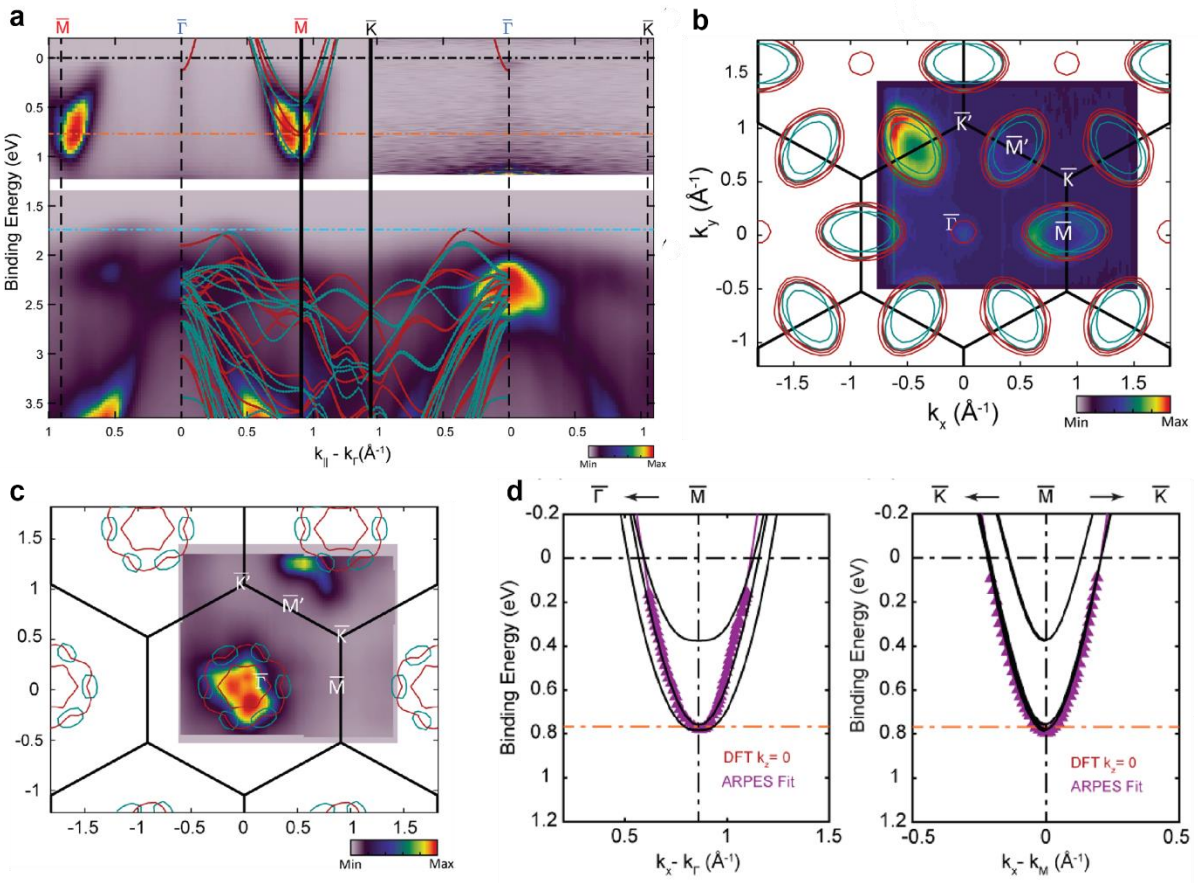

Figure 8.5 Comparison of DFT results with experimental results. (**a)** DFT electronic structure (lines) compared with Energy dispersion curves obtained from ARPES measurements (coloured maps). The black, red and blue dash lines indicate the experimental Fermi level, the conduction band minima and the valence band maxima separately. Fermi surface and electron pocket mapping comparing DFT results (lines) with the ARPES results (coloured maps) taken at **(b)** Fermi level and **(c)** Fermi level -1.76eV. In **(a)(b)** and **(c),** the red colour lines indicate follows the band high symmetry path Γ, M, K Γ (kz=0) while the turquoise curves follow the path the A, L, H, A (kz=π/c). The colour scale indicates the kz range correspondence to hv 56.5 to 90 eV. **(d)** Electron conduction pocket around M. Purple

diamond curves indicate the band location extracted from energy distribution curves, while the block lines indicate the DFT results. Graphs taken from Ref. [176].

8.3 Large Piezo-Resistivity of In2Se3.

Our experimental collaborators have discovered giant room temperature piezoresistance in In2Se3. This can be modelled and explained with our first-principles calculation. **Figure 8.6** shows the evolution of atomic structures as the pressure is growing from **(a)** 0GPa to **(e)** 4GPa. As the pressure is increased, the Se in the middle of the two In layers moves towards the line between two Se layers. As a result, the symmetry of the structure changes from distorted R3m phase to undistorted R3m. The new phase as shown in **Figure 8.6 (e)** restored the nearly perfect R3m symmetry, similar to the original β phase. During the pressure increase, the unit cell dimension has become smaller. This can be inferred from the dimension change from **Figure 8.6 (a)** to **(e)**. The exact change in the dimension can be found in **Table 8-1.** As the pressure increases, the difference in length between vectors **a** and **b** also decreases from 0.14 Å to 0 Å. **Figure 8.7** shows the volume reduction as the pressure is increased. We can observe the sudden reduction of volume between 3.5GPa and 4GPa, which further proves the phase transformation.

This can be further proved through the HSE band structure. As shown in **Figure 8.8,** the indirect band gap at high symmetry point L decreases when the pressure increases from 1GPa to 4GPa (see **Figure 8.8 (a)-(d)**). At 4GPa, the indirect band gap closes, and the material becomes a semimetal. We believe this is the reason why the material has a large reduction in the resistance during the pressure increase. The detailed orbital projected band structure evolution under pressure is plotted in **Figure 8.9(a)-(d)**. We found that the valence band is

mainly contributed by the pz orbital of the In atom, while the electron pocket near the conduction band minima is mainly contributed by a mixture of In-s and Se-px+py orbitals. As the pressure increases, the electron pocket contributed by In-s and Se-px+py orbitals are driven closer to the valence band and finally pass through the Fermi level at 3GPa (PBE-GGA), or 4GPa (HSE). This is consistent with the experimental finding that the electron density is increased when added pressure, suggesting the material is n-doped. The giant piezoresistive is dominated by the delocalised electron density and mobility contributed by In-5s and Se-4p orbitals.

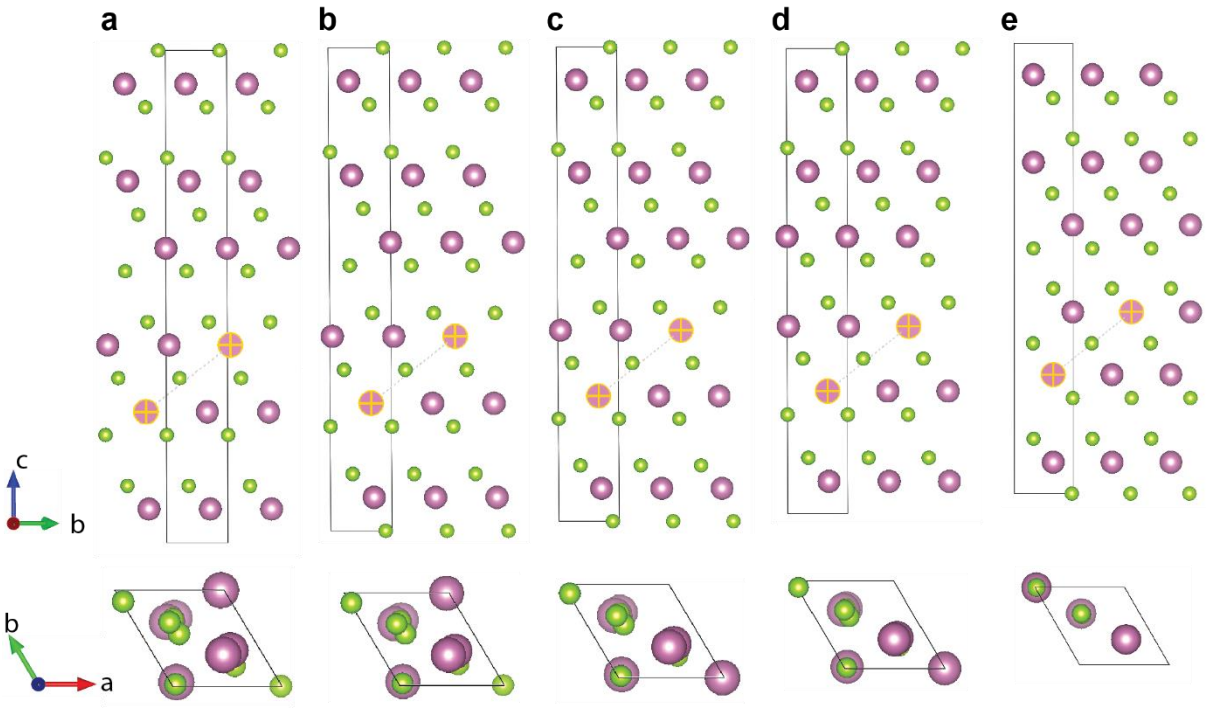

Figure 8.6 β’ In2Se3 under **a**(0GPa), **b**(1GPa), **c**(2GPa), **d**(3GPa), **e**(4GPa). The upper image shows the projected graph along a direction. The lower image shows the projected graph along c direction. A

dashed line has been drawn connecting two highlighted In atoms to compare with the position of the Se atom. The size of dimension approximately reflects the ratio of size change in response to pressure.

Table 8-2 The dimension of the unit cell under different pressures

	0GPa	1GPa	2GPa	3GPa	4Gpa
A	3.98	3.97	3.95	3.95	3.94
B	4.12	4.08	4.05	4.00	3.94
C	28.31	27.57	27.09	26.63	26.12

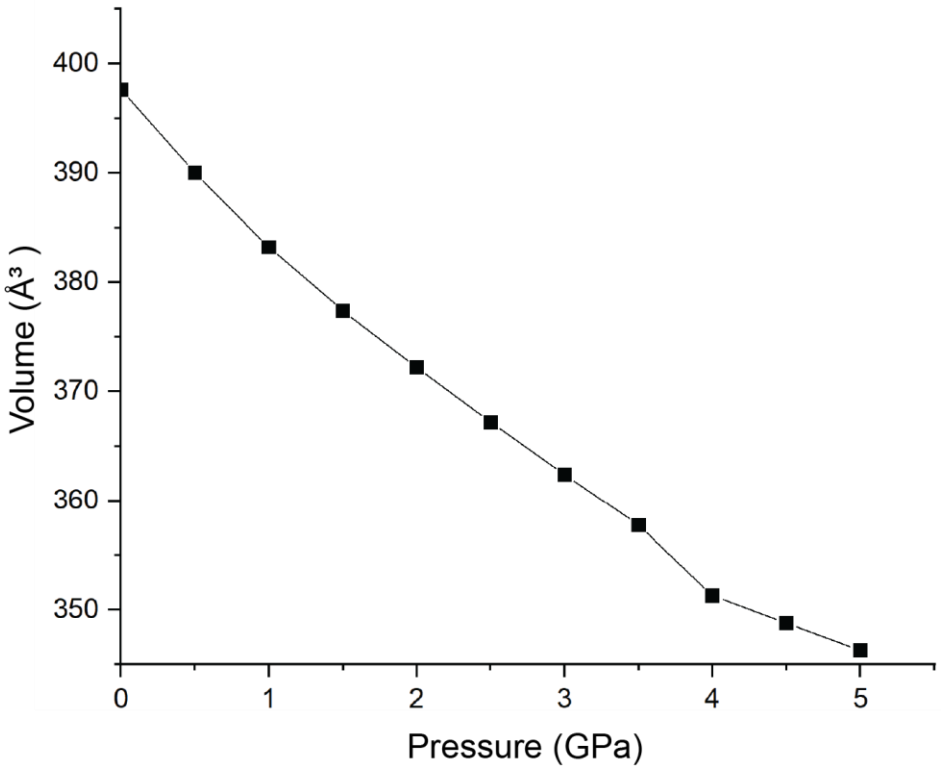

Figure 8.7 Volume ($Å^3$) vs Pressure (GPa) curve.

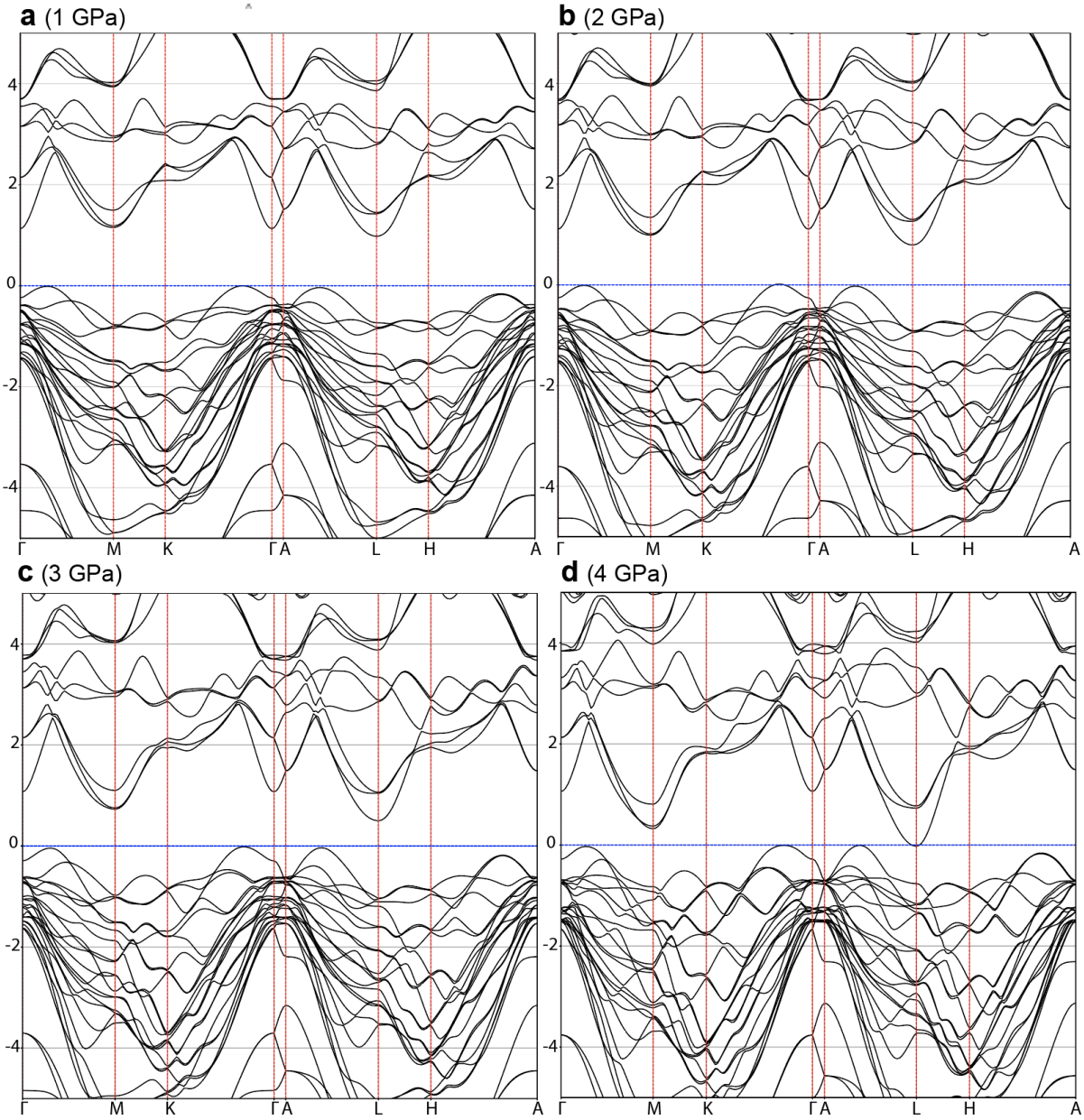

Figure 8.8 HSE Band evolution from under the pressure **(a)** 1 GPa, **(b) 2** GPa, **(c)** 3 GPa, and **(d)** 4 GPa.

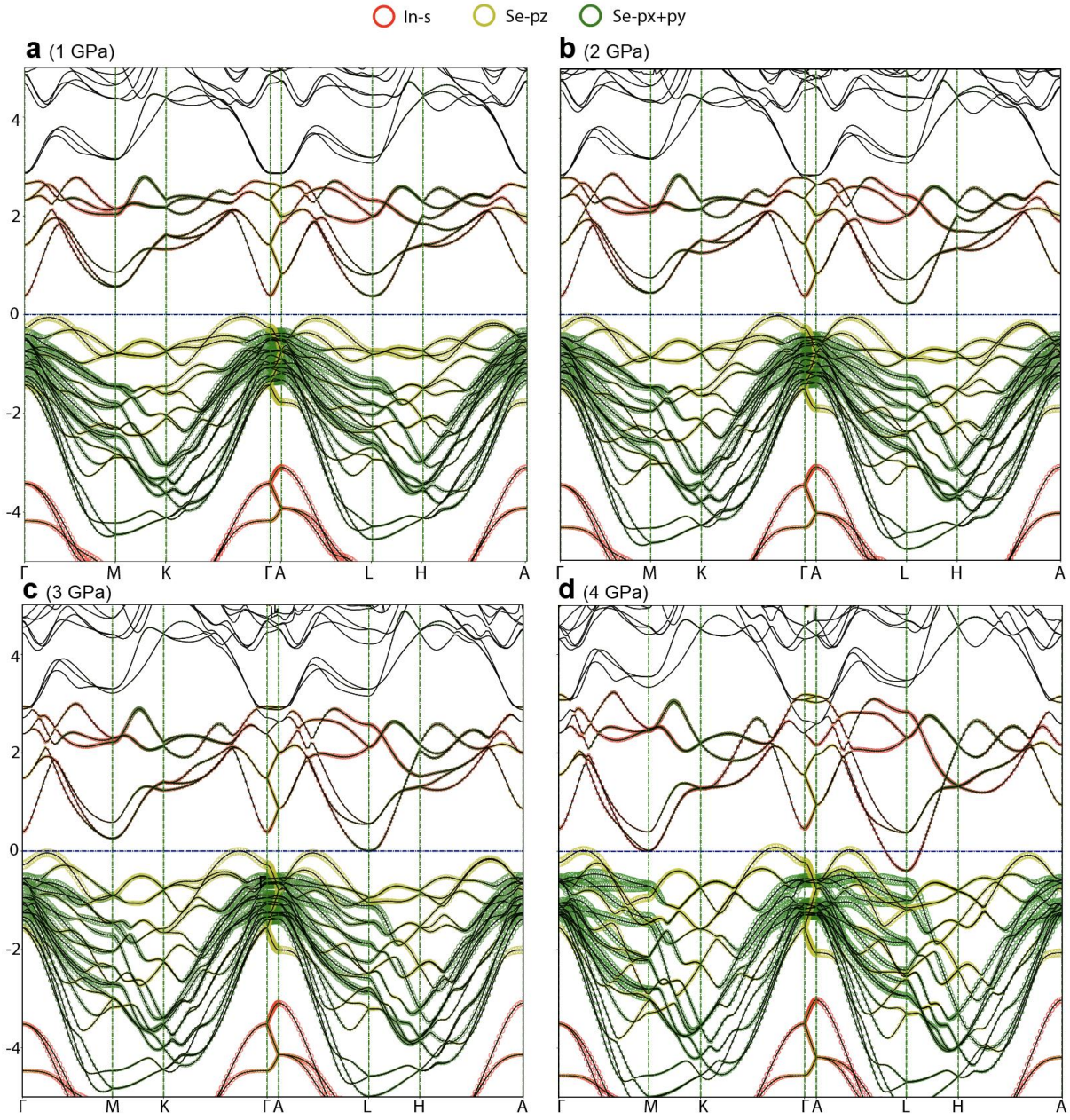

Figure 8.9 Orbital projected band evolution from under the pressure (a) 1 GPa, (b) 2 GPa, (c) 3 GPa, and (d) 4 GPa.

8.4 Conclusions

We have calculated the electronic structures for β’ In2Se3. The computational results are consistent with the experimental results, suggesting the material to be a large bandgap (>1eV) semiconductor. Our research also uncovered the mechanism that triggers the large piezo-resistance of the material, which is dominated by the delocalisation of In-5s and Se-4p orbitals. The large bandgap character and the sensitive band gap change against the pressure bring us the inspirations in electronics design. In terms of topological insulators, the large band gap makes it a good substrate for thin film topological insulators. The piezo-resistance character brings an example of how the bulk band gap can be tuned for a vdW material, inspiring the search for tunable topological materials.

Chapter 9 Conclusions and Future Works

9.1 Concluding Remarks

The thesis uses the first-principles approach to study the electronic structures of various designs in the topological field. As a material with large spin-orbit coupling, two-dimensional bismuth has proved the capability to host various types of topological states when controlling the variation in allotrope type, number of layers, and especially, the interaction from the substrates.

- Bismuth is a playground for rich topological phenomena. The materials Bi (111) BL, 2ML/4ML/6ML Bi (110) and Bi/SiC(0001) are demonstrated as Z_2 TIs, while the freestanding planar bismuthene is a 2D TCI. Orbital filtering effect is demonstrated on Bi/SiC (0001) and on BiF. Those results are consistent with previous experimental and theoretical studies.
- The Bismuthen/BiF interface states incorporate features from both TI (band number/shape) and TCI (bulk band gap).
- The 2ML/4ML 6ML Bi (110) non-trivial edge states DOS matches well with the experimental results. The depth of the states captured by the experiment is around 4Å

Using planar bismuthene as a model, our interests mainly focus on maintaining and tuning the topological edge states of topological crystalline insulators. As crystalline mirror symmetry can be easily turned off, 2D TCI edge states are previously expected to break easily. However, our studies have shown multiple approaches to maintain the edge states.

- When the substrate has only weak interaction against the thin film, the topological feature of TCI survives the mirror symmetry breaking effect.
- A sandwich stacking of substrates helps to preserve the thin film edge states even when there is a stronger substrate-thin film interaction.
- Controlling the edge termination helps the edge states survive from mirror-symmetry breaking field. Those edge terminations host edge state degeneracies only at high symmetry kpoints. Although the vulnerability against change in edge termination means that the edge states are no longer topologically protected against edge defects, the spin-filtered nature of the edge states does not change. Therefore, the material is still suitable as a spin current generator in spintronic applications.

For a non-special edge termination, that is, the termination with some edge states degeneracies located at generic kpoints, the band gap can be tuned conveniently through adding pressure, applying electric field, controlling the substrate configuration, and reducing nanoribbon width. Unlike Z_2 TI materials, the breaking of those band gaps occurs at degeneracy points where no bulk band closure is needed. Therefore, it becomes applicable for electronics that require high-speed turning on and off operations. We found that both the pressure and the electric field needed is within the practical range. Several examples are:

- The maximum edge bandgap (118meV) is reached at about 1.75V/nm for planar bismuthene with armchair edge.
- About 7GPa and 30 GPa is needed for Bi/SiCH-(0001) and Bi/h-BN respectively to reach the maximum band gap.

- With Bi/h-BN rotated sandwich structure applied, the effect of opening the edge band gap via adding pressure is about doubled.

Besides bismuth, β’ In2Se3 is another material we have studied in this thesis. We mainly focused on comparing our computational model with experimental results. The results have suggested that β’ In2Se3 is a large band gap semiconductor with strong piezo-resistance. Therefore, it can be used as a substrate to support thin film topological insulators. Also, the mechanism of band evolution brought inspiration for the design of band gap tunable materials, including topological insulators.

9.2 Future works

The thesis has demonstrated the robustness and tunability of 2D TCIs. The next step is to synthesize them through experiment. According to our current knowledge, there have been no reports on confirmed observation of mirror-symmetry protected two-dimensional topological crystalline insulators. One reason is that the interaction from substrates breaks the TCI symmetry. However, although not mentioned by the authors, we believe 2D TCIs have already been synthesized in Shao et al’s paper [71] for antimonene on Ag (111) systems. After the annealing process, they have fabricated planar antimonene on the very inert Ag (111) substrate. From the Figure S4 of Shao et al’s paper [71], we can identify a significant difference in both the bulk band structure and the nontrivial edge state within the nanoribbon band structure, between a planar antimonene and buckled Sb (111) BL. In the meantime, Hsu et al, [77] proved

that planar antimonene and planar bismuthene share the same TCI topological nature. Since Ag (111) is metallic, the edge state of antimonene is buried in the Ag metallic states. Also, antimonene has a small bulk band gap compared to bismuthene. However, Shao et al.'s experiment has demonstrated that it is possible to fabricate planar TCI on weak substrates. With similar experimental strategies, fabricating bismuthene on a non-metallic inert substrate (such as h-BN in our study) is also possible. The other thing to try is the sandwich structure. Once fabricated, the band structure can be studied by ARPES measurement, while the edge states can be mapped out through STS measurement to verify our theoretical results.

The next steps are to use the pressure/electrical field approach to turn the material on/off. The different responses from ZZ/AC should be demonstrated. In this thesis, we have demonstrated the approximate range of parameters such as pressure and electric field. These parameters need to be optimised in experiments and combined with alternating substrate configuration to study the most efficient way to tune it on and off.

The materials used in 2D TCI are not limited to bismuthene and Group V materials. Both theoretical and experimental studies can be extended to other 2D TCI materials. Unlike bismuthene, many other 2D TCIs adopt rectangular unit cells, such as PbSe monolayer [76]. Rectangular unit cells apply a different Brillouin zone, and therefore the edge state may act differently under mirror symmetry breaking field.

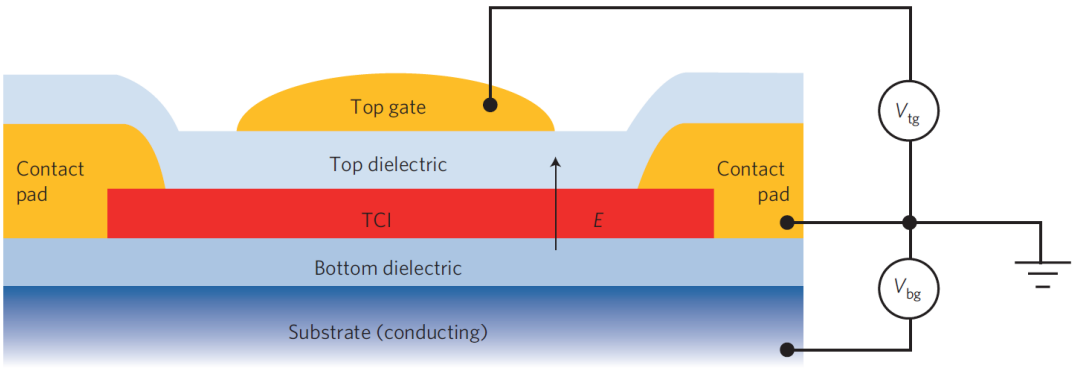

Figure 9.1 A switchable TCI transistor. Graph taken from [75].

With optimised materials, substrate and parameters to maintain and tune the edge states, a TCI topological transistor device following Liu et al.'s concept [75] can be created. The edge current transport, in this case, will be dissipationless.

Reference

1. Hsieh, T.H., et al., *Topological crystalline insulators in the SnTe material class.* Nature Communications, 2012. **3**: p. 982.
2. Kou, L., et al., *Two-Dimensional Topological Insulators: Progress and Prospects.* The Journal of Physical Chemistry Letters, 2017. **8**(8): p. 1905-1919.
3. Zunger, A., *Beware of plausible predictions of fantasy materials*. 2019, Nature Publishing Group.
4. Ren, Y., Z. Qiao, and Q. Niu, *Topological phases in two-dimensional materials: a review.* Reports on Progress in Physics, 2016. **79**(6): p. 066501.
5. Moore, G.E., *Cramming more components onto integrated circuits. Electronics 38 (8): 114–117*. 1965.
6. Mack, C.A., *Fifty Years of Moore's Law.* IEEE Transactions on Semiconductor Manufacturing, 2011. **24**(2): p. 202-207.
7. Fritze, M., *Post-Moore: prospects for novel patterning of low volume ICs*. SPIE Advanced Lithography. Vol. 11610. 2021: SPIE.
8. Mok, M.P.C., et al. *Chiplet-based System-on-Chip for Edge Artificial Intelligence*. in *2021 5th IEEE Electron Devices Technology & Manufacturing Conference (EDTM)*. 2021.
9. Waldrop, M.M., *The chips are down for Moore's law.* Nature News, 2016. **530**(7589): p. 144.
10. Loh, G.H., S. Naffziger, and K. Lepak. *Understanding Chiplets Today to Anticipate Future Integration Opportunities and Limits*. in *2021 Design, Automation & Test in Europe Conference & Exhibition (DATE)*. 2021.
11. Powell, J.R., *The Quantum Limit to Moore's Law.* Proceedings of the IEEE, 2008. **96**(8): p. 1247-1248.
12. Xiu, L., *Time Moore: Exploiting Moore's Law From The Perspective of Time.* IEEE Solid-State Circuits Magazine, 2019. **11**(1): p. 39-55.
13. Kumar, S., *Fundamental Limits to Moore's Law.* arXiv preprint arXiv:1511.05956, 2015.
14. Pop, E., R.W. Dutton, and K.E. Goodson, *Monte Carlo simulation of Joule heating in bulk and strained silicon.* Applied Physics Letters, 2005. **86**(8): p. 082101.
15. Andrae, A.S.G. and T. Edler, *On Global Electricity Usage of Communication Technology: Trends to 2030.* Challenges, 2015. **6**(1): p. 117-157.
16. *Double, double, toil and trouble.* The economist, 2016.

17. Zhang, H., et al., *Topological insulators in Bi2Se3, Bi2Te3 and Sb2Te3 with a single Dirac cone on the surface.* Nature Physics, 2009. **5**: p. 438.

18. König, M., et al., *Quantum Spin Hall Insulator State in HgTe Quantum Wells.* Science, 2007. **318**(5851): p. 766-770.

19. Schindler, F., et al., *Higher-order topological insulators.* Science Advances, 2018. **4**(6): p. eaat0346.

20. Schindler, F., et al., *Higher-order topology in bismuth.* Nature Physics, 2018. **14**(9): p. 918-924.

21. Benalcazar, W.A., B.A. Bernevig, and T.L. Hughes, *Quantized electric multipole insulators.* Science, 2017. **357**(6346): p. 61-66.

22. Ren, Y., Z. Qiao, and Q. Niu, *Engineering Corner States from Two-Dimensional Topological Insulators.* Physical Review Letters, 2020. **124**(16): p. 166804.

23. Feng, Y.P., et al., *Prospects of spintronics based on 2D materials.* Wiley Interdisciplinary Reviews: Computational Molecular Science, 2017. **7**(5): p. e1313-n/a.

24. Paudel, H.P. and M.N. Leuenberger, *Three-dimensional topological insulator quantum dot for optically controlled quantum memory and quantum computing.* Physical Review B, 2013. **88**(8): p. 085316.

25. Hasan, M.Z. and C.L. Kane, *Colloquium: Topological insulators.* Reviews of Modern Physics, 2010. **82**(4): p. 3045-3067.

26. Bansil, A., H. Lin, and T. Das, *Colloquium.* Reviews of Modern Physics, 2016. **88**(2): p. 021004.

27. Qi, X.-L. and S.-C. Zhang, *Topological insulators and superconductors.* Reviews of Modern Physics, 2011. **83**(4): p. 1057-1110.

28. Hall, E.H., *On a new action of the magnet on electric currents.* American Journal of Mathematics, 1879. **2**(3): p. 287-292.

29. Hall, E., *On the possibility of transverse currents in ferromagnets.* Philos. Mag, 1881. **12**: p. 157-160.

30. Karplus, R. and J.M. Luttinger, *Hall Effect in Ferromagnetics.* Physical Review, 1954. **95**(5): p. 1154-1160.

31. Nagaosa, N., et al., *Anomalous Hall effect.* Reviews of Modern Physics, 2010. **82**(2): p. 1539-1592.

32. Klitzing, K.v., G. Dorda, and M. Pepper, *New Method for High-Accuracy Determination of the Fine-Structure Constant Based on Quantized Hall Resistance.* Physical Review Letters, 1980. **45**(6): p. 494-497.

33. Thouless, D.J., et al., *Quantized Hall Conductance in a Two-Dimensional Periodic Potential.* Physical Review Letters, 1982. **49**(6): p. 405-408.

34. Simon, B., *Holonomy, the Quantum Adiabatic Theorem, and Berry's Phase.* Physical Review Letters, 1983. **51**(24): p. 2167-2170.

35. Haldane, F.D.M., *Model for a Quantum Hall Effect without Landau Levels: Condensed-Matter Realization of the "Parity Anomaly".* Physical Review Letters, 1988. **61**(18): p. 2015-2018.

36. Novoselov, K.S., et al., *Electric Field Effect in Atomically Thin Carbon Films.* Science, 2004. **306**(5696): p. 666-669.

37. Kane, C.L. and E.J. Mele, *Quantum Spin Hall Effect in Graphene.* Physical Review Letters, 2005. **95**(22): p. 226801.

38. Bernevig, B.A., T.L. Hughes, and S.-C. Zhang, *Quantum Spin Hall Effect and Topological Phase Transition in HgTe Quantum Wells.* Science, 2006. **314**(5806): p. 1757-1761.

39. Fu, L. and C.L. Kane, *Topological insulators with inversion symmetry.* Physical Review B, 2007. **76**(4): p. 045302.

40. Hsieh, D., et al., *A topological Dirac insulator in a quantum spin Hall phase.* Nature, 2008. **452**: p. 970.

41. Liu, Z.K., et al., *Discovery of a Three-Dimensional Topological Dirac Semimetal, Na3Bi.* Science, 2014. **343**(6173): p. 864-867.

42. Xu, S.-Y., et al., *Discovery of a Weyl fermion semimetal and topological Fermi arcs.* Science, 2015. **349**(6248): p. 613-617.

43. Chang, C.-Z., et al., *Experimental Observation of the Quantum Anomalous Hall Effect in a Magnetic Topological Insulator.* Science, 2013.

44. Vergniory, M.G., et al., *A complete catalogue of high-quality topological materials.* Nature, 2019. **566**(7745): p. 480-485.

45. Fu, L. and C.L. Kane, *Time reversal polarization and a Z2 adiabatic spin pump.* Physical Review B, 2006. **74**(19): p. 195312.

46. SHEN, S.-Q., *TOPOLOGICAL INSULATORS: Dirac Equation in Condensed Matter*. 2017: SPRINGER.

47. Kane, C.L. and E.J. Mele, *Z2.* Physical Review Letters, 2005. **95**(14): p. 146802.

48. Hatsugai, Y., *Chern number and edge states in the integer quantum Hall effect.* Physical Review Letters, 1993. **71**(22): p. 3697-3700.

49. Chang, C.-Z., et al., *Experimental Observation of the Quantum Anomalous Hall Effect in a Magnetic Topological Insulator.* Science, 2013. **340**(6129): p. 167-170.

50. Liu, C.-X., et al., *Quantum Anomalous Hall Effect in Hg1-yMnyTe Quantum Wells.* Physical Review Letters, 2008. **101**(14): p. 146802.

51. Zhao, Y.-F., et al., *Tuning the Chern number in quantum anomalous Hall insulators.* Nature, 2020. **588**(7838): p. 419-423.

52. Focassio, B., et al., *Dual topological insulator device with disorder robustness.* Physical Review B, 2020. **102**(4): p. 045414.

53. 戴希, *凝聚态材料中的拓扑相与拓扑相变——2016 年诺贝尔物理学奖解读.* 物理, 2016. **45**(12): p. 757-768.

54. Wang, Z.F., Z. Liu, and F. Liu, *Organic topological insulators in organometallic lattices.* Nature Communications, 2013. **4**: p. 1471.

55. Kim, H.-S., et al., *Strain-induced topological insulator phase and effective magnetic interactions in Li2IrO3.* Physical Review B, 2013. **87**(16): p. 165117.

56. Liu, Q., et al., *Switching a Normal Insulator into a Topological Insulator via Electric Field with Application to Phosphorene.* Nano Letters, 2015. **15**(2): p. 1222-1228.

57. Liu, L., et al., *Two-dimensional topological semimetal states in monolayer Cu2Ge, Fe2Ge, and Fe2Sn.* Physical Review B, 2020. **101**(16): p. 165403.

58. Xia, H., et al., *Dimensional Crossover and Topological Phase Transition in Dirac Semimetal Na3Bi Films.* ACS Nano, 2019. **13**(8): p. 9647-9654.

59. Mutch, J., et al., *Evidence for a strain-tuned topological phase transition in ZrTe₅.* Science Advances, 2019. **5**(8): p. eaav9771.

60. Collins, J.L., et al., *Electric-field-tuned topological phase transition in ultrathin Na3Bi.* Nature, 2018. **564**(7736): p. 390-394.

61. Wang, Z.F., K.-H. Jin, and F. Liu, *Computational design of two-dimensional topological materials.* Wiley Interdisciplinary Reviews: Computational Molecular Science, 2017. **7**(4): p. e1304-n/a.

62. Mannix, A.J., et al., *Synthesis and chemistry of elemental 2D materials.* Nature Reviews Chemistry, 2017. **1**(2): p. 0014.

63. Zavabeti, A., et al., *Two-Dimensional Materials in Large-Areas: Synthesis, Properties and Applications.* Nano-Micro Letters, 2020. **12**(1): p. 66.

64. Koma, A., *Van der Waals epitaxy—a new epitaxial growth method for a highly lattice-mismatched system.* Thin Solid Films, 1992. **216**(1): p. 72-76.

65. Dean, C.R., et al., *Boron nitride substrates for high-quality graphene electronics.* Nature Nanotechnology, 2010. **5**(10): p. 722-726.

66. Dai, Z., L. Liu, and Z. Zhang, *Strain Engineering of 2D Materials: Issues and Opportunities at the Interface.* Advanced Materials, 2019. **31**(45): p. 1805417.

67. Li, G., et al., *Structure characterization and strain relief analysis in CVD growth of boron phosphide on silicon carbide.* Applied Surface Science, 2015. **327**: p. 7-12.

68. Koma, A. and K. Yoshimura, *Ultrasharp interfaces grown with Van der Waals epitaxy.* Surface Science, 1986. **174**(1): p. 556-560.

69. Ginley, T.P., Y. Wang, and S. Law, *Topological Insulator Film Growth by Molecular Beam Epitaxy: A Review.* Crystals, 2016. **6**(11): p. 154.

70. Reis, F., et al., *Bismuthene on a SiC substrate: A candidate for a high-temperature quantum spin Hall material.* Science, 2017. **357**(6348): p. 287-290.

71. Shao, Y., et al., *Epitaxial Growth of Flat Antimonene Monolayer: A New Honeycomb Analogue of Graphene.* Nano Letters, 2018. **18**(3): p. 2133-2139.

72. Li, G., et al., *Theoretical paradigm for the quantum spin Hall effect at high temperatures.* Physical Review B, 2018. **98**(16): p. 165146.

73. Fu, L., *Topological Crystalline Insulators.* Physical Review Letters, 2011. **106**(10): p. 106802.

74. Teo, J.C.Y., L. Fu, and C.L. Kane, *Surface states and topological invariants in three-dimensional topological insulators: Application to Bi1-xSbx.* Physical Review B, 2008. **78**(4): p. 045426.

75. Liu, J., et al., *Spin-filtered edge states with an electrically tunable gap in a two-dimensional topological crystalline insulator.* Nature Materials, 2013. **13**: p. 178.

76. Wrasse, E.O. and T.M. Schmidt, *Prediction of Two-Dimensional Topological Crystalline Insulator in PbSe Monolayer.* Nano Letters, 2014. **14**(10): p. 5717-5720.

77. Hsu, C.-H., et al., *Two-dimensional Topological Crystalline Insulator Phase in Sb/Bi Planar Honeycomb with Tunable Dirac Gap.* Scientific Reports, 2016. **6**: p. 18993.

78. Deng, H.-X., et al., *Atomic-ordering-induced quantum phase transition between topological crystalline insulator and Z2 topological insulator.* arXiv preprint arXiv:1702.05697, 2017.

79. Liu, J., W. Duan, and L. Fu, *Two types of surface states in topological crystalline insulators.* Physical Review B, 2013. **88**(24): p. 241303.

80. Tanaka, Y., et al., *Experimental realization of a topological crystalline insulator in SnTe.* Nature Physics, 2012. **8**: p. 800.

81. Dziawa, P., et al., *Topological crystalline insulator states in Pb1−xSnxSe.* Nature Materials, 2012. **11**: p. 1023.

82. Semenoff, G.W., *Condensed-Matter Simulation of a Three-Dimensional Anomaly.* Physical Review Letters, 1984. **53**(26): p. 2449-2452.

83. Cucka, P. and C.S. Barrett, *The crystal structure of Bi and of solid solutions of Pb, Sn, Sb and Te in Bi.* Acta Crystallographica, 1962. **15**(9): p. 865-872.

84. Aktürk, E., O.Ü. Aktürk, and S. Ciraci, *Single and bilayer bismuthene: Stability at high temperature and mechanical and electronic properties.* Physical Review B, 2016. **94**(1): p. 014115.

85. Hofmann, P., *The surfaces of bismuth: Structural and electronic properties.* Progress in Surface Science, 2006. **81**(5): p. 191-245.

86. Murakami, S., *Quantum Spin Hall Effect and Enhanced Magnetic Response by Spin-Orbit Coupling.* Physical Review Letters, 2006. **97**(23): p. 236805.

87. Wada, M., et al., *Localized edge states in two-dimensional topological insulators: Ultrathin Bi films.* Physical Review B, 2011. **83**(12): p. 121310.

88. Liu, Z., et al., *Stable Nontrivial Z2 Topology in Ultrathin Bi (111) Films: A First-Principles Study.* Physical Review Letters, 2011. **107**(13): p. 136805.

89. Chen, L., Z.F. Wang, and F. Liu, *Robustness of two-dimensional topological insulator states in bilayer bismuth against strain and electrical field.* Physical Review B, 2013. **87**(23): p. 235420.

90. Huang, Z.-Q., et al., *Nontrivial topological electronic structures in a single Bi(111) bilayer on different substrates: A first-principles study.* Physical Review B, 2013. **88**(16): p. 165301.

91. Wang, Z.F., L. Chen, and F. Liu, *Tuning Topological Edge States of Bi(111) Bilayer Film by Edge Adsorption.* Nano Letters, 2014. **14**(5): p. 2879-2883.

92. Elias, D.C., et al., *Dirac cones reshaped by interaction effects in suspended graphene.* Nature Physics, 2012. **8**: p. 172.

93. Yang, F., et al., *Spatial and Energy Distribution of Topological Edge States in Single Bi(111) Bilayer.* Physical Review Letters, 2012. **109**(1): p. 016801.

94. Sabater, C., et al., *Topologically Protected Quantum Transport in Locally Exfoliated Bismuth at Room Temperature.* Physical Review Letters, 2013. **110**(17): p. 176802.

95. Drozdov, I.K., et al., *One-dimensional topological edge states of bismuth bilayers.* Nature Physics, 2014. **10**: p. 664.

96. Takayama, A., et al., *One-Dimensional Edge States with Giant Spin Splitting in a Bismuth Thin Film.* Physical Review Letters, 2015. **114**(6): p. 066402.

97. Yeom, H.W., K.-H. Jin, and S.-H. Jhi, *Topological fate of edge states of single Bi bilayer on Bi(111).* Physical Review B, 2016. **93**(7): p. 075435.

98. Hsu, C.-H., et al., *Topology on a new facet of bismuth.* Proceedings of the National Academy of Sciences, 2019. **116**(27): p. 13255-13259.

99. Zhou, M., et al., *Epitaxial growth of large-gap quantum spin Hall insulator on semiconductor surface.* Proceedings of the National Academy of Sciences, 2014. **111**(40): p. 14378-14381.

100. Chia-Hsiu, H., et al., *The nontrivial electronic structure of Bi/Sb honeycombs on SiC(0001).* New Journal of Physics, 2015. **17**(2): p. 025005.

101. Song, Z., et al., *Quantum spin Hall insulators and quantum valley Hall insulators of BiX/SbX (X=H, F, Cl and Br) monolayers with a record bulk band gap.* Npg Asia Materials, 2014. **6**: p. e147.

102. Wu, J., et al., *Controlled Chlorine Plasma Reaction for Noninvasive Graphene Doping.* Journal of the American Chemical Society, 2011. **133**(49): p. 19668-19671.

103. Ma, Y., et al., *Robust Two-Dimensional Topological Insulators in Methyl-Functionalized Bismuth, Antimony, and Lead Bilayer Films.* Nano Letters, 2015. **15**(2): p. 1083-1089.

104. Fu, B., et al., *A new kind of 2D topological insulators BiCN with a giant gap and its substrate effects.* Scientific Reports, 2016. **6**: p. 30003.

105. Li, S.-s., et al., *Effect of Amidogen Functionalization on Quantum Spin Hall Effect in Bi/Sb(111) Films.* ACS Applied Materials & Interfaces, 2017. **9**(47): p. 41443-41453.

106. Yaping, W., et al., Journal of Physics: Condensed Matter, 2018.

107. Nagao, T., et al., *Nanofilm Allotrope and Phase Transformation of Ultrathin Bi Film on Si(111)7*7.* Physical Review Letters, 2004. **93**(10): p. 105501.

108. Popovic, S., et al., *Revised and new crystal data for indium selenides.* Journal of Applied Crystallography, 1979. **12**(4): p. 416-420.

109. Lu, Y., et al., *Topological Properties Determined by Atomic Buckling in Self-Assembled Ultrathin Bi(110).* Nano Letters, 2015. **15**(1): p. 80-87.

110. Yao, Y., et al., *Spin-orbit gap of graphene: First-principles calculations.* Physical Review B, 2007. **75**(4): p. 041401.

111. Richardella, A., et al., *Characterizing the structure of topological insulator thin films.* APL Materials, 2015. **3**(8): p. 083303.

112. Sholl, D. and J.A. Steckel, *Density functional theory: a practical introduction*. 2011: John Wiley & Sons.

113. Martin, R.M., *Electronic structure: basic theory and practical methods*. 2004: Cambridge university press.

114. Jain, A., Y. Shin, and K.A. Persson, *Computational predictions of energy materials using density functional theory.* Nature Reviews Materials, 2016. **1**: p. 15004.

115. Born, M. and R. Oppenheimer, *Zur Quantentheorie der Molekeln.* Annalen der Physik, 1927. **389**(20): p. 457-484.

116. Misra, P., *Physics of condensed matter*. 2011: Academic Press.

117. Hartree, D.R., *The Wave Mechanics of an Atom with a Non-Coulomb Central Field. Part I. Theory and Methods.* Mathematical Proceedings of the Cambridge Philosophical Society, 1928. **24**(1): p. 89-110.

118. Fock, V., *Näherungsmethode zur Lösung des quantenmechanischen Mehrkörperproblems.* Zeitschrift für Physik, 1930. **61**(1): p. 126-148.

119. Slater, J.C., *Note on Hartree's Method.* Physical Review, 1930. **35**(2): p. 210-211.

120. Hohenberg, P. and W. Kohn, *Inhomogeneous Electron Gas.* Physical Review, 1964. **136**(3B): p. B864-B871.

121. Kohn, W. and L.J. Sham, *Self-Consistent Equations Including Exchange and Correlation Effects.* Physical Review, 1965. **140**(4A): p. A1133-A1138.

122. Perdew, J.P. and A. Zunger, *Self-interaction correction to density-functional approximations for many-electron systems.* Physical Review B, 1981. **23**(10): p. 5048-5079.

123. Langreth, D.C. and J.P. Perdew, *Theory of nonuniform electronic systems. I. Analysis of the gradient approximation and a generalization that works.* Physical Review B, 1980. **21**(12): p. 5469-5493.

124. Kresse, G. and J. Hafner, *Ab initio.* Physical Review B, 1994. **49**(20): p. 14251-14269.

125. Kresse, G. and J. Furthmüller, *Efficient iterative schemes for ab initio total-energy calculations using a plane-wave basis set.* Physical Review B, 1996. **54**(16): p. 11169-11186.

126. Blaha, P., et al., *WIEN2k.* Inst. f. Materials Chemistry, TU Vienna, 2001.

127. Paolo, G., et al., *QUANTUM ESPRESSO: a modular and open-source software project for quantum simulations of materials.* Journal of Physics: Condensed Matter, 2009. **21**(39): p. 395502.

128. Gonze, X., et al., *ABINIT: First-principles approach to material and nanosystem properties.* Computer Physics Communications, 2009. **180**(12): p. 2582-2615.

129. Grimme, S., *Semiempirical GGA-type density functional constructed with a long-range dispersion correction.* Journal of Computational Chemistry, 2006. **27**(15): p. 1787-1799.

130. Grimme, S., et al., *A consistent and accurate ab initio parametrization of density functional dispersion correction (DFT-D) for the 94 elements H-Pu.* The Journal of Chemical Physics, 2010. **132**(15): p. 154104.

131. Tkatchenko, A. and M. Scheffler, *Accurate Molecular Van Der Waals Interactions from Ground-State Electron Density and Free-Atom Reference Data.* Physical Review Letters, 2009. **102**(7): p. 073005.

132. Slater, J.C. and G.F. Koster, *Simplified LCAO Method for the Periodic Potential Problem.* Physical Review, 1954. **94**(6): p. 1498-1524.

133. Marzari, N. and D. Vanderbilt, *Maximally localized generalized Wannier functions for composite energy bands.* Physical Review B, 1997. **56**(20): p. 12847-12865.

134. Mostofi, A.A., et al., *wannier90: A tool for obtaining maximally-localised Wannier functions.* Computer Physics Communications, 2008. **178**(9): p. 685-699.

135. Marzari, N., et al., *Maximally localized Wannier functions: Theory and applications.* Reviews of Modern Physics, 2012. **84**(4): p. 1419-1475.

136. Wannier, G.H., *The Structure of Electronic Excitation Levels in Insulating Crystals.* Physical Review, 1937. **52**(3): p. 191-197.

137. Kresse, G. and D. Joubert, *From ultrasoft pseudopotentials to the projector augmented-wave method.* Physical Review B, 1999. **59**(3): p. 1758-1775.

138. Perdew, J.P., K. Burke, and M. Ernzerhof, *Generalized Gradient Approximation Made Simple.* Physical Review Letters, 1996. **77**(18): p. 3865-3868.

139. Grimme, S., S. Ehrlich, and L. Goerigk, *Effect of the damping function in dispersion corrected density functional theory.* Journal of Computational Chemistry, 2011. **32**(7): p. 1456-1465.

140. Banszerus, L., et al., *Ultrahigh-mobility graphene devices from chemical vapor deposition on reusable copper.* Science Advances, 2015. **1**(6): p. e1500222.

141. Soluyanov, A.A. and D. Vanderbilt, *Computing topological invariants without inversion symmetry.* Physical Review B, 2011. **83**(23): p. 235401.

142. Yu, R., et al., *Equivalent expression of Z2 topological invariant for band insulators using the non-Abelian Berry connection.* Physical Review B, 2011. **84**(7): p. 075119.

143. Gresch, D., et al., *Z2Pack: Numerical implementation of hybrid Wannier centers for identifying topological materials.* Physical Review B, 2017. **95**(7): p. 075146.

144. Wu, Q., et al., *WannierTools : An open-source software package for novel topological materials.* Computer Physics Communications, 2017.

145. Zhang, L.Z., et al., *Quantum Spin Hall Effect and Tunable Spin Transport in As-Graphane.* Nano Letters, 2017. **17**(7): p. 4359-4364.

146. Li, Q., et al., *Localized Wannier function based tight-binding models for two-dimensional allotropes of bismuth.* New Journal of Physics, 2021.

147. Märkl, T., et al., *Engineering multiple topological phases in nanoscale Van der Waals heterostructures: realisation of α-antimonene.* 2D Materials, 2017. **5**(1): p. 011002.

148. Li, S.-s., et al., *Tunability of the Quantum Spin Hall Effect in Bi(110) Films: Effects of Electric Field and Strain Engineering.* ACS Applied Materials & Interfaces, 2017. **9**(25): p. 21515-21523.

149. Roushan, P., et al., *Topological surface states protected from backscattering by chiral spin texture.* Nature, 2009. **460**: p. 1106.

150. Song, Z., et al., *Quantum spin Hall insulators and quantum valley Hall insulators of BiX/SbX (X=H, F, Cl and Br) monolayers with a record bulk band gap.* NPG Asia Materials, 2014. **6**(12): p. e147-e147.

151. Hsu, C.-H., et al., *The nontrivial electronic structure of Bi/Sb honeycombs on SiC(0001).* New Journal of Physics, 2015. **17**(2): p. 025005.

152. Kobayashi, K., *Electronic states of SnTe and PbTe (001) monolayers with supports.* Surface Science, 2015. **639**: p. 54-65.

153. Solovyev, I.V., Z.V. Pchelkina, and V.I. Anisimov, *Construction of Wannier functions from localized atomiclike orbitals.* Physical Review B, 2007. **75**(4): p. 045110.

154. Zurek, E., J. Autschbach, and O.K. Andersen, *Downfolding and N‐ization of Basis Sets of Slater Type Orbitals.* AIP Conference Proceedings, 2007. **963**(2): p. 1421-1424.

155. Wu, Q., et al., *WannierTools: An open-source software package for novel topological materials.* Computer Physics Communications, 2018. **224**: p. 405-416.

156. Klein, D.J., *Graphitic polymer strips with edge states.* Chemical Physics Letters, 1994. **217**(3): p. 261-265.

157. Jaskólski, W., et al., *Edge states and flat bands in graphene nanoribbons with arbitrary geometries.* Physical Review B, 2011. **83**(23): p. 235424.

158. Zhang, S., et al., *Ideal inert substrates for planar antimonene: h-BN and hydrogenated SiC (0001).* Physical Chemistry Chemical Physics, 2018. **20**(36): p. 23397-23402.

159. Araújo, A.L., et al., *Topological nonsymmorphic ribbons out of symmorphic bulk.* Physical Review B, 2016. **93**(16): p. 161101.

160. Ando, Y. and L. Fu, *Topological Crystalline Insulators and Topological Superconductors: From Concepts to Materials.* Annual Review of Condensed Matter Physics, 2015. **6**(1): p. 361-381.

161. Li, Q., et al., *Localized Wannier function based tight-binding models for two-dimensional allotropes of bismuth.* arXiv preprint arXiv:2102.11486, 2021.

162. Bychkov, Y.A. and E.I. Rashba, *Oscillatory effects and the magnetic susceptibility of carriers in inversion layers.* Journal of Physics C: Solid State Physics, 1984. **17**(33): p. 6039-6045.

163. Min, H., et al., *Intrinsic and Rashba spin-orbit interactions in graphene sheets.* Physical Review B, 2006. **74**(16): p. 165310.

164. Xu, J.H., et al., *Tight-binding theory of the electronic structures for rhombohedral semimetals.* Physical Review B, 1993. **48**(23): p. 17271-17279.

165. Araújo, A.L., et al., *Interplay between boundary conditions and Wilson's mass in Dirac-like Hamiltonians.* Physical Review B, 2019. **100**(20): p. 205111.

166. Choi, W., et al., *Recent development of two-dimensional transition metal dichalcogenides and their applications.* Materials Today, 2017. **20**(3): p. 116-130.

167. Si, M., et al., *A ferroelectric semiconductor field-effect transistor.* Nature Electronics, 2019. **2**(12): p. 580-586.

168. Ye, J., et al., *Crystal Structures and Phase Transformation in In2Se3Compound Semiconductor.* Japanese Journal of Applied Physics, 1998. **37**(Part 1, No. 8): p. 4264-4271.

169. Ho, C.-H., Y.-C. Chen, and C.-C. Pan, *Structural phase transition and erasable optically memorized effect in layered γ-In2Se3 crystals.* Journal of Applied Physics, 2014. **115**(3): p. 033501.

170. Debbichi, L., O. Eriksson, and S. Lebègue, *Two-Dimensional Indium Selenides Compounds: An Ab Initio Study.* The Journal of Physical Chemistry Letters, 2015. **6**(15): p. 3098-3103.

171. Osamura, K., Y. Murakami, and Y. Tomiie, *Crystal Structures of α-and β-indium selenide, In2Se3.* Journal of the Physical Society of Japan, 1966. **21**(9): p. 1848-1848.

172. van Landuyt, J., G. van Tendeloo, and S. Amelinckx, *Phase transitions in In2Se3 as studied by electron microscopy and electron diffraction.* physica status solidi (a), 1975. **30**(1): p. 299-314.

173. Zheng, C., et al., *Room temperature in-plane ferroelectricity in van der Waals In₂Se₃.* Science Advances, 2018. **4**(7): p. eaar7720.

174. Ding, W., et al., *Prediction of intrinsic two-dimensional ferroelectrics in In2Se3 and other III2-VI3 van der Waals materials.* Nature Communications, 2017. **8**(1): p. 14956.

175. Manolikas, C., *New results on the phase transformations of In2Se3.* Journal of Solid State Chemistry, 1988. **74**(2): p. 319-328.

176. Collins, J.L., et al., *Electronic Band Structure of In-Plane Ferroelectric van der Waals β′-In2Se3.* ACS Applied Electronic Materials, 2020. **2**(1): p. 213-219.

177. Krukau, A.V., et al., *Influence of the exchange screening parameter on the performance of screened hybrid functionals.* The Journal of Chemical Physics, 2006. **125**(22): p. 224106.

178. Li, W., et al., *Large disparity between optical and fundamental band gaps in layered In2Se3.* Physical Review B, 2018. **98**(16): p. 165134.

179. Perdew, J.P., et al., *Understanding band gaps of solids in generalized Kohn–Sham theory.* Proceedings of the National Academy of Sciences, 2017. **114**(11): p. 2801-2806.

180. Julien, C., et al., *Electrical and optical properties of In2Se3 thin films.* Thin Solid Films, 1986. **137**(1): p. 27-37.